

NORTHWESTERN UNIVERSITY

Remote-Controlled Exchange Rates by Photoswitchable Internal Catalysis
of Boronic Ester–Diol Exchange

A DISSERTATION
SUBMITTED TO THE GRADUATE SCHOOL
IN PARTIAL FULFILLMENT OF THE REQUIREMENTS

for the degree

DOCTOR OF PHILOSOPHY

Field of Chemistry

By
David Nabil Barsoum

EVANSTON, ILLINOIS

December 2021

© Copyright by David Barsoum 2021

All Rights Reserved

Abstract

Dynamic covalent chemistry (DCC) combines the strength and directionality of covalent bonds with the reversibility of supramolecular interactions. The formation and stability of these bonds are typically regulated by parameters such as temperature, pH, concentration, catalyst loading and light. Light is an exceptionally powerful stimulus because it can be applied non-invasively with superior spatial and temporal control. Molecules that can be reversibly switched between two states using different wavelengths of light offer a unique opportunity to remotely control DCC.

Previously, photoswitches have been employed to govern the reactivity of dynamic covalent bonds via two principal strategies: (i) by rendering the dynamic bond active or inactive through light-driven valence bond tautomerization; and (ii) by tuning the reactivity of the dynamic bond with an adjacent photoswitch. Here, we present a strategy to remotely control the kinetics of dynamic covalent reactions without affecting their thermodynamics, by designing a photoswitch that modulates the reactivity of an internal catalyst. We have termed this approach photoswitchable internal catalysis (PIC).

Here we report a PIC that is capable of tuning the exchange rate between boronic ester and free diol over at least 4 orders of magnitude. The design of our photoswitch consists of two key components: first, the internal catalytic nitrogen in 8-quinoline boronic ester (8-QBE, Figure 1A), which assists in the rapid exchange between boronic ester and free diol; second, an acyl-hydrazone photoswitch that bears an acidic N–H, which forms an intramolecular H-bond when positioned ortho to a basic heterocycle (Figure 1B). Unification of these two moieties yields the PIC system in Figure 1C. In its thermodynamically favored isomer, (*E*)-PIC, the photoswitch is in the “ON”

state, in which internal catalysis from the proximal quinoline mediates rapid boronic ester exchange. Photoisomerization of the acyl-hydrazone to the “OFF” state, (**Z**)-PIC, results in the formation of an intramolecular H-bond between the quinoline nitrogen lone pair and the acyl-hydrazone N–H, deactivating internal catalysis, resulting in a drastically slower exchange (Figure 1C).

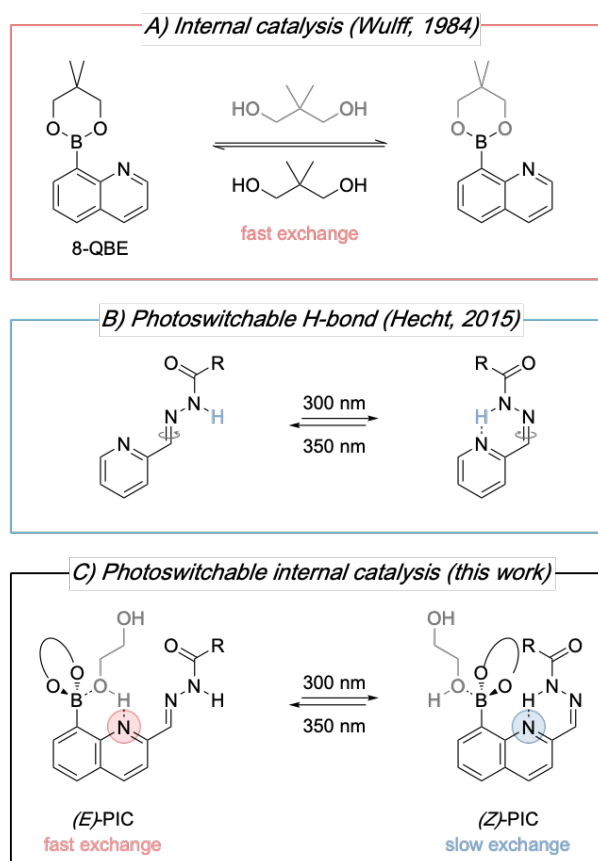


Figure 1. Conceptual design of photoswitchable internal catalysis, based on combining (A) the significant rate acceleration for boronic ester exchange provided by internal base catalysis and (B) bistable acylhydrazone photoswitches, yielding (C) photoswitch-gated internal catalysis of the boronic ester exchange.

Acknowledgements

As I near the end of this long journey I have learned so much and yet feel like I know even less. One thing I know for sure is that I could not have done this alone. The people who have supported me through this journey are the ones who deserve the credit.

First and foremost, I would like to thank my adviser, Professor Julia Kalow for the tremendous amount of support she has provided me over the last few years while working in her lab. Without her support, understanding, and patience none of this would have been possible.

I would like to thank my wife, Niky, for her love and support through this journey. There were many ups and downs, but she brought balance to my life, even during the most chaotic of times. My love for her is what kept me motivated to finish. Her love for me is what kept me strong enough to finish.

I would like to thank my lab mates for creating a positive and welcoming environment, free of judgement. In particular, I would like to thank Joseph Accardo for his support and friendship. Not only is he an amazing chemist but a good friend that helped me get through graduate school.

Finally, I would like to thank my mom and dad for their love, support and encouragement. I know that all they wish is for me to succeed.

List of abbreviations

^1H NMR	Proton nuclear magnetic resonance
8-QBA	8-quinoline boronic acid
8-QBE	8-quinoline boronic ester
^{11}B NMR	Boron nuclear magnetic resonance
^{13}C NMR	Carbon nuclear magnetic resonance
ACN	acetonitrile
AcOH	acetic acid
a.u.	arbitrary units
B_2pin_2	bis(pinacolato)diboron
BDE	bond dissociation energy
$^\circ\text{C}$	celsius
CDCl_3	chloroform
COF	covalent organic framework
DAE	diarylethylene
DCC	dynamic covalent chemistry
DCM	dichloromethane
Δ	heat
DI	deionized
DMA	<i>N,N</i> -dimethylacetamide
DMF	<i>N,N</i> -dimethylformamide
DMSO	dimethyl sulfoxide

EtOH	ethanol
EXSY	exchange spectroscopy
g	gram
H ₂ O	water
H-bond	Hydrogen bond
HCl	hydrochloric acid
HOMO	highest occupied molecular orbital
<i>hν</i>	light
KOAc	potassium acetate
LCMS	liquid chromatography mass spectrometry
LUMO	lowest unoccupied molecular orbital
LRMS	low resolution mass spectrometry
M	molar
Me	methyl
MeOH	methanol
mg	milligram
MHz	mega hertz
μ	micro
MIDA	N-methyliminodiacetic acid
mL	milliliter
mM	millimolar
mmol	millimole

mol	mole
Na ₂ CO ₃	Sodium carbonate
Na ₂ SO ₄	Sodium sulfate
NaOH	Sodium Hydroxide
n-BuPAd ₂	Di(1-adamantyl)-n-butylphosphine
nm	nanometer
NMR	nuclear magnetic resonance
NGP	neighboring group participation
Pd ₂ (dba) ₃	tris(dibenzylideneacetone)dipalladium(0)
PIC	photoswitchable internal catalysis
ppm	parts per million
PSS	photostationary state
<i>p</i> -TSA	para toluene sulfonic acid
rt	room temperature
SeO ₂	Selenium (IV) Dioxide
TFA	trifluoroacetic acid
THF	tetrahydrofuran
UV	ultraviolet
UV-Vis	Ultraviolet-visible
VT-NMR	variable temperature nuclear magnetic resonance
ZnCl ₂	Zinc (II) Chloride

	9
Table of Contents	
<i>Abstract</i>	3
<i>Acknowledgements</i>	5
<i>List of abbreviations</i>	6
<i>Table of Contents</i>	9
<i>List of Figures</i>	12
<i>List of Schemes</i>	15
Chapter 1 – Dynamic Covalent Chemistry	16
1.1 Dynamic Covalent Chemistry	16
1.1.1 Internal Catalysis	18
1.1.2 Boronic Ester/diol exchange	19
Chapter 2 – Photoswitchable Dynamic Covalent Bonds	23
2.1 Introduction to Photoresponsive Systems	23
2.2 Photoswitchable catalysis	23
2.3 Introduction to Photoswitches	24
2.3.1 Electrocyclization Photoswitches	26
2.3.2 E/Z isomerization Photoswitches	27
2.4 Photoinduced Modulation of Reactivity	28
2.5 Design of a PIC to remotely tune boronic ester-diol exchange	30
Chapter 3 – Synthesis of (E)-PIC	31

	10
3.1 Quinoline synthesis	32
3.2 Quinaldine Oxidation	33
3.3 Acetal protection	34
3.4 Borylation	34
3.5 Acetal Deprotection	36
3.6 Hydrazone Condensation	37
3.7 Esterification	38
3.9 Alternative Synthetic Routes	39
3.10 Synthetic Procedures	41
3.11 NMR data	48
<i>Chapter 4 – Photoswitch Properties</i>	57
4.1 Photostationary State	57
4.2 Fatigue Resistance	59
4.3 Quantitative Conversion of (<i>E</i>)-PIC_{ester} and (<i>Z</i>)-PIC_{ester}	60
<i>Chapter 5 – Remote-controlled exchange rates using photoswitchable internal catalysis</i>	62
5.1 Photoswitchable Exchange Rates	62
5.2 VT-NMR Kinetic Experiment Procedures	67
<i>References</i>	74
<i>Appendix A. Original Research Proposal</i>	80

<i>Appendix B. Curriculum Vitae</i>	11
	91

List of Figures

Figure 1. Conceptual design of photoswitchable internal catalysis, based on combining (A) the significant rate acceleration for boronic ester exchange provided by internal base catalysis and (B) bistable acylhydrazone photoswitches, yielding (C) photoswitch-gated internal catalysis of the boronic ester exchange.	4
Figure 2. Common dynamic covalent reactions.	16
Figure 3. Schematic overview of the different strategies that have been applied to enhance or control the exchange rates of dynamic covalent reactions.	17
Figure 4. Mechanism of degenerate exchange of boronate ester and free diol.	20
Figure 5. (A) Tuning neighboring group to control the exchange kinetics of boronic ester. (B) Design of diboronic ester cross- linkers with tunable exchange kinetics. (C) Dynamic exchange of boronic ester cross-linkers affords dynamic materials.	21
Figure 6. Conceptual approaches to photoresponsive systems.	24
Figure 7. Common photoswitch scaffolds.	26
Figure 8. Acyl hydrazone photoswitches functionalized at the carbonyl position with either a phenyl group, which displays T-type photochromism, or with a H-bond acceptor at the ortho position, which displays P-type photochromism.	28
Figure 9. Conceptual design of a photoswitch that modulates the reactivity of a reaction.	29
Figure 10. Azobenzene photoswitch that reversibly masks/unmasks an activating hydroxyl group ortho to an aldehyde.	30
Figure 11. ¹ H NMR of the aromatic region of (E)- and (Z)-PICacid shows the N–H peak shift downfield after isomerization from E to Z.	57

- Figure 12.** (A) Conversion of (E)-PICacid (red line) in MeCN (1.56×10^{-5} M) to (Z)-PICacid,PSS (black line) followed in time under constant irradiation ($\lambda_{\text{irr}} = 300$ nm, $t_{\text{irr}} = 90$ sec); IP at 336 nm. (B) Absorbance followed at $\lambda_{\text{max}}(\text{E}) = 322$ nm over time as in (A)58
- Figure 13.** A) UV-Vis absorbance of (E)-PICacid (black line) and the photostationary state of (Z)-PICacid photostationary state (red line) in acetonitrile at 1.56×10^{-5} M). B) Corresponding absorbance of PICacid after irradiation at 300 nm and 350 nm.59
- Figure 14.** ^1H NMR spectra of (E)-PICester (bottom) and quantitative conversion to (Z)-PICester (top) after irradiation with 300 nm light.60
- Figure 15.** (A) UV-Vis absorption of (E)-PICacid in MeCN (black line, 1.56×10^{-5} M) and (Z)-PICacid,PSS (red line). (B) UV-Vis absorption of (E)-PICester (black dashed line) and (Z)-PICester (red dashed line).61
- Figure 16.** ^1H NMR of the dynamic exchange in (E)-PICester + neo-pentylglycol (25 °C) and static exchange in (Z)-PICester + neo-pentylglycol (65 °C).63
- Figure 17.** ^1H VT-NMR of the dynamic exchange of (E)-PICester (left) and static exchange in (Z)-PICester (right).64
- Figure 18.** ^1H VT-NMR of the dynamic exchange of Me-QBE (left) and Me-QBE + TFA (right)66
- Figure 19.** VT-NMR kinetic study boronic ester transesterification of (E)-PICester and neo-pentyl glycol. Coalescence for (E)-PICester at -15 °C ($\Delta\nu = 72.0$ Hz) provides $k \sim 4100$ s $^{-1}$ at 25 °C.70
- Figure 20.** VT-NMR kinetic study boronic ester transesterification of (Z)-PICester and neo-pentyl glycol. Coalescence for (Z)-PICester is not observed up to 75 °C. Coalescence at 25 °C represents the chair flip (activation energy = 13.7 kcal/mol).71

	14
Figure 21. (E)-PICcrosslinker in a polymer network.	72
Figure 21. (E)-PICcrosslinker in a polymer network.	73
Figure 22.. Mechanism of spontaneous blinking rhodamine dyes.	83
Figure 23. Mechanism of Zinc binding induced bathochromic shift in BIPY fluorophores.	84
Figure 24. Proposed mechanism for super-resolution imaging of Zinc ions by the combination of a FRET pair consisting of a spontaneous blinking (acceptor) and a Zinc sensor (donor).	85
Figure 25. Synthesis of BIPY-SPC.	86
Figure 26. Utilizing CuAAC to screen donor fluorophores to be compatible with SPC.	87

List of Schemes

Scheme 1. Retro synthesis of (E)-PIC	31
Scheme 2. Synthesis of (E)-PIC	32
Scheme 3. Oxidation of Me-QBA with SeO ₂	33
Scheme 4. Synthesis and reactivity of 3-OMe.....	34
Scheme 5. Direct borylation of 2 and (E)-PICBr.....	35
Scheme 6. The unusual stability of heteroaromatic acetals	36
Scheme 7. The complex acid/base equilibrium of 8-QBA	37
Scheme 8. Solubility equilibrium of 5	37
Scheme 9. Some diols used to make boronic esters from (E)-PICacid and Me-QBA	38
Scheme 10. Dimethyl acetal route	39
Scheme 11. BF ₃ K protection route.....	40
Scheme 12. MIDA protection route.....	40
Scheme 13. Synthesis of Me-QBA and Me-QBE.....	46
Scheme 14. Crystal structure of Me-QBA-OMe and catechol in methanol.....	67

Chapter 1 – Dynamic Covalent Chemistry

1.1 Dynamic Covalent Chemistry

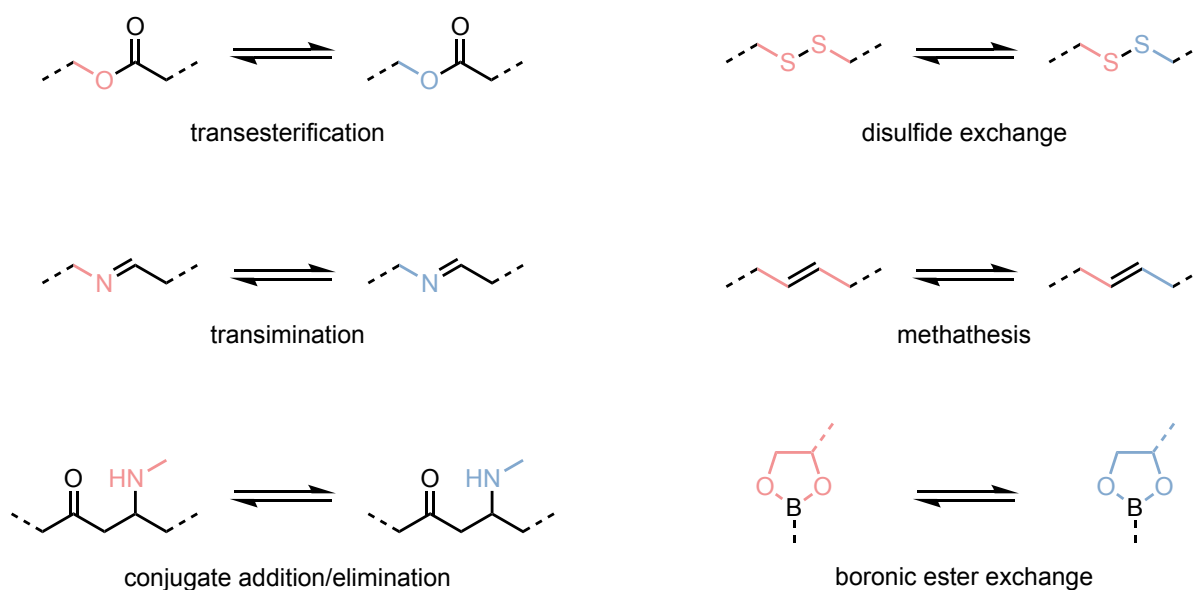
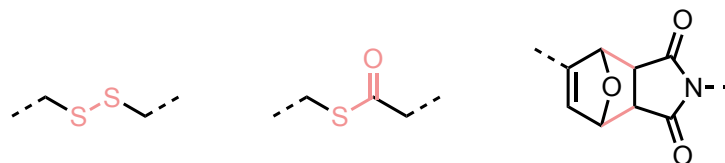


Figure 2. Common dynamic covalent reactions.

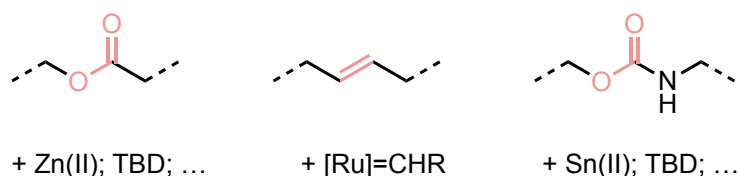
Dynamic covalent chemistry (DCC) combines the strength and directionality of covalent bonds with the reversibility of supramolecular interactions. Owing to their tunability and robustness, dynamic covalent bonds have found wide application in library synthesis, bioconjugation, self-assembled receptors, covalent organic frameworks (COFs), self-healing and adaptive polymers, and responsive sensors.¹⁻⁷ Some of the most popular dynamic covalent reactions include transesterification, transimination, conjugate addition–elimination, disulfide exchange, methathesis, and boronic ester exchange (Figure 2). The formation and stability of these

bonds are typically regulated by parameters such as temperature, pH, concentration, catalyst loading and light.

A) Intrinsically reactive bonds



B) More robust bonds activated by external catalysis



C) More robust bonds activated by internal catalysis



Figure 3. Schematic overview of the different strategies that have been applied to enhance or control the exchange rates of dynamic covalent reactions. (A) Intrinsically reactive dynamic systems that apply reversible, weak or transient covalent bonds such as disulfides, thioesters and furan– maleimide adducts. (B) More robust bonds that are activated by external catalysis with common examples such as acid or base-promoted transesterification, transcarbamoylation or ruthenium catalyzed cross-metathesis. (C) And another strategy to activate more robust covalent bonds making use of an internal catalytic effect, without requiring the use of highly reactive groups.

The reversibility of DCC is key to properties such as error correction in COFs and self-healing in polymer networks, but in order for an exchange reaction to be compatible with the

application of interest, the chemistry must also be kinetically accessible. There are several strategies that are used to enhance or control the exchange rates of dynamic covalent reactions.⁸ The first is by exploiting intrinsically reactive bonds such as disulfides,⁹ thioesters¹⁰ and furan–maleimide adducts (Figure 3A).¹¹ This strategy is conceptually most similar to supramolecular chemistry and, in the context of bulk materials, can compromise long-term stability. The second common strategy is activation of dynamic bonds by an external catalyst. The introduction of a strong Lewis acid or base, or transition-metal complex, can activate robust or moderately reactive covalent bonds. Some common reactions that utilize this strategy are Lewis acid/base-catalyzed transesterification,¹² transcarbamoylation,¹³ or ruthenium-catalyzed cross-metathesis (Figure 3B).¹⁴ Finally, dynamic covalent bonds can be activated through an “internal catalyst”. This strategy requires a more subtle design wherein the catalytic functionality is positioned such that it can selectively activate nearby dynamic covalent bonds (Figure 3C).

1.1.1 Internal Catalysis

Internal catalysis relies on proximity-induced enhancement of reactions of nearby functional groups. These proximal groups facilitate reactivity by stabilizing transition states and creating lower-energy reaction pathways through inductive, ionic, electrostatic, dipolar or covalent interactions, which would not be kinetically significant in an intermolecular context.¹⁵ Because of the decrease in entropy, relatively unreactive functional groups such as mild acids or bases can have pronounced influences on reactivity. A notable effect arises when a substituent can stabilize the transition state or reaction intermediate by having a covalent (or covalent-like) bond to the reaction center.¹⁶ This behavior, also known as neighboring group participation (NGP), usually

involves significant rate effects on reactions compared to their equivalents without those proximal substituents.

1.1.2 Boronic Ester/diol exchange

Boronic ester transesterification represents an ideal chemistry to demonstrate switchable internal catalysis due to its wide dynamic range and high bond dissociation energy (B-O BDE = 125 kcal/mol). In 1984, Wulff reported that the rate of exchange of boronic ester with diols spans a remarkable 14 orders of magnitude depending on the boronic ester structure (Figure 4C).¹⁷ The exchange reaction proceeds via three fundamental steps: (I) addition, (II) proton transfer, and (III) elimination (Figure 4A). A small change in structure can alter the identity of the rate-limiting step, resulting in a dramatic change in rates (Figure 4B, C). At 20 °C, phenylboronic acid 1,2-propanediol ester displays a modest exchange rate of 10^{-2} s^{-1} , and proton transfer was determined to be rate limiting (II > III > I) based on a large kinetic isotope effect ($k_{\text{H}}/k_{\text{D}} = 4\text{-}5$). An increase in steric hindrance slows the exchange by as much as 4 orders of magnitude by increasing the barrier for addition (I > II > III). In contrast, installing a proximal basic group significantly decreases the barrier for proton transfer through internal catalysis, making elimination rate limiting (III > II > I, no KIE) and increasing the exchange rate by up to 10^9 -fold relative to phenylboronic ester exchange.

The dramatic rate enhancement observed in **8-QBE** can be attributed to the proximity of the quinoline nitrogen lone pair in relation to the boronic ester^{46,47} and the rigid aromatic structure.⁴⁸ This structure allows the quinoline lone pair to form a 6-membered ring in the proton transfer transition state. The commonly used 2-aminomethyl “Wulff-type” phenylboronic ester

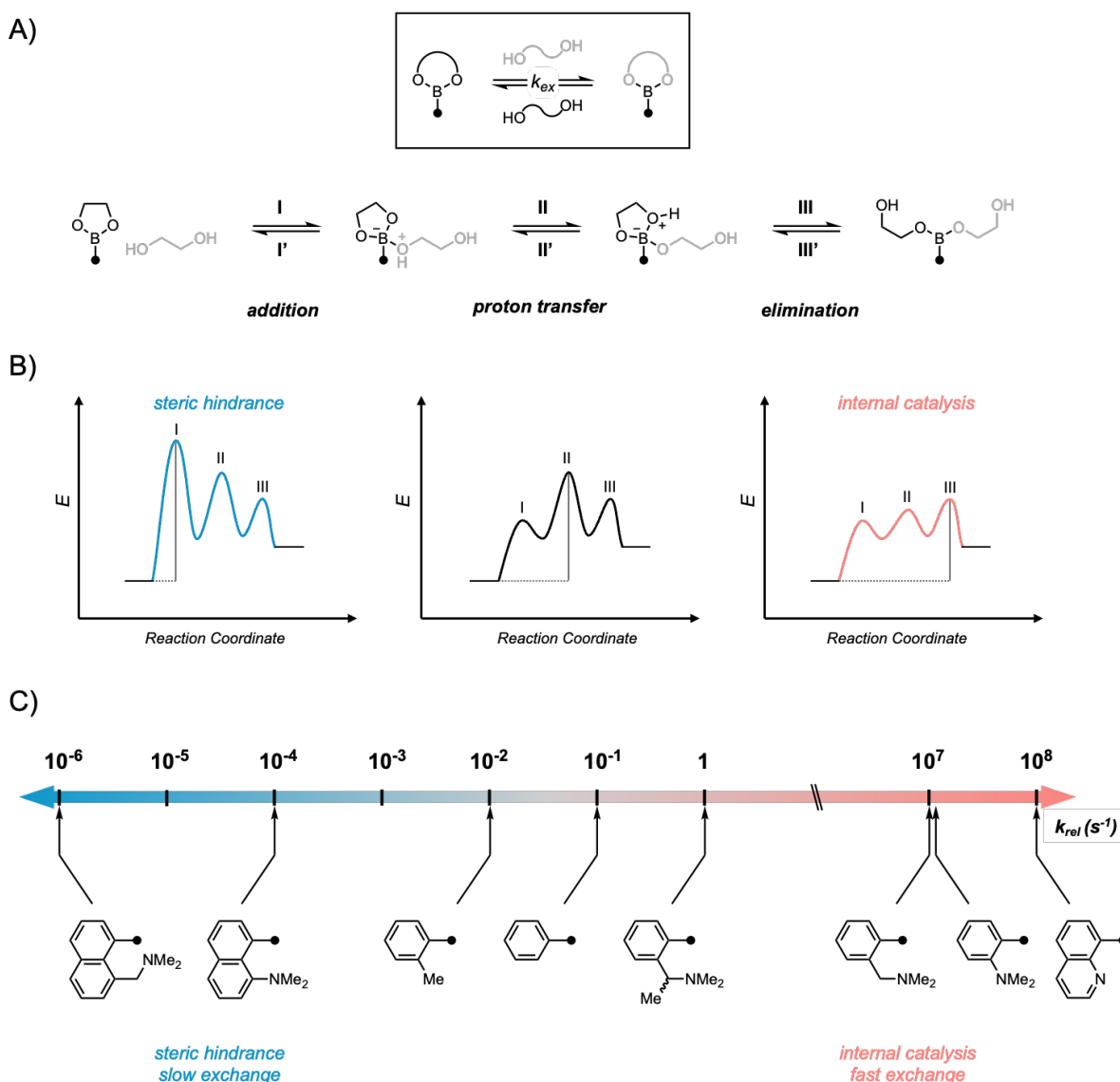


Figure 4. (A) Mechanism of degenerate exchange of boronate ester and free diol. The forward reaction (I \rightarrow II \rightarrow III) is followed by the reverse (III' \rightarrow II' \rightarrow I') to generate the final product, which is identical to the starting reactants in a degenerate exchange process. (B) Reaction coordinate diagram showing the change in activation energies corresponding to structural changes, i.e., introduction of a proximal bulky group (left) or proximal basic group (right) in comparison to phenyl boronic ester (middle). For simplicity, the reaction coordinate diagram shows only half of the reaction up to the bis-diol trigonal intermediate, since the reverse reactions to form the boronic ester product are identical, based on microscopic reversibility. (C) Dynamic range of exchange kinetics for boronic esters.

undergoes exchange an order of magnitude slower than **8-QBE**, despite the more basic nitrogen, highlighting the importance of entropy in neighboring group participation.

In 2015, Guan reported the relationship between small molecule exchange rates of boronic ester transesterification and self-healing properties in polymer networks.¹⁸ In this work, the authors compared a boronic ester bearing an internal catalyst that displays fast exchange rates with free diols ($k_{\text{ex}} \approx 3000 \text{ s}^{-1}$) to a boronic ester without an internal catalyst ($k_{\text{ex}} = 0.016 \pm 0.004 \text{ s}^{-1}$) showing about 5 orders of magnitude difference in exchange rates (Figure 5). In this work they used a divalent cross-linker with adjustable exchange kinetics to tune the properties of bulk polymer networks. Interestingly, when implemented into a polymer network as a crosslinker, the boronic ester with the internal catalyst present shows remarkable self-healing properties. On the other hand, the crosslinker without an internal catalyst was not only less malleable but did not display self-healing properties. Guan further expanded the concept of internally catalyzed cross linkers in polymer networks with silyl ethers, again showing that crosslinkers substituted with internal

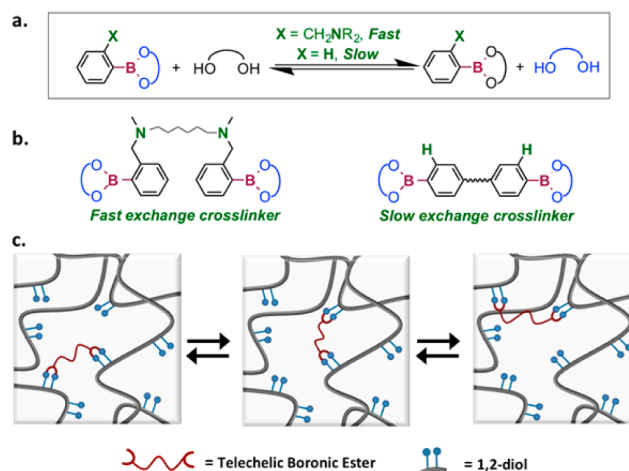


Figure 5. (A) Tuning neighboring group to control the exchange kinetics of boronic ester. (B) Design of diboronic ester cross-linkers with tunable exchange kinetics. (C) Dynamic exchange of boronic ester cross-linkers affords dynamic materials. Figure adapted from reference 18.

catalysts display fast exchange kinetics that can be translated to malleability and reprocessability in bulk materials, whereas their uncatalyzed counterparts do not.¹⁹

2.1 Introduction to Photoresponsive Systems

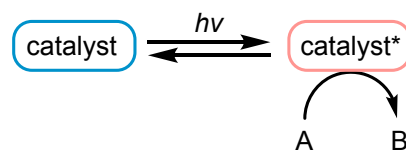
Light is an attractive stimulus to control dynamic covalent reactions because it can be applied non-invasively with excellent spatial and temporal control. Dynamic covalent bonds that respond to light require a photoactive component. Photoswitches, which can be reversibly switched between two states using different wavelengths of light, offer a unique opportunity to remotely control DCC.

2.2 Photoswitchable catalysis

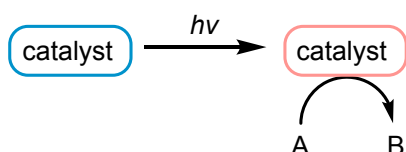
Several conceptually distinct approaches have been used in photoresponsive reactions, including photocatalysis, photoactivated catalysis, and photoswitchable catalysis (figure 3).²⁰ In photocatalysis, an inactive pre-catalyst is irradiated to generate a catalytically active photoexcited state which then reacts with a substrate (Figure 6A). On the other hand, photoactivated catalysis starts with an inactive catalyst and upon irradiation adopts a new ground-state structure that is catalytically active (Figure 6B). Photoswitchable catalysis involves a catalytically active species that undergoes a reversible photochemical transformation resulting in a change of the intrinsic catalytic properties (Figure 6C). The photoinduced transformation may turn on/off catalysis or may change the rate at which the catalyst facilitates a given reaction.

An ideal photoswitchable catalyst requires that the photoinduced transformation (1) occurs with high efficiency in both the forward and the reverse directions, (2) causes a significant change in steric or electronic properties of the catalyst, and (3) ultimately results in a change in the catalytic activity.²⁰

A) Photocatalysis



B) Photoactivated catalysis



C) Photoswitchable catalysis

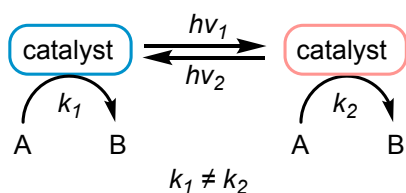


Figure 6. Conceptual approaches to photoresponsive systems.

2.3 Introduction to Photoswitches

Photochromism describes the reversible transformation of a molecular species between two isomers induced by light. The thermodynamically more stable isomer A is transformed into metastable isomer B. The back reaction can occur either photochemically (P-type photochromism) or thermally (T-type photochromism). Furthermore, there is a distinction between positive and negative photochromism, depending on if the absorption of B is red shifted as compared to A (positive) and vice versa (negative).²¹

There are several parameters that must be considered when designing the optimal photoswitch for its designated use: addressability, efficiency, thermal stability, and reliability.²¹ Addressability refers to the specific wavelengths used, which must be compatible with the material surrounding the photoswitch and intended use. Furthermore, the absorption of each isomer will determine the selectivity for separately exciting both switching states. This difference is typically reflected in the absorbance maximum of each isomer (λ_{max}) including their extinction coefficient (ϵ) as well as their band separation. Efficiency is typically evaluated by the degree of photoconversion for forward and backward reactions reflected in the composition of the photostationary state (PSS) at a specific irradiation wavelength. The latter depends on the absorbance ratios of both isomers and on the quantum yields (Φ) for their interconversion. Thermal stability is typically quantified by the thermal half-life ($t_{1/2}$) of the metastable isomer at a specific temperature. Finally, reliability refers to the ability of the photoswitch to undergo many forwards and backwards switching cycles without significant degradation due to side reactions (fatigue resistance).

Photoswitches can be categorized by the type of chemical reaction involved in the light-induced isomerization. The most common reactions are hydrogen transfer, cycloaddition, homolytic or heterolytic bond dissociation, *E/Z*-isomerization, and electrocyclization.²¹ I will briefly summarize important *E/Z* isomerization and electrocyclization-based photoswitches as they are the most frequently represented classes of photoswitches (Figure 7).

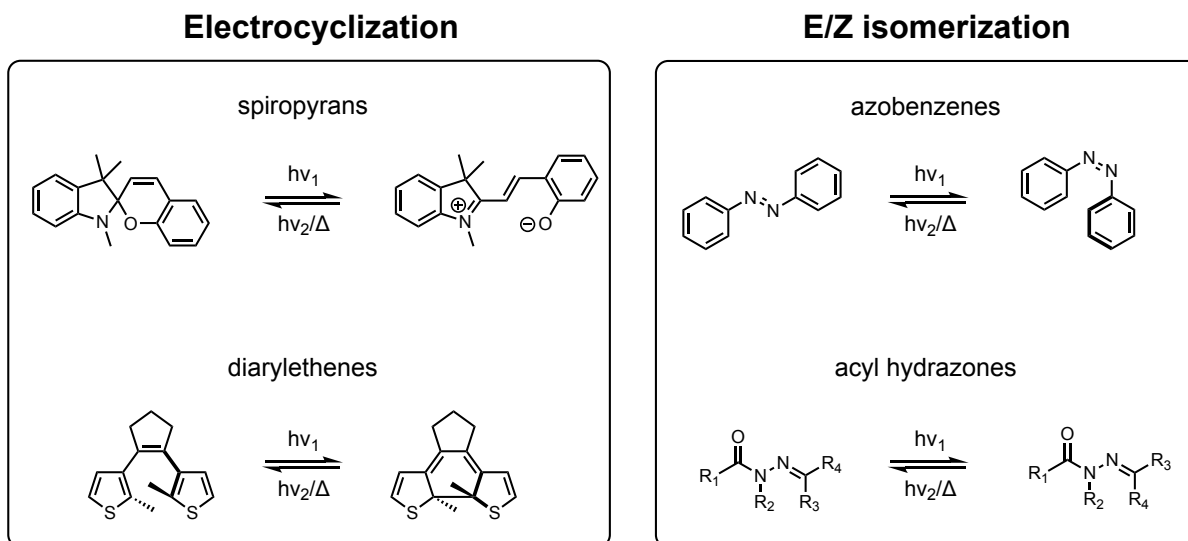


Figure 7. Common photoswitch scaffolds

2.3.1 Electrocyclization Photoswitches

Electrocyclic reactions involving the delocalization of six π -electrons over a scaffold of six atoms are common in molecular photoswitches. Among the most prominent electrocyclic photoswitches are spiropyrans and diarylethenes (DAEs).

Spiropyrans

Spiropyrans are among the oldest examples of electrocyclic photoswitches.²² An important feature of spiropyrans is that the photoisomerization induces a large change in both the structure (orthogonal vs planar geometry) as well as the dipole moment due to the zwitterionic character of the open merocyanine form. Although they have been widely employed, spiropyrans possess a number of drawbacks including low fatigue resistance, the need for UV light to induce ring opening, the fast thermal back reaction, and sensitivity to medium.

Diarylethenes

DAEs were developed in the early 1980s and are among the most popular electrocyclic photoswitches today. DAEs are unique in that the geometry of the molecule is relatively unaltered by the photoisomerization, whereas the electronic structure, reflected by the energy levels of the highest occupied molecular orbital (HOMO) and lowest unoccupied molecular orbital (LUMO), experiences dramatic changes.²³

2.3.2 *E/Z* isomerization Photoswitches

Azobenzenes

Some of the simplest molecules that undergo photoinduced isomerization of a N=N central double bond are azobenzenes. Azobenzenes are arguably the most used photoswitch class today due to their relatively simple structure, rapid and easy synthesis, as well as robust and efficient photochemistry.²⁴ On the other hand, azobenzenes generally have relatively short thermal half-lives.

Acyl hydrazones

Although much less prominent, an even more synthetically accessible class of photoswitches that undergoes *E/Z*-photoisomerization is acyl hydrazones, pioneered by the groups of Lehn²⁵ and Aprahamian.²⁶ *E*→*Z* isomerization of the C=N bond can be induced either by UV or visible light, while the reverse *Z*→*E* isomerization proceeds either photochemically or thermally. The properties of both *E* and *Z* isomers and their isomerization processes are heavily dependent on the substitution pattern and thus all key performance parameters, i.e., addressability, efficiency, thermal stability, and reliability can be systematically tuned.²⁷

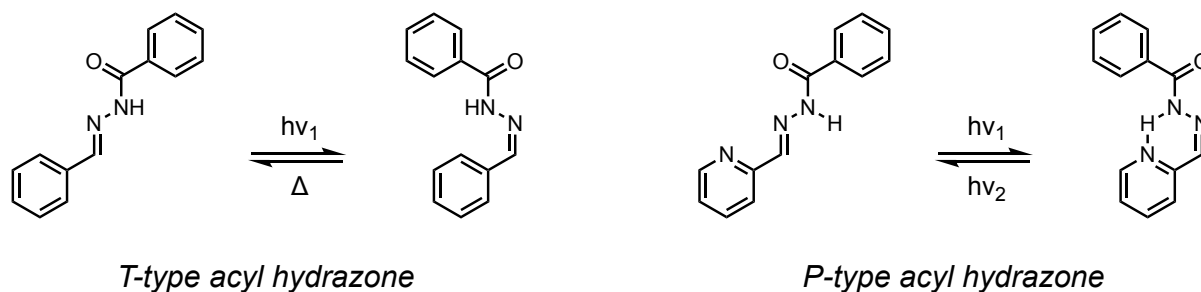


Figure 8. Acyl hydrazone photoswitches functionalized at the carbonyl position with either a phenyl group, which displays T-type photochromism, or with a H-bond acceptor at the ortho position, which displays P-type photochromism.

One of the most notable features of this class of photoswitches is the ease of their preparation by simple condensation of an acyl hydrazide and a carbonyl compound under mild conditions. The properties of these photoswitches can easily be tuned by these two components. For example, if the carbonyl component is functionalized with a phenyl group, the *Z* isomer undergoes thermal isomerization back to the *E* isomer, thus making it a T-type photoswitch (Figure 8). On the other hand, when the carbonyl is functionalized ortho to a heterocyclic H-bond acceptor, such as in the case of 2-substituted pyridine, the *Z* isomer becomes thermally stabilized. This thermally stable *Z* isomer can be readily converted back to the *E* isomer photochemically, thus making it a P-type photoswitch.

2.4 Photoinduced Modulation of Reactivity

Reactivity modulation is reflected in a change of the activation barrier, and it can be accomplished either internally, by rendering the substrate and/or product photoswitchable, or externally, by employing a photoswitchable catalyst.²⁸ The main difference in these strategies is that an internal photoswitch requires a stoichiometric number of photons, whereas an external photoswitchable catalyst allows the use of sub-stoichiometric photons and hence catalytic

amplification. Because we are interested in modulating the reactivity of dynamic covalent bonds in a stoichiometric manner, we will focus our attention on photoswitches which modulate the reactivity of bonds internally.

Previously, photoswitches have been employed to govern the reactivity of dynamic covalent bonds via two principal strategies: (i) by rendering the dynamic bond active or inactive through light-driven valence bond tautomerization;²⁹⁻³¹ and (ii) by tuning the reactivity of the dynamic bond with an adjacent photoswitch.^{32,33}

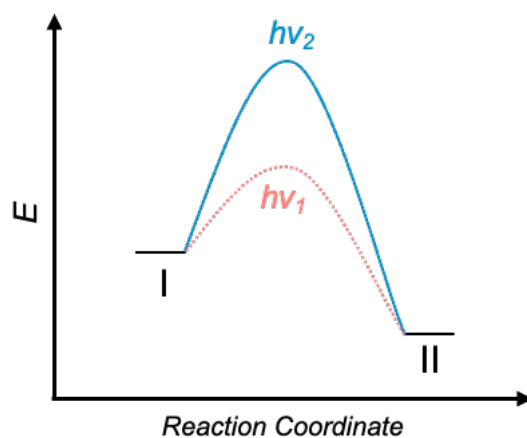


Figure 9. Conceptual design of a photoswitch that modulates the reactivity of a reaction.

In the simplest case, the photoswitching event can enhance or reduce the reactivity in a dynamic covalent reaction (Figure 9). Hecht illustrated such a system in the photomodulation of aldehyde reactivity in imine formation/exchange using an azobenzene to reversibly mask/unmask a phenol ortho to an aldehyde (Figure 10).³⁰ The associated rate increase translates to approximately 2.4-fold faster imine formation in the *Z*-isomer versus the *E*-isomer. Notably, the photoisomerization only changes the height of the thermal barrier, i.e. ΔG^\ddagger , and hence accelerates

or decelerates the reaction without altering the overall thermodynamics, i.e. ΔG° (Figure 9). This is a prime example of what we have termed photoswitchable internal catalysis (PIC).

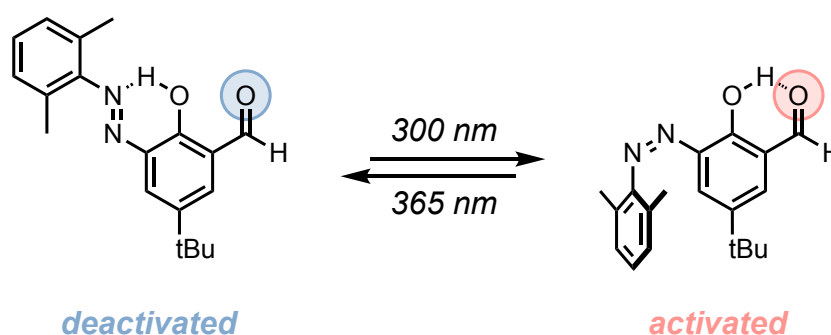
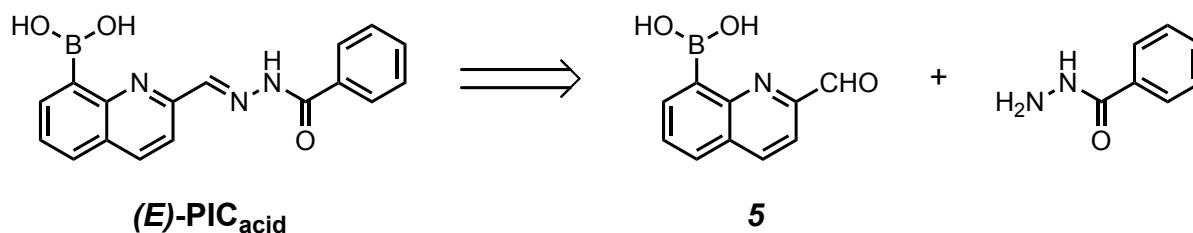


Figure 10. Azobenzene photoswitch that reversibly masks/unmasks an activating hydroxyl group ortho to an aldehyde.

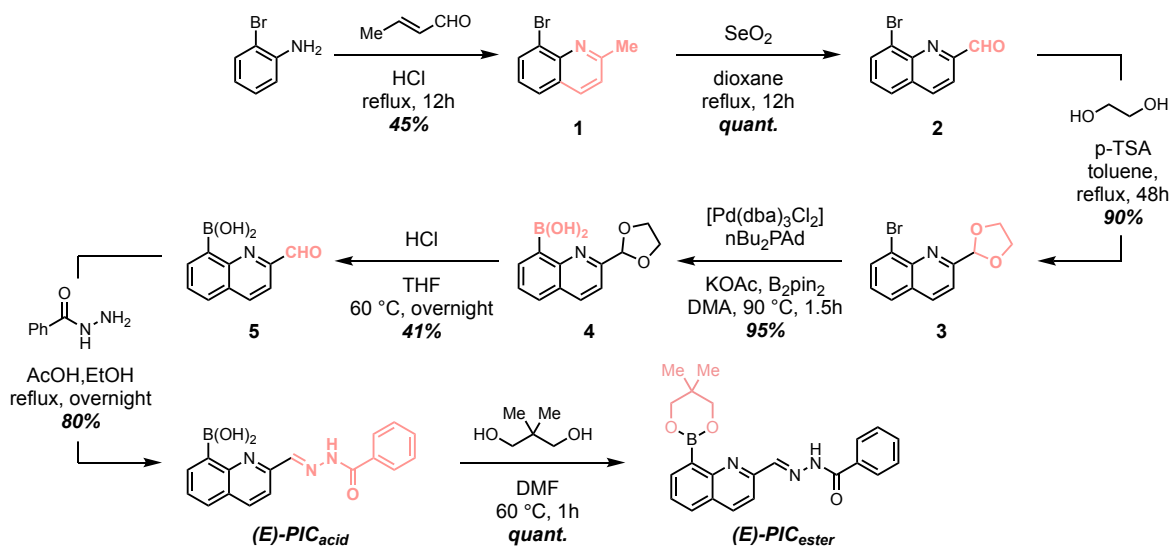
2.5 Design of a PIC to remotely tune boronic ester-diol exchange

We imagined that the rate-limiting step of boronic ester exchange could be remotely tuned with an appropriate photoswitch, thus dramatically altering the rate of exchange. Our strategy was to deactivate internal catalysis in **8-QBE** by engaging the quinoline lone pair in an intramolecular H-bond. Our attention was drawn to a relatively novel class of acyl-hydrazone photoswitches that bear an acidic amide N–H bond.^{25,26} Hydrazone photoswitches derived from 2-pyridinecarboxyaldehyde or 2-quinolinecarboxyaldehyde are thermally stable in the *Z* isomer thanks to the formation of a six-membered intramolecular H-bond. We envisioned that the intramolecular H-bond, in addition to stabilizing the *Z* isomer, could deactivate internal catalysis in **8-QBE**. This design yielded **PIC** (Figure 1C), wherein exchange is accelerated by internal catalysis when the hydrazone adopts the *E* configuration and dramatically slowed in the *Z* isomer.

Scheme 2. Retrosynthesis of (*E*)-PIC.

We imagined that our proposed photoswitch (*E*)-PIC could be derived from condensation between the respective acyl-hydrazide and (2-formylquinolin-8-yl)boronic acid (**5**) (Scheme 1). While the hydrazide is commercially available, **5** must be synthesized. Because boronic acids are sensitive functional groups that are most commonly used as intermediates in metal-mediated cross-coupling reactions, there are few synthetic examples in which a boronic acid is carried through a multi-step synthesis.³⁴ The synthesis (Scheme 2) posed several challenges that we will address in the subsequent sections. First, we will briefly discuss the synthesis of 8-substituted quinaldines and their subsequent oxidation to access 8-bromo-quinoline-2-aldehyde. A 3-step sequence (acetal protection, borylation, acetal deprotection) is used to install the boronic acid. Following acetal deprotection, the **5** undergoes condensation with an acyl-hydrazide to afford our proposed photoswitch.

Scheme 3. Synthesis of (*E*)-PIC



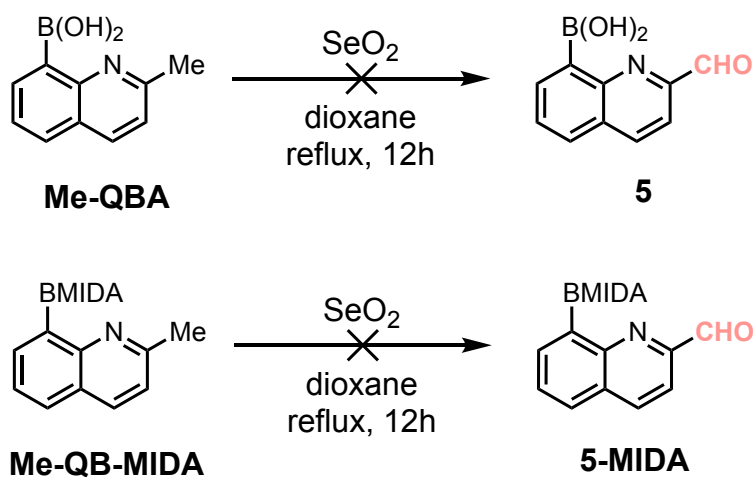
3.1 Quinoline synthesis

Quinoline synthesis can be achieved by a number of different routes. We chose the Doebner-Miller synthesis to access an 8-bromo-2-methyl quinoline (**1**) under standard conditions.³⁵ Several variations of this reaction were attempted to improve the isolated yield. The inclusion of toluene to make a biphasic reaction mixture has been shown to reduce polymerization of crotonaldehyde under highly acidic conditions,³⁶ however, when tested these conditions, the reaction was sluggish and isolation became challenging. Likewise, the introduction of zinc chloride has been shown to reduce the reactivity of the quinoline through coordination. Again, no improvements in yield were observed, and thus we opted for the standard conditions. However, the addition of 1.0 equivalent of $ZnCl_2$ during isolation significantly facilitated purification by removal of excess unreacted aniline.³⁷ The reaction was tested up from 5.0-100.0 g and we found that the optimal scale for best yields and isolation was 20.0 g.

3.2 Quinaldine Oxidation

Oxidation of **1** to access 8-bromoquinoline-2-carbaldehyde (**2**) was easily achieved using SeO_2 , often in near quantitative yields.³⁸ The reaction proceeds smoothly to completion and, after filtering off any selenium byproducts, a pure product was isolated without the need for further purification. However, if the SeO_2 is not properly activated, the reaction does not reach completion and purification by column chromatography is required.

Scheme 4. Oxidation of **Me-QBA** with SeO_2

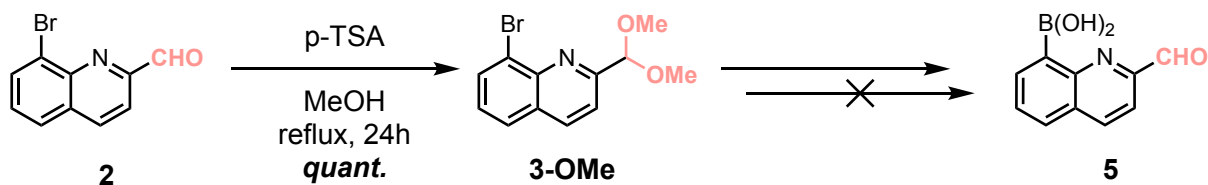


In an effort to directly access **5** without the need of a protecting group, **Me-QBA** was exposed to SeO_2 . Unfortunately, the selenium reagent oxidizes the boronic acid and no desired product is observed (Scheme 3). When a MIDA protecting group is installed in order to protect the boron from oxidation, no reaction appeared to proceed.

3.3 Acetal protection

Because of the highly reactive aldehyde in **2**, we chose a three-step sequence (protection, borylation, deprotection) to access (2-formylquinolin-8-yl)boronic acid (**5**). The acetal protection of **2** was achieved by acid catalysis with ethylene glycol under Dean-Stark conditions to yield 8-bromo-2-(1,3-dioxolan-2-yl)quinoline (**3**). A dimethyl acetal adduct can also be accessed by refluxing in methanol. Although higher yields are observed (Scheme 4), the dimethyl acetal is much more robust and becomes challenging to deprotect, which we will discuss in Section 3.5.

Scheme 5. Synthesis and reactivity of **3-OMe**

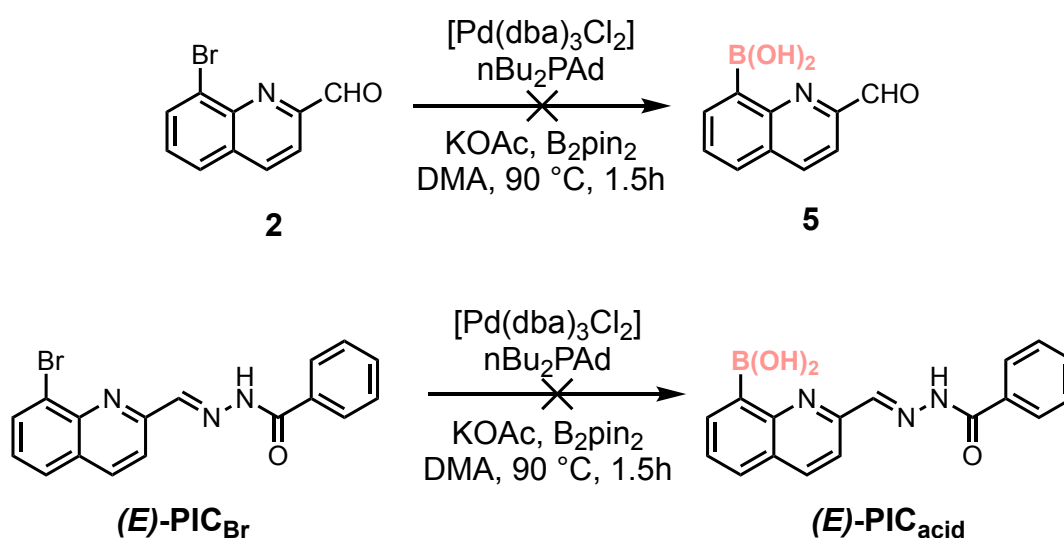


3.4 Borylation

Arylboronic acids are typically synthesized via two methods from the corresponding aryl halide: 1) transition-metal catalyzed Miyaura borylation or 2) lithium-halogen exchange and trapping. Previous reports using the latter to borylate 8-bromo quinoline show poor yields, and thus transition-metal mediated synthesis was the preferred route to access (2-(1,3-dioxolan-2-yl)quinolin-8-yl)boronic acid (**4**). Initial attempts using standard Miyaura borylation procedure ($\text{PdCl}_2(\text{dppf})$, KOAc, dioxane, $80\text{ }^\circ\text{C}$) were not fruitful. Quinolines are routinely used to chelate to various metals due to their high binding affinity. In this case, quinoline appears to poison the catalyst and the reaction stalls, resulting in the recovery of starting material. Because of the

relevance of quinolines in drug discovery, Senanayake and co-workers developed a method to selectively borylation 8-bromoquinolines using the ligand *n*Bu₂PAd.³⁹ Much to our satisfaction, this method consistently produces high yields of pure product with little need for purification.

Scheme 6. Direct borylation of **2** and (*E*)-PIC_{Br}

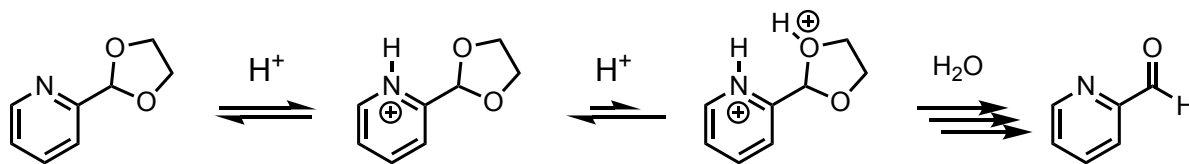


In an effort to side-step the acetal protection and access **5**, direct borylation of **2** was attempted. Although other aldehydes have been reported to be stable under normal Miyaura borylation conditions, this was not the case under Senanayake's conditions (Scheme 5). The substrate appears to dimerize and no desired product was observed. Likewise, when (*E*)-PIC_{Br} was subjected to the borylation conditions, no desired product was observed, presumably due to undesired reactivity of the hydrazone.

3.5 Acetal Deprotection

The synthesis and isolation of (2-formylquinolin-8-yl)boronic acid (**5**) from **4** posed several challenges and became the bottleneck of the synthesis. Acetal deprotection is typically achieved under mildly acidic conditions. These conditions proved problematic when presented with acid-sensitive functional groups such as quinoline and boronic acids, and the unique combination of these two groups in the **8-QBA** scaffold posed further challenges. Additionally, ortho substituted heteroaromatic acetals have been shown to be unusually resistant to acetal deprotections.⁴⁰ Under acidic conditions, the basic quinoline nitrogen has a higher affinity for proton than the acetal. The increase in positive charge density on the aromatic ring deactivates the formation of the protonated acetal species, which is a necessary intermediate for ionization and hydrolysis to form the aldehyde (Scheme 6).

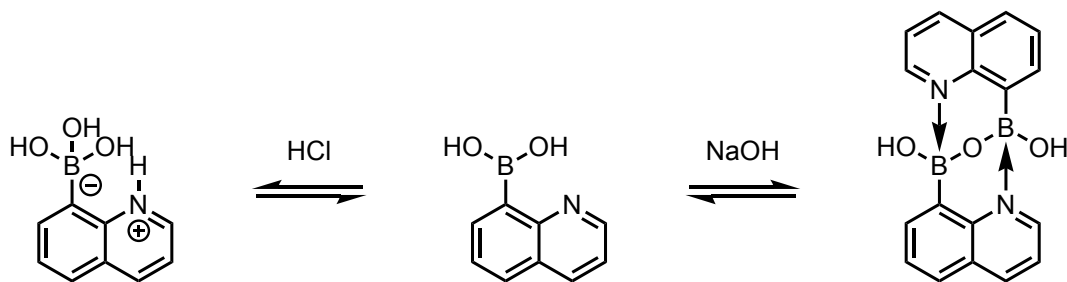
Scheme 7. The unusual stability of heteroaromatic acetals.



In retrospect, it is clear why initial attempts using typical acetal deprotection conditions—catalytic amounts of para-toluene sulfonic acid (p-TSA) in acetone—were unsuccessful. While we were able to achieve deprotection under highly acidic conditions (3.0 M HCl), the resulting product, **5**, is water soluble and highly reactive, making isolation challenging. Furthermore, careful attention is required during the neutralization of the reaction mixture. Under the strongly

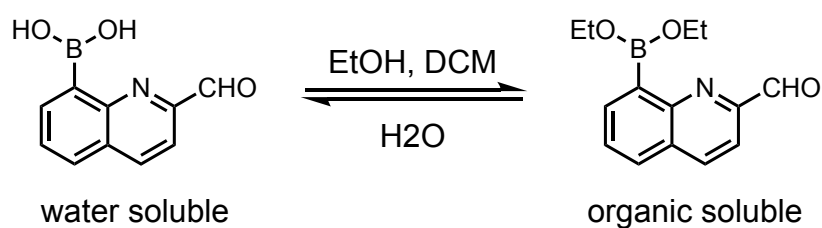
acidic conditions, the quinoline is protonated, forming a zwitterion with the tetrahedral boronate and making the compound highly water soluble (Scheme 7). On the other hand, if the solution becomes too basic, the boronic acids dimerize to form a complex mixture (Scheme 7).⁴¹

Scheme 8. The complex acid/base equilibrium of **8-QBA**



The amphiphilic nature of the **5** was addressed by dissolution in an ethanol/DCM/hexanes mixture. The boronic acid quinaldehyde should react with the ethanol to undergo esterification of the boronic acid, increasing the solubility in organic solvents (Scheme 8). After crystallization by slow evaporation, the compound is hydrolyzed by moisture under ambient conditions to access **5**.

Scheme 9. Solubility equilibrium of **5**



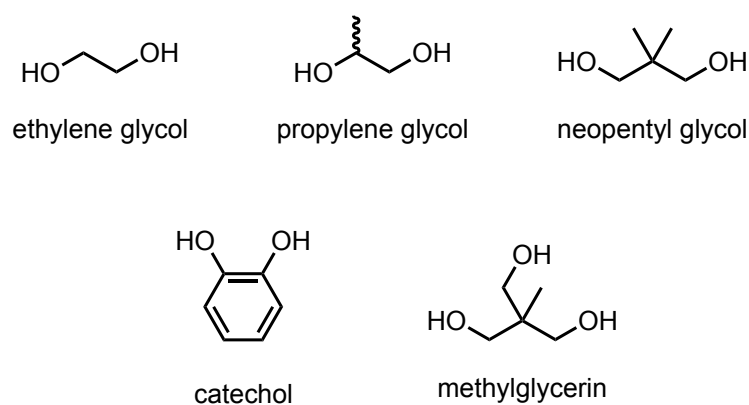
3.6 Hydrazone Condensation

Condensation of aldehyde **5** with an acyl hydrazide using a catalytic amount of acetic acid smoothly affords the photoswitch (*E*)-**PIC**_{acid}, which precipitates from the solution to afford pure

product. It is crucial for **5** to be sufficiently pure to cleanly access (*E*)-**PIC**_{acid} since column chromatography cannot be used to purify this final compound due to the high polarity and reactivity of the boronic acid, as well as its poor solubility in most organic solvents.

3.7 Esterification

Scheme 9. Some diols used to make boronic esters from (*E*)-**PIC**_{acid} and Me-QBA

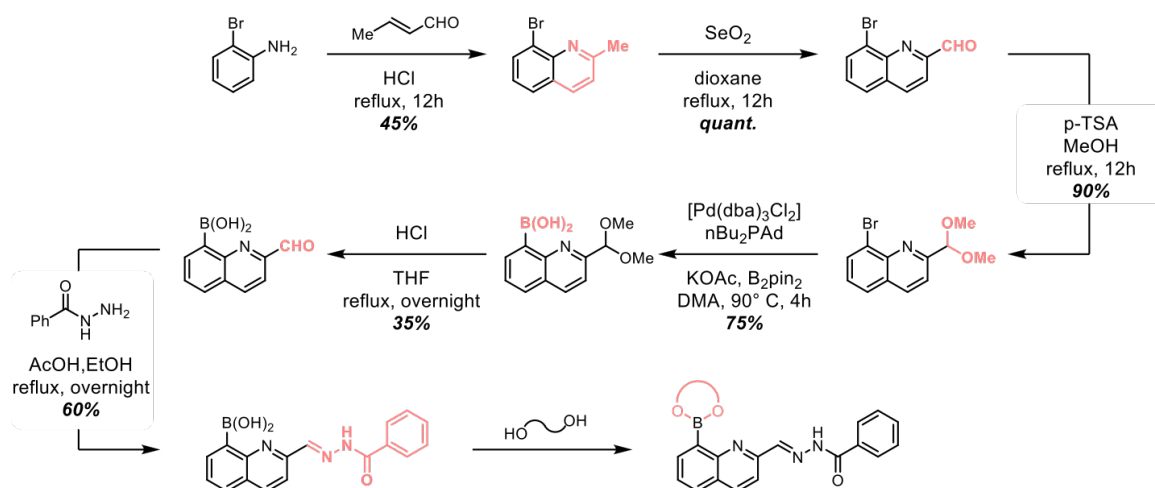


The final step of the synthesis of the target compound is esterification of (*E*)-**PIC**_{acid}. A variety of diols were used to synthesize boronic esters for different purposes (Scheme 9). Esterification of boronic acids is typically performed using an external base. We believed we could take advantage of the internal base component of our design to selectively synthesize the boronic ester without the need of an external base. (*E*)-**PIC**_{acid} showed low solubility in most organic solvents with the exception of DMF. Conveniently, and in addition to the internal base, the residual dimethylamine in DMF acts as base catalyst. A 1:2 mixture of (*E*)-**PIC**_{acid} and diol was heated in DMF for 1h before removal of the solvent to afford full conversion of the boronic acid to the corresponding boronic ester. Excess diol was used so subsequent kinetic studies could be performed with 1:1 boronic ester:diol.

3.9 Alternative Synthetic Routes

Due to the complications that rose during acetal deprotection and isolation, several alternative synthetic routes were attempted to access compound 5. As mentioned earlier, a dimethyl acetal was accessed by refluxing in methanol in the presence of a weak acid (p-TSA) instead of ethylene glycol (Scheme 10). While the acetal was easier to install, it appears that during deprotection this acetal is even more robust than the one derived from ethylene glycol.

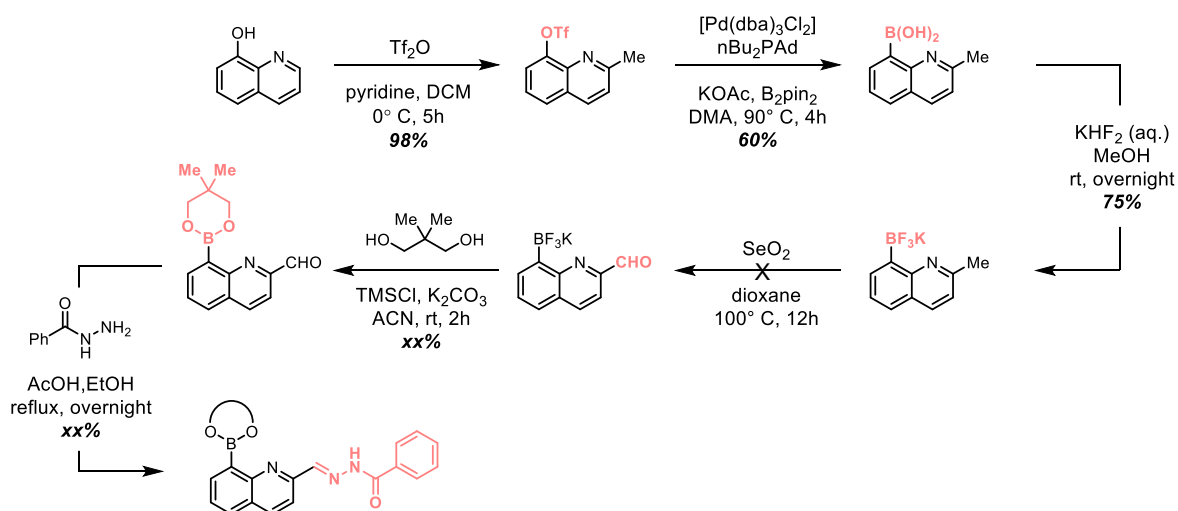
Scheme 10. Dimethyl acetal route



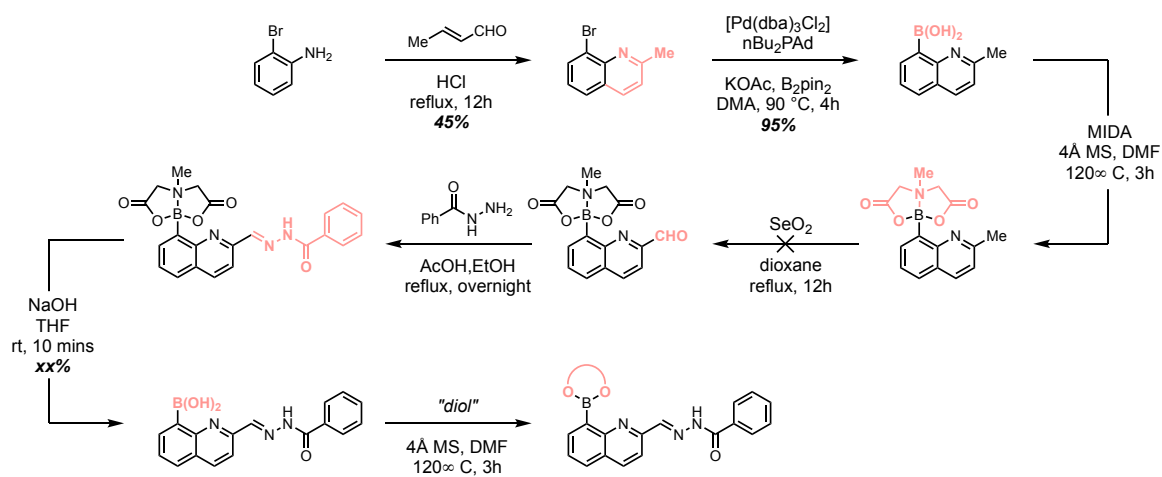
In an attempt to sidestep acetal protection all together, we chose to protect the boronic acid by accessing the BF_3K salt (Scheme 11) as well as through a MIDA protecting group (Scheme 12). In both cases, these protected analogs undergo very sluggish oxidation with SeO_2 . We opted not to explore these routes further without being able to push the reaction to completion, since

we are unable to use silica column to purify once the boron has been installed, even with the protecting groups.

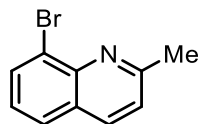
Scheme 11. BF₃K protection route



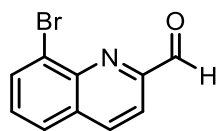
Scheme 12. MIDA protection route



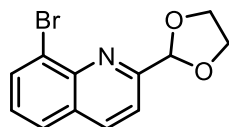
3.10 Synthetic Procedures



8-Bromo-2-methylquinoline (1) - To a solution of 2-bromoaniline (20.0 g, 116.4 mmol, 1.0 eq.) in 6N hydrochloric acid (60 ml) under reflux, crotonaldehyde (8.96 g, 128.0 mmol, 1.1 eq.) was added dropwise. After refluxing for 8 h, the reaction mixture was cooled down and washed with 80 ml of ether, followed by the addition of zinc chloride (15.8 g, 116.4 mmol, 1.0 eq.). The reaction mixture was stirred for 30 min at room temperature and an additional 15 min at 0°C to yield a yellow precipitate. The solid was collected and washed with 3N cold hydrochloric acid, and then suspended in 2-propanol (80 ml) and stirred for 5 min at room temperature. The solid was filtered and washed with 2-propanol until the washing became colorless, and then washed with 80 ml of ether and dried in air. The solid was suspended in 60 ml of cold water followed by the addition of 20 ml of concentrated ammonium hydroxide. The mixture was vigorously shaken and then extracted with ether (3 x 80 ml). After drying over magnesium sulfate and concentration, a dark solid product was obtained, which was purified by chromatography (EtOAc:Hexanes 10:90) to give a white solid product (11.6 g, 52.3 mmol, 45%). $^1\text{H NMR}$ (400 MHz, CDCl_3) δ 10.31 (d, $J = 0.9$ Hz, 1H), 8.33 (d, $J = 7.5$ Hz, 1H), 8.17 (dd, $J = 7.4, 1.3$ Hz, 1H), 8.10 (d, $J = 8.4$ Hz, 1H), 7.89 (dd, $J = 8.2, 1.3$ Hz, 1H), 7.55 (dd, $J = 8.2, 7.5$ Hz, 1H); $^{13}\text{C NMR}$ (126 MHz, CDCl_3) δ 160.61, 144.98, 136.71, 133.20, 127.93, 127.61, 126.19, 124.31, 123.00, 77.16, 25.87. **LRMS:** m/z expected for $\text{C}_{10}\text{H}_8\text{BrN}$ $[\text{M}+\text{H}]^+$ 220.98, measured 220.96.

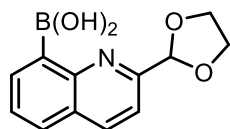


8-bromoquinoline-2-carbaldehyde (2) - A 100 ml Schlenk tube charged with SeO_2 (2.75 g, 24.8 mmol, 1.1 eq.) and a magnetic stir bar was purged with N_2 for 5 min. 1,4-dioxane (44 ml) was added and the mixture was heated to 80 °C before adding 8-bromo-2-methylquinoline (**1**) (5.00 g, 22.5 mmol, 1.0 eq.) under a stream of N_2 . The dark mixture was maintained at 80 °C for 12 hours, cooled to room temperature, the precipitate was filtered, and the filtrate was again filtered through alumina eluting with CH_2Cl_2 . Solvent was removed on a rotary evaporator to give the pure product as a tan solid (5.3 g, 22.5 mmol, >95%). In some cases further purification is required by chromatography (EtOAc:Hex 10:90) $^1\text{H NMR}$ (400 MHz, CDCl_3) δ 8.03 (d, J = 8.4 Hz, 1H), 8.01 (dd, J = 7.4, 1.3 Hz, 1H), 7.74 (dd, J = 8.1, 1.3 Hz, 1H), 7.34 (d, J = 8.2 Hz, 2H), 7.32 (d, J = 8.2 Hz, 1H), 2.82 (s, 3H). $^{13}\text{C NMR}$ (126 MHz, CDCl_3) δ 193.54, 153.25, 145.21, 138.25, 134.38, 131.52, 129.64, 127.85, 126.31, 118.24, 77.16. **LRMS**: m/z expected for $\text{C}_{10}\text{H}_6\text{BrNO}$ $[\text{M}+\text{H}]^+$ 234.96, measured 234.98.



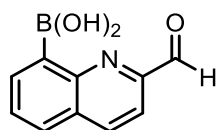
8-bromo-2-(1,3-dioxolan-2-yl)quinoline (3) - 8-bromoquinoline-2-carbaldehyde (**2**) (1.0g, 4.24mmol, 1.0 eq.), ethylene glycol (0.329g, 5.3 mmol, 1.25 eq.), p-toluenesulfonic acid monohydrate (49 mg, 0.26mmol, 0.061 eq.), and toluene (10mL) were added to a round bottom flask equipped with a Dean-Stark apparatus. The orange heterogenous mixture becomes deep red

and homogenous after being heated to 125 °C. After 48 hours, the reaction was allowed to cool to room temperature. Toluene was removed by rotovap and the crude product was dissolved in DCM and washed with Na₂CO₃ (1% w/w in H₂O). After drying over Na₂SO₄, the solvent was removed. The compound was purified by silica gel column eluting with Hexanes/Ethyl Acetate, starting from 95:5 and ramping up to 80:20 to afford the pure product as an orange oil (0.77 g, 2.75 mmol, 65%). **¹H NMR** (400 MHz, CDCl₃) δ 8.21 (dd, J = 48.1, 8.5 Hz, 1H), 8.06 (dd, J = 7.5, 1.3 Hz, 1H), 7.79 (dd, J = 8.1, 1.3 Hz, 1H), 7.70 (d, J = 8.5 Hz, 1H), 7.41 (dd, J = 8.1, 7.5 Hz, 1H), 6.06 (s, 1H), 4.31 – 4.11 (m, 4H). **¹³C NMR** (126 MHz, CDCl₃) δ 158.47, 144.58, 137.66, 133.44, 129.69, 127.59, 127.44, 125.28, 119.15, 104.24, 65.94. **LRMS:** m/z expected for C₁₂H₁₀BrNO₂ [M+H]⁺ 278.99, measured 278.98.



(2-(1,3-dioxolan-2-yl)quinolin-8-yl)boronic acid (4) – The following experiment was adapted from reference 39: To a dry and Schlenk flask containing a magnetic stir bar were charged with **3** (470 mg, 1.68 mmol, 1.0 eq.), pinacol bis(pinacolato)diboron (512 mg, 2.02 mmol, 1.2 eq.), Pd₂(dba)₃ (15.4 mg, 16.8 μmol, 0.01 eq.), n-BuPAd₂ (18.0 mg, 50.4 μmol, 0.03 eq.), KOAc (495 mg, 5.04 mmol, 3.0 eq.), and DMAc (1.5 mL) under nitrogen. Then the reaction mixture was heated at 90 °C. After 1.5 h, the reaction mixture was cooled to room temperature, and 40 mL of water was added slowly. The solid was collected by filtration and washed sequentially with 20 mL of water and 15 mL of toluene and then dried under vacuum to give the pure product as a pale yellow solid (0.39 g, 1.60 mmol, 95%). **¹H NMR** (500 MHz, CDCl₃) δ 8.68 (bs, 2H), 8.43 (d, J =

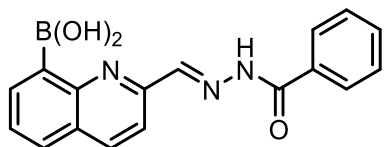
6.8 Hz, 1H), 8.29 (d, $J = 8.5$ Hz, 1H), 7.93 (d, $J = 8.1$ Hz, 1H), 7.71 – 7.57 (m, 1H), 6.03 (s, 1H), 4.27 – 4.12 (m, 4H); ^{13}C NMR (126 MHz, CDCl_3) δ 156.07, 151.20, 138.73, 138.53, 130.70, 128.03, 127.40, 118.15, 103.86, 77.16, 65.97; ^{11}B NMR (160 MHz, CDCl_3) δ 29.96. **LRMS:** m/z expected for $\text{C}_{12}\text{H}_{12}\text{BNO}_4$ $[\text{M}+\text{H}]^+$ 245.09, measured 245.10.



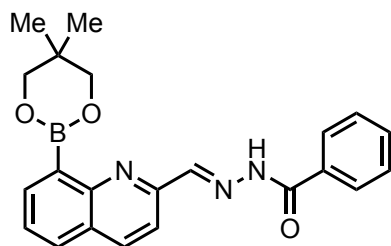
(2-formylquinolin-8-yl)boronic acid (5) – HCl (10 mL, 3.0 M) was added to a solution of **4** (0.490 g, 2.0 mmol, 1.0 eq.) in tetrahydrofuran (10 mL). The mixture was stirred at 60 °C overnight. The solution was cooled to room temperature and neutralized with NaOH (10 mL, 3.0 M) and extracted by dichloromethane and ethanol (9:1 DCM:EtOH, 3 x 50 mL). The organic layer was washed with water and brine, dried over Na_2SO_4 and filtered. After the solvent was removed in vacuo, the flask was triturated with hexanes to remove any protodeborelated quinoline. The crude product was recrystallized in dichloromethane and a minimal amount of ethanol, layered with hexanes to afford **5** (0.16 g, 0.82 mmol, 41%) as a light pink solid. ^1H NMR (500 MHz, CDCl_3) δ 10.26 (d, $J = 0.9$ Hz, 1H), 8.53 (dd, $J = 6.9, 1.6$ Hz, 1H), 8.43 (dd, $J = 8.4, 0.9$ Hz, 1H), 8.09 (d, $J = 8.4$ Hz, 1H), 8.07 – 7.97 (m, 3H), 7.78 (dd, $J = 8.2, 6.8$ Hz, 1H); ^{13}C NMR (126 MHz, CDCl_3) δ 192.25, 151.61, 150.76, 139.50, 139.13, 130.92, 130.03, 129.42, 117.12; ^{11}B NMR (160 MHz, CDCl_3) δ 29.72. **LRMS:** m/z expected for $\text{C}_{10}\text{H}_8\text{BNO}_3$ $[\text{M}+\text{H}]^+$ 201.06, measured 201.05.

Note: Several complications arise during the synthesis and isolation of **5** that make yields/purity inconsistent. First, when subjecting compound **4** to acidic conditions, protonation of the quinoline nitrogen results in an increase in positive charge density, slowing protonation of the acetal and

hindering full conversion.² Incomplete acetal deprotection leads to issues in isolation of **5**. Second, careful attention must be paid to the neutralization of the strongly acidic reaction mixture due to the intricate equilibria that lead to a complex mixture of dimerized and zwitterionic species.³

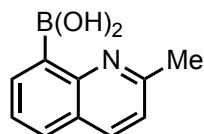
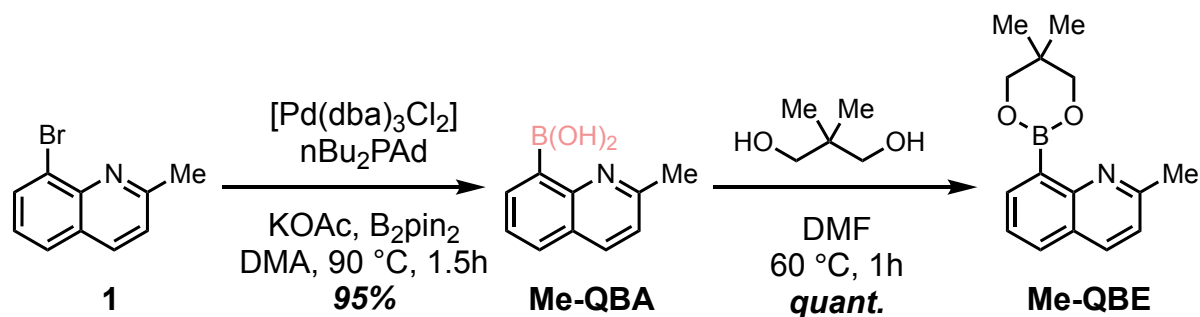


(E)-PIC_{acid} – Benzoyl hydrazide (109 mg, 0.8 mmol, 1.0 eq.) and **5** (160 mg, 0.8 mmol, 1.0 eq.) were suspended in EtOH (1.5 mL). Subsequently, a catalytic amount of acetic acid was added and the mixture was heated to reflux. After 30 minutes, the reaction is cooled to room temperature during which the product precipitates from solution and was filtered off to yield the pure acylhydrazone without need for further purification (204 mg, 0.64 mmol, 80%). **¹H NMR** (500 MHz, DMSO-*d*₆) δ 12.23 (s, 1H), 9.48 (s, 2H), 8.72 (s, 1H), 8.56 (d, *J* = 8.6 Hz, 1H), 8.31 (d, *J* = 6.8 Hz, 1H), 8.18 (d, *J* = 8.6 Hz, 1H), 8.14 (d, *J* = 8.1 Hz, 1H), 7.98 (d, *J* = 7.6 Hz, 2H), 7.70 (t, *J* = 7.4 Hz, 1H), 7.64 (t, *J* = 7.3 Hz, 1H), 7.57 (t, *J* = 7.5 Hz, 2H); **¹³C NMR** (126 MHz, DMSO-*d*₆) δ 163.30, 152.40, 151.09, 147.08, 138.60, 138.09, 132.89, 132.19, 130.79, 129.54, 128.62, 127.74, 127.34, 117.22, 39.52; **¹¹B NMR** (160 MHz, CDCl₃) δ 28.95. **LRMS**: *m/z* expected for C₁₇H₁₄BN₃O₃ [M+H]⁺ 319.11, measured 319.13.



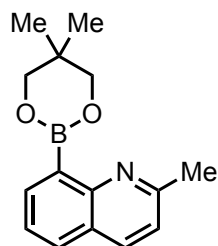
(E)-PIC_{ester} – **(E)-PIC_{acid}** (31.9 mg, 0.1 mmol, 1.0 eq.) and 2.0 equivalents of neopentyl glycol (20.8 mg, 0.2 mmol) were dissolved in DMF (1 mL). The mixture was stirred for 1 hour before removing the DMF under reduced pressure on a rotovap at 60 °C. The resulting mixture was dissolved in toluene-d₈ and acetone-d₆ (0.1 M, 9:1 toluene:acetone) and used for kinetics experiments without further purification.

Scheme 13. Synthesis of **Me-QBA** and **Me-QBE**



(2-(methyl)quinolin-8-yl)boronic acid (Me-QBA) – The following experiment was adapted from reference 39: To a dry and clean Schlenk flask containing a magnetic stir bar were charged with

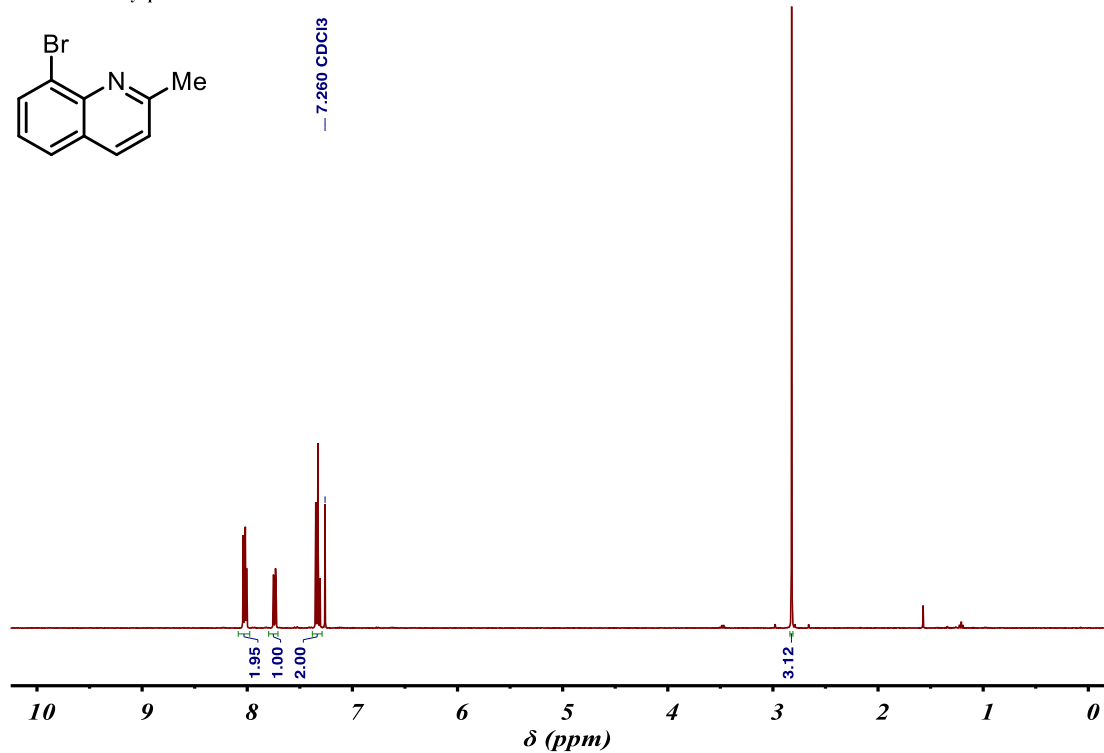
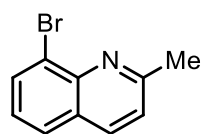
1 (373 mg, 1.68 mmol, 1.0 eq.), pinacol bis(pinacolato)diboron (512 mg, 2.02 mmol, 1.2 eq.), Pd₂(dba)₃ (15.4 mg, 16.8 μmol, 0.01 eq.), n-BuPAD₂ (18.0 mg, 50.4 μmol, 0.03 eq.), KOAc (494 mg, 5.04 mmol, 3.0 eq.), and DMAc (1.5 mL) under nitrogen. Then the reaction mixture was heated at 90 °C. After 1.5 h, the reaction mixture was cooled to room temperature, and 40 mL of water was added slowly. The solid was collected by filtration and washed sequentially with 20 mL of water and 15 mL of toluene and then dried under vacuum to give the pure product as a pale yellow solid (0.30 g, 1.6 mmol, 95%). ¹H NMR (500 MHz, CDCl₃) δ 8.37 (dd, *J* = 6.9, 1.5 Hz, 1H), 8.12 (d, *J* = 8.4 Hz, 1H), 7.88 (dd, *J* = 8.1, 1.6 Hz, 1H), 7.56 (t, *J* = 6.9 Hz, 1H), 7.32 (d, *J* = 8.4 Hz, 1H), 2.77 (s, 3H); ¹³C NMR (126 MHz, CDCl₃) δ 157.90, 151.91, 138.00, 137.74, 130.64, 126.09, 126.07, 121.75, 25.31; ¹¹B NMR (160 MHz, CDCl₃) δ 30.03. LRMS: *m/z* expected for C₁₂H₁₂BNO₄ [M+H]⁺ 187.08, measured 187.09.



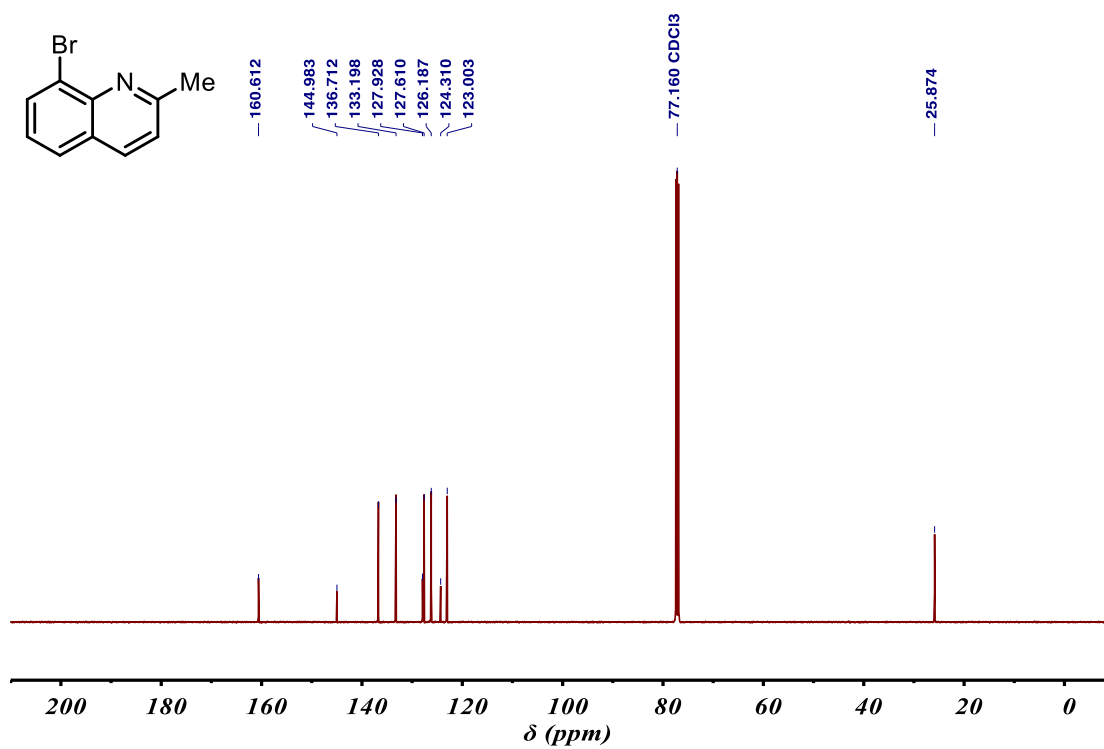
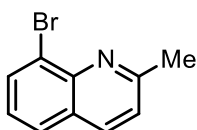
Me-QBE – (18.7 mg, 0.1 mmol, 1.0 eq.) and 2.0 equivalents of neopentyl glycol (20.8 mg, 0.2 mmol) were dissolved in DMF (1 mL). The mixture was stirred for 1 hour before removing the DMF under reduced pressure on a rotovap at 60 °C. The resulting mixture was dissolved in toluene-d₈ and acetone-d₆ (0.1 M, 9:1 toluene:acetone) and used for kinetics experiments without further purification.

3.11 NMR data

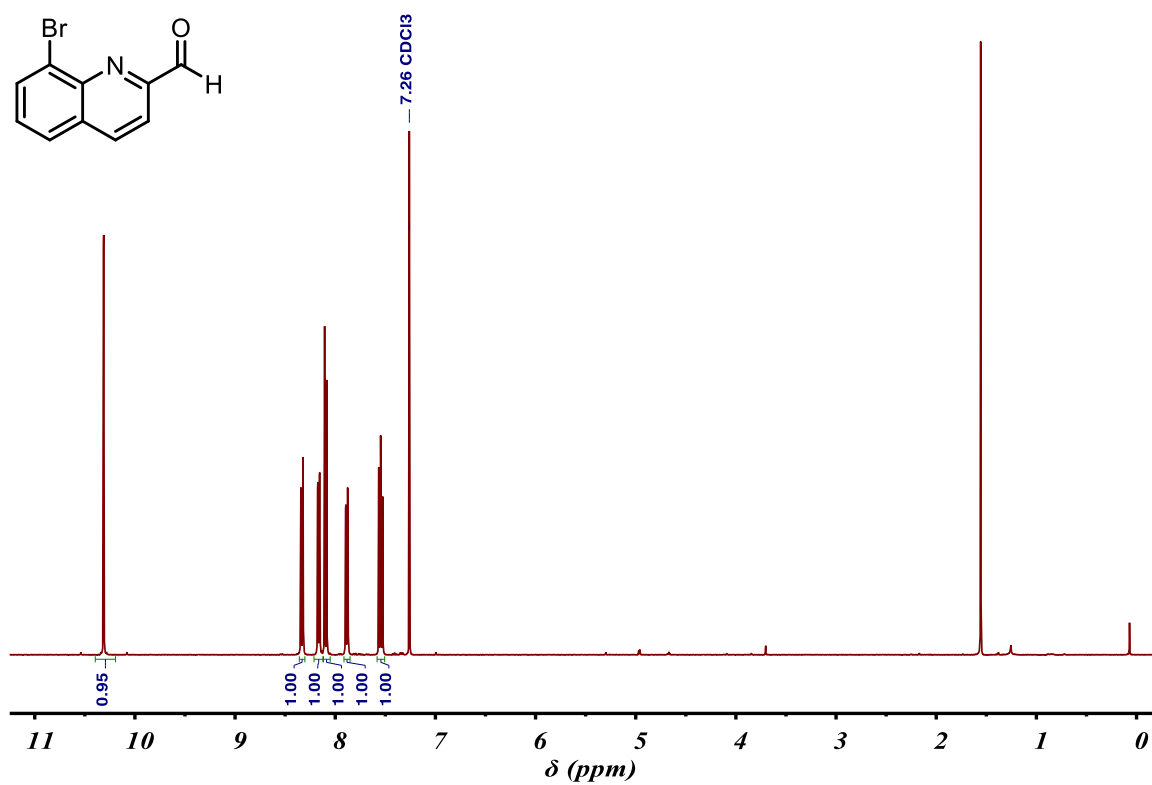
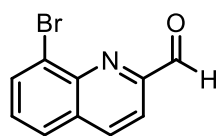
8-bromo-2-methylquinoline



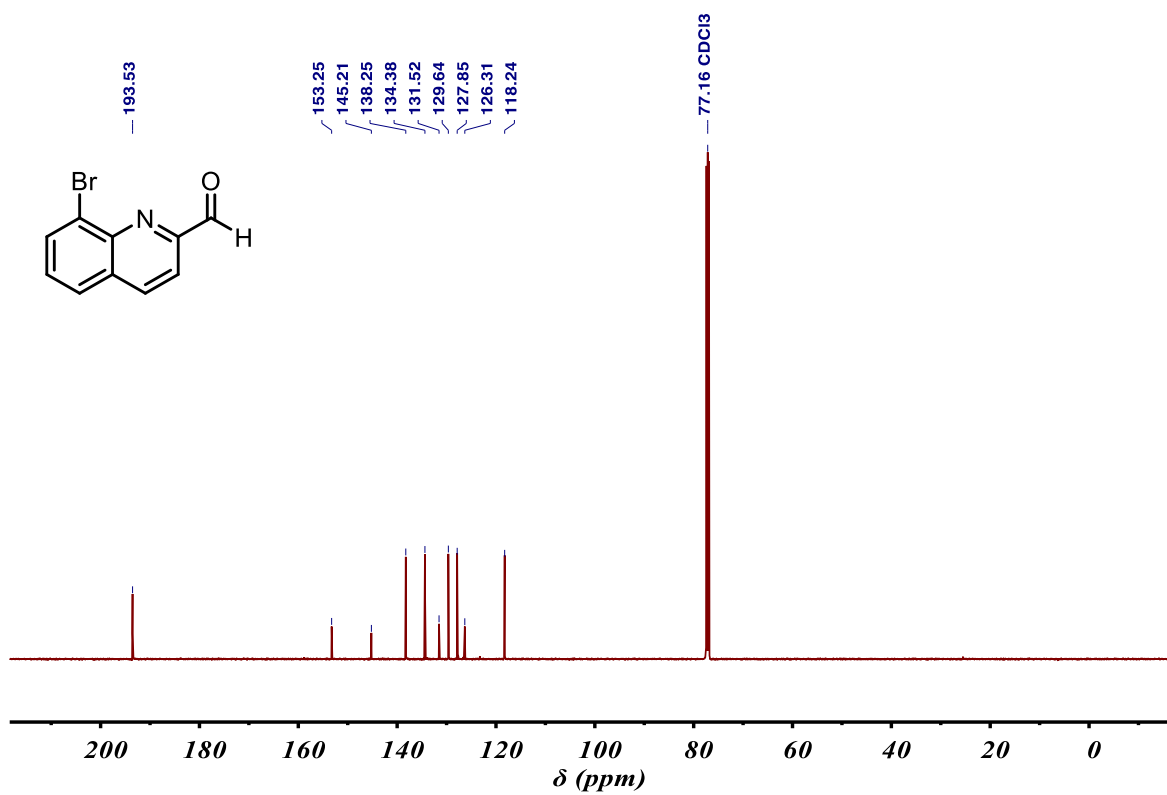
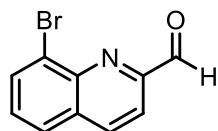
8-bromo-2-methylquinoline



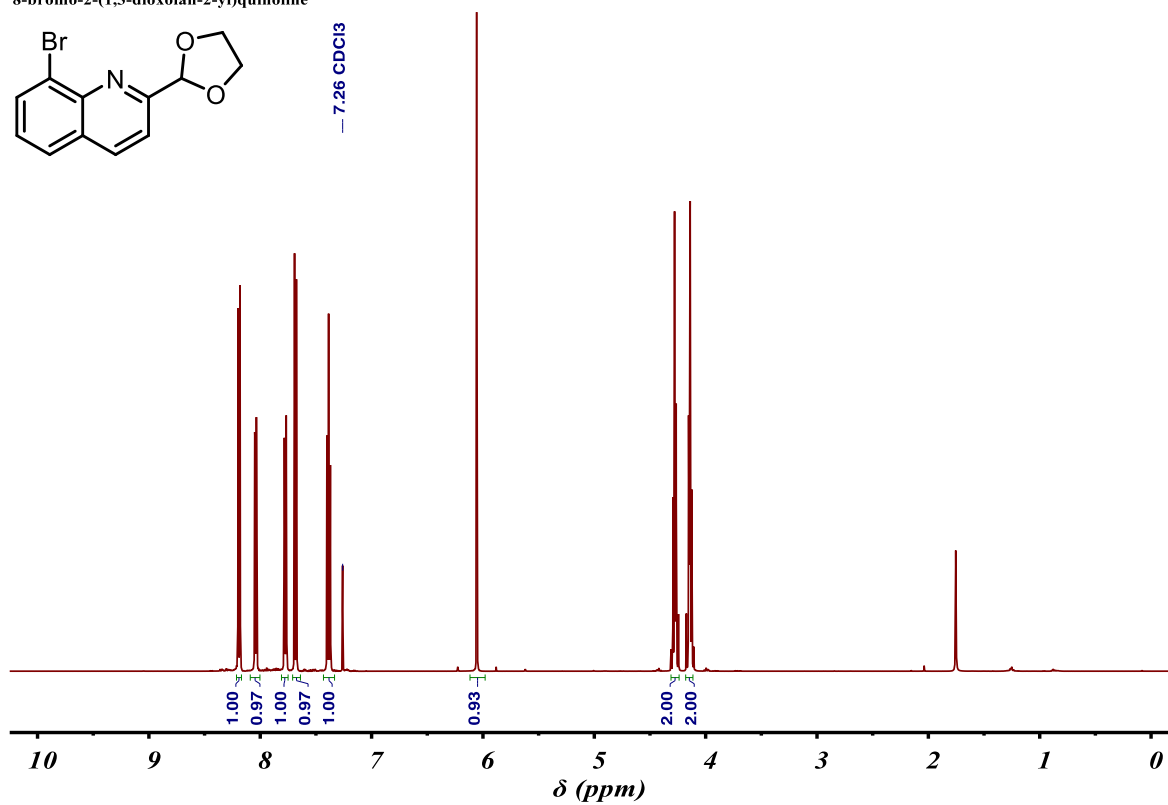
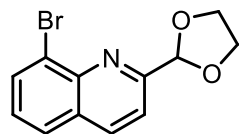
8-bromoquinoline-2-carbaldehyde



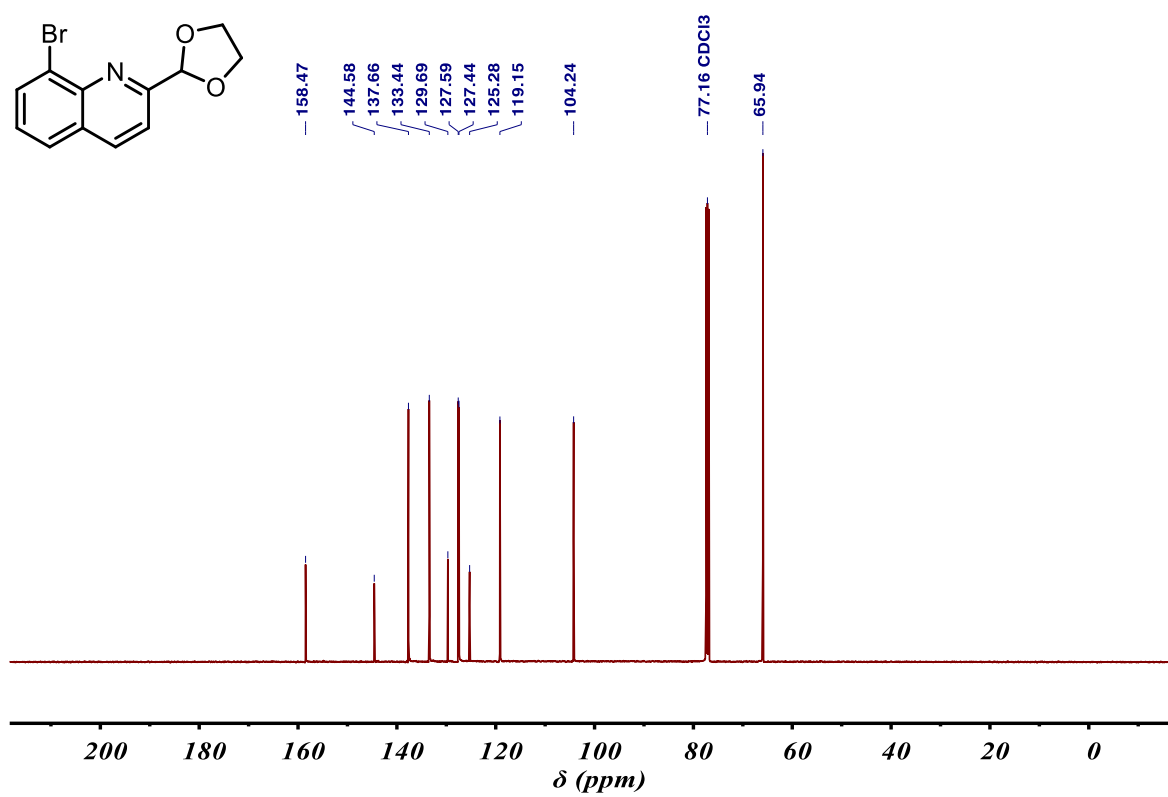
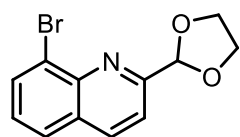
8-bromoquinoline-2-carbaldehyde



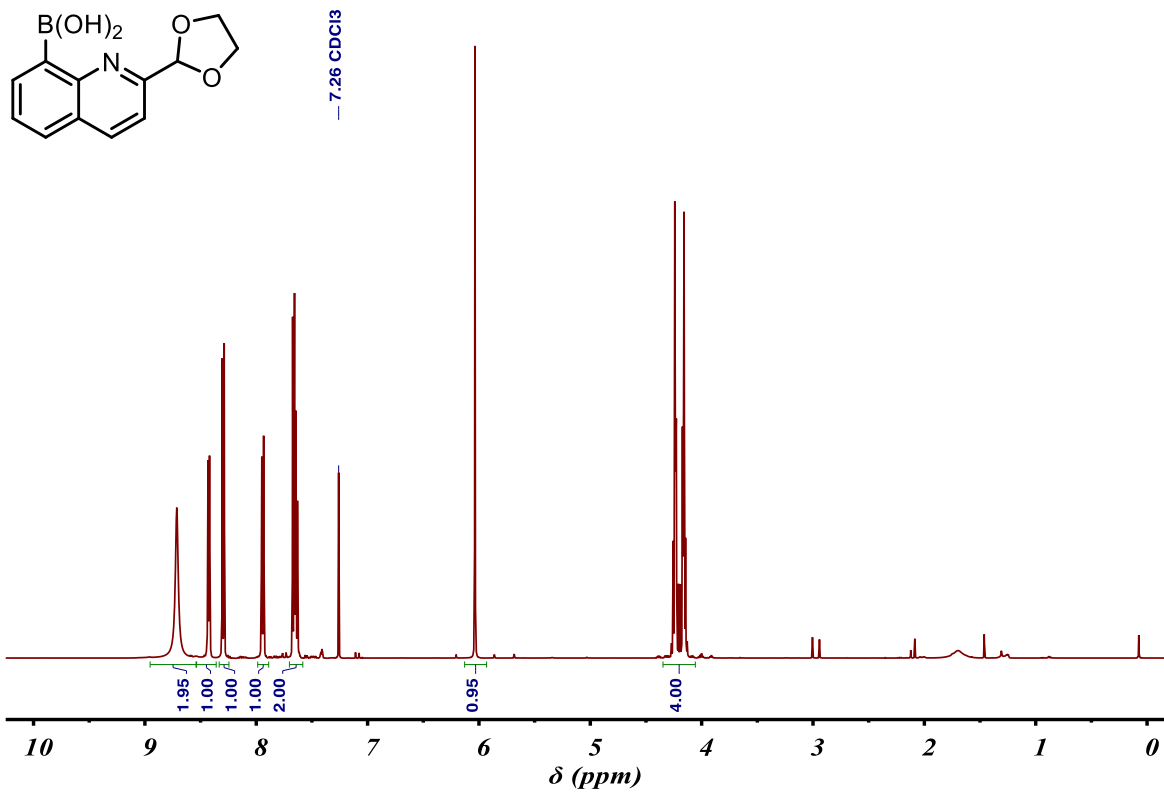
8-bromo-2-(1,3-dioxolan-2-yl)quinoline



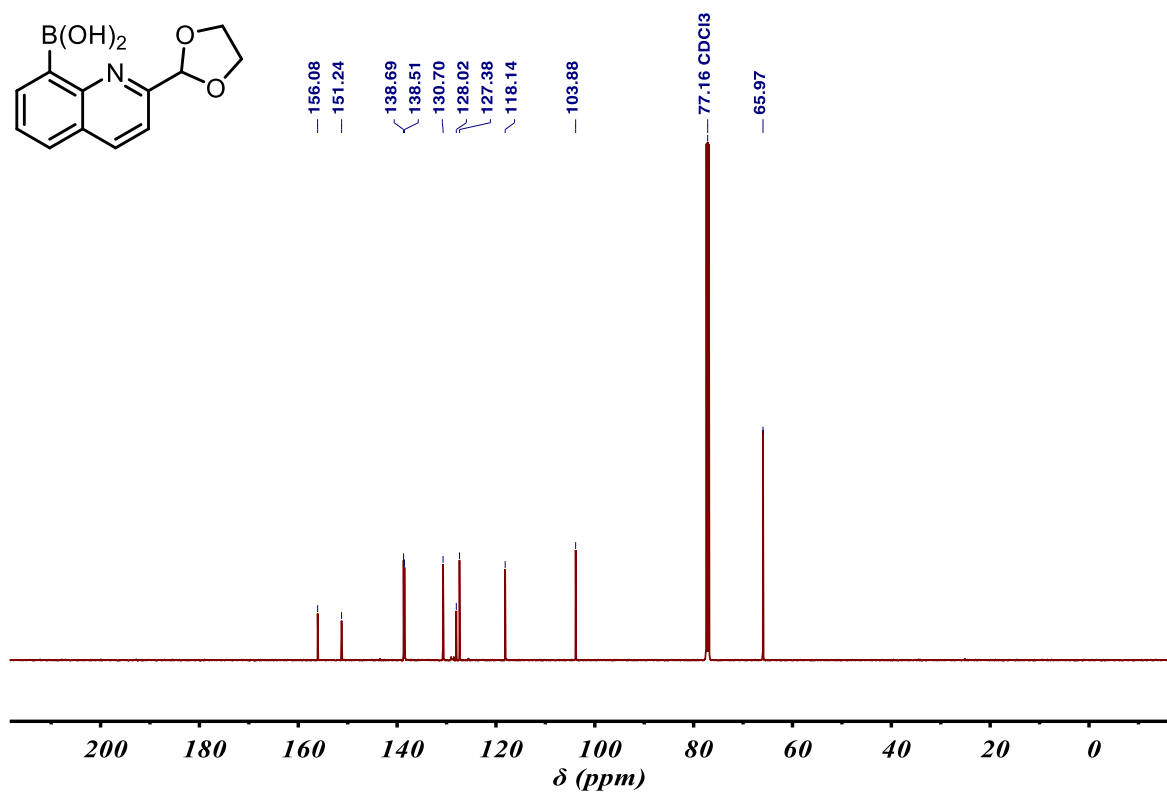
8-bromo-2-(1,3-dioxolan-2-yl)quinoline



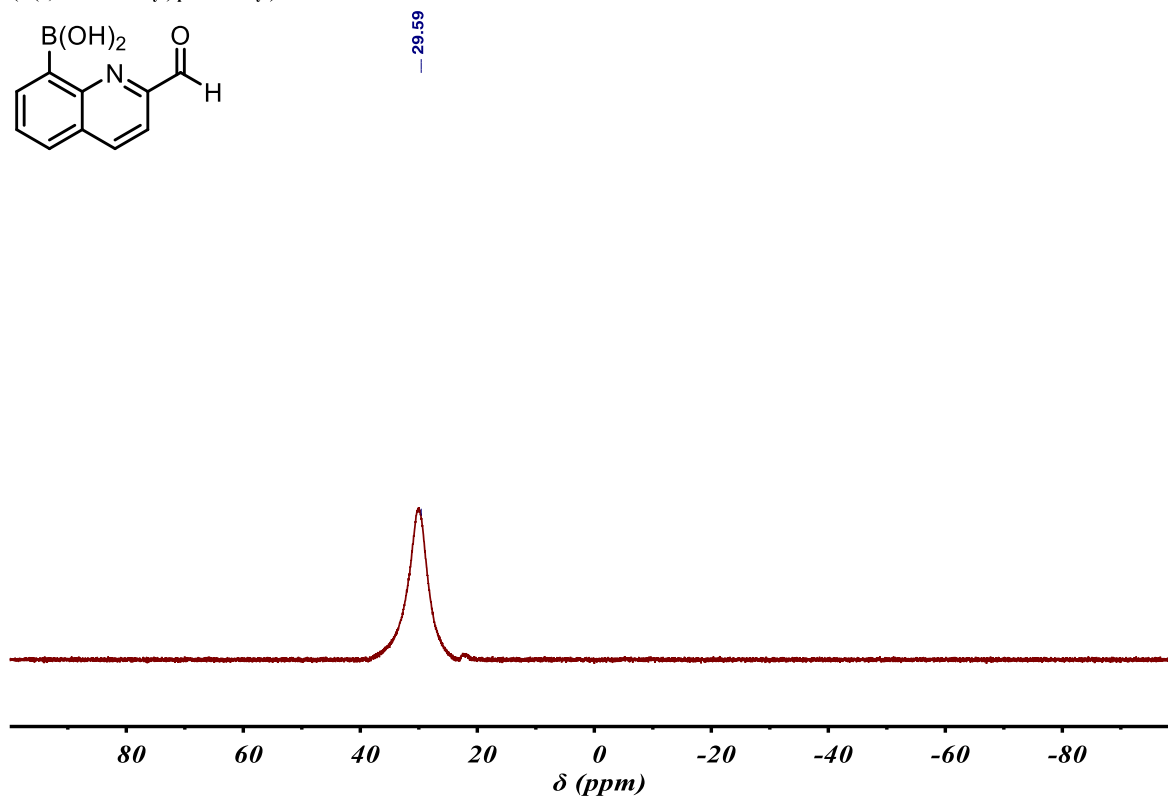
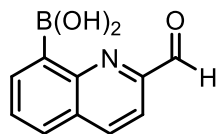
(2-(1,3-dioxolan-2-yl)quinolin-8-yl)boronic acid



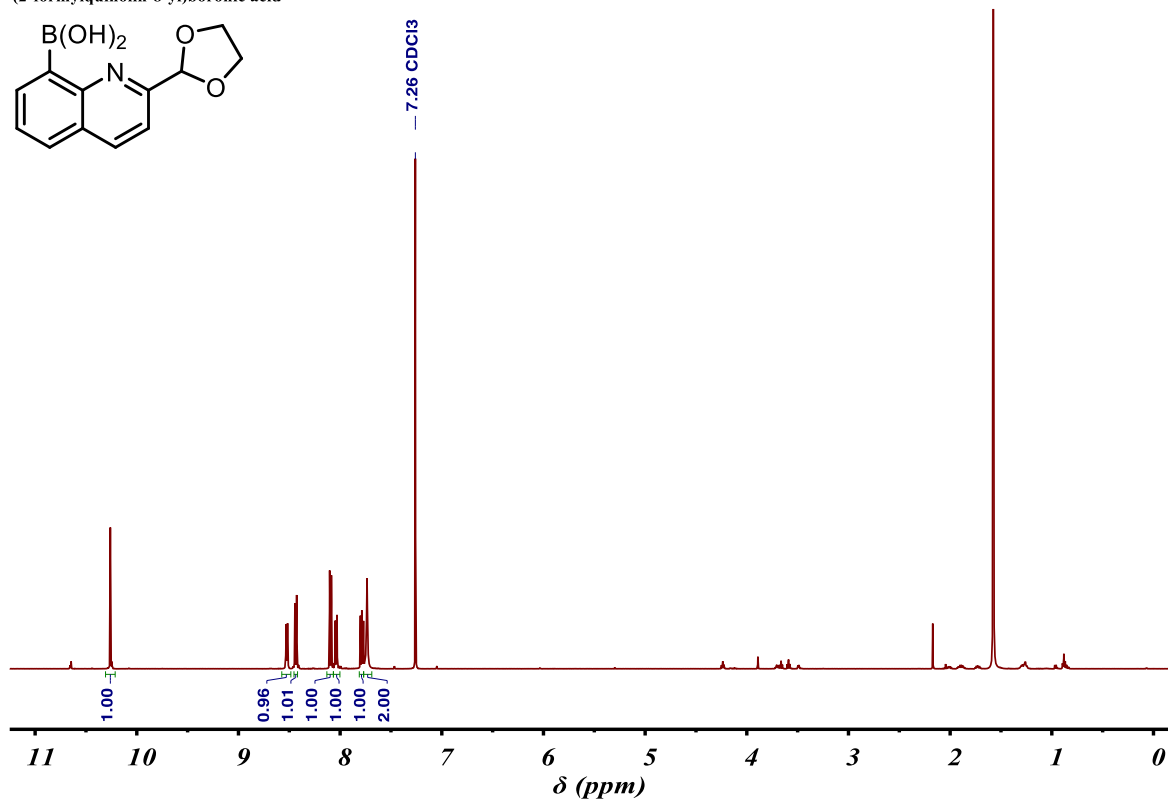
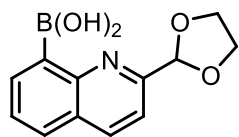
(2-(1,3-dioxolan-2-yl)quinolin-8-yl)boronic acid



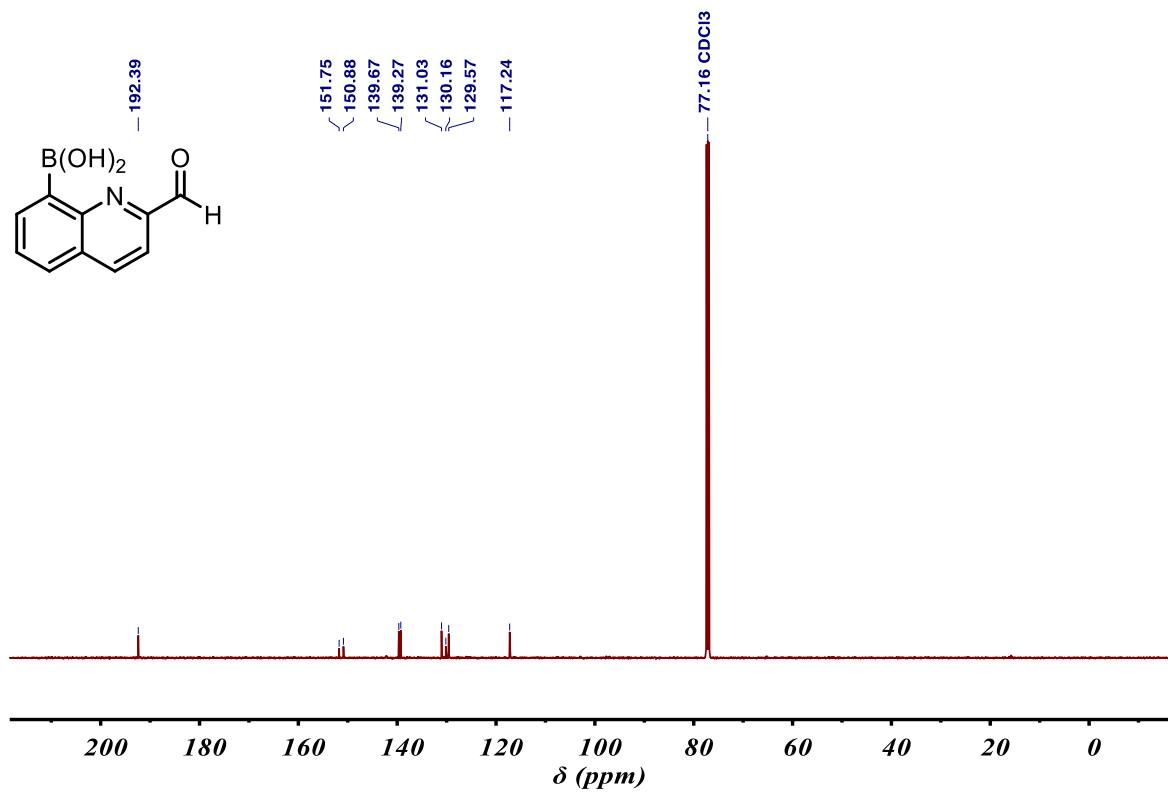
(2-(1,3-dioxolan-2-yl)quinolin-8-yl)boronic acid



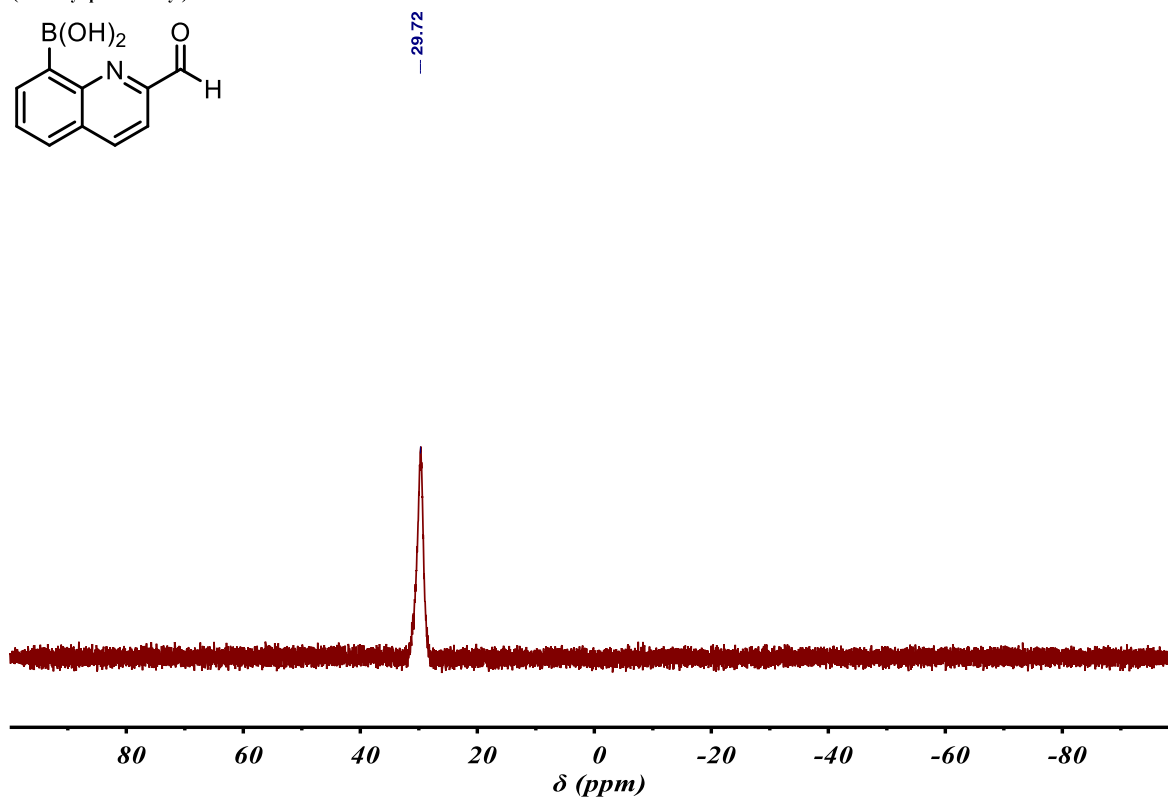
(2-formylquinolin-8-yl)boronic acid



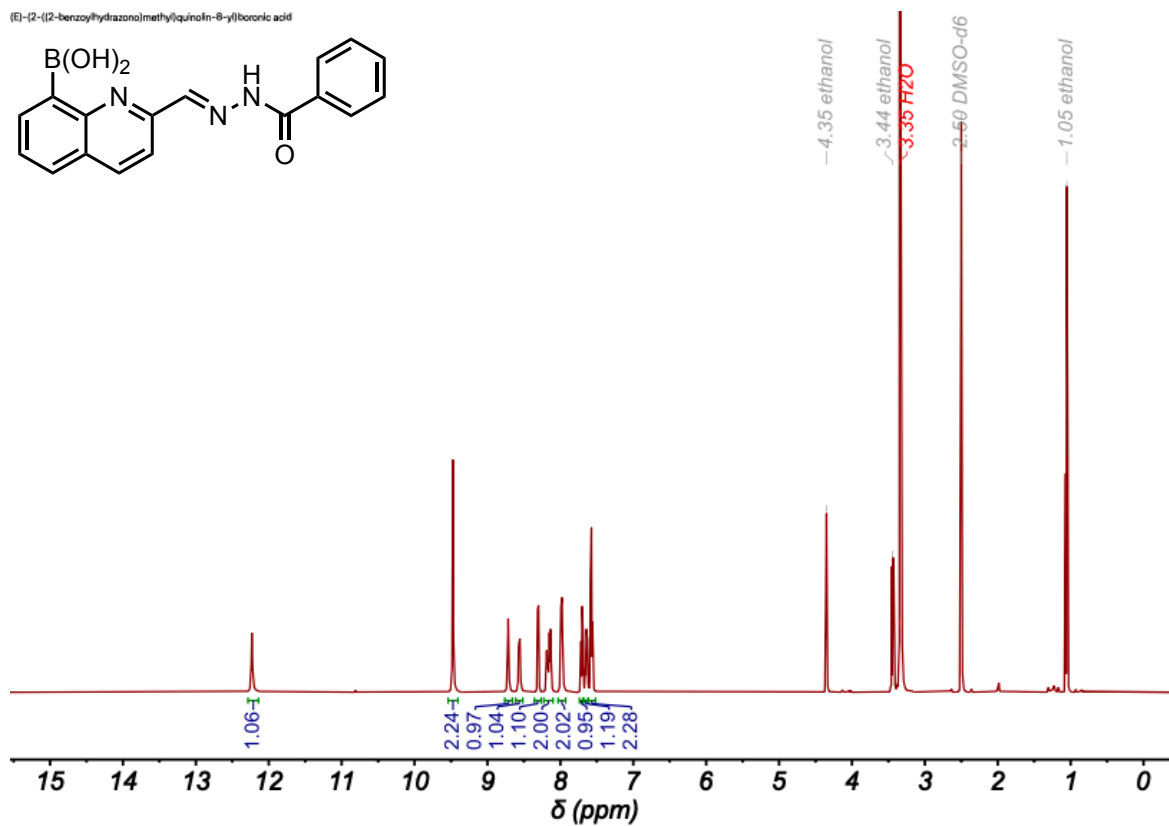
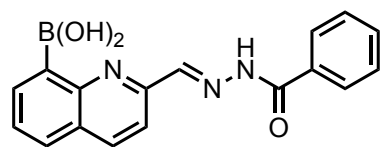
(2-formylquinolin-8-yl)boronic acid



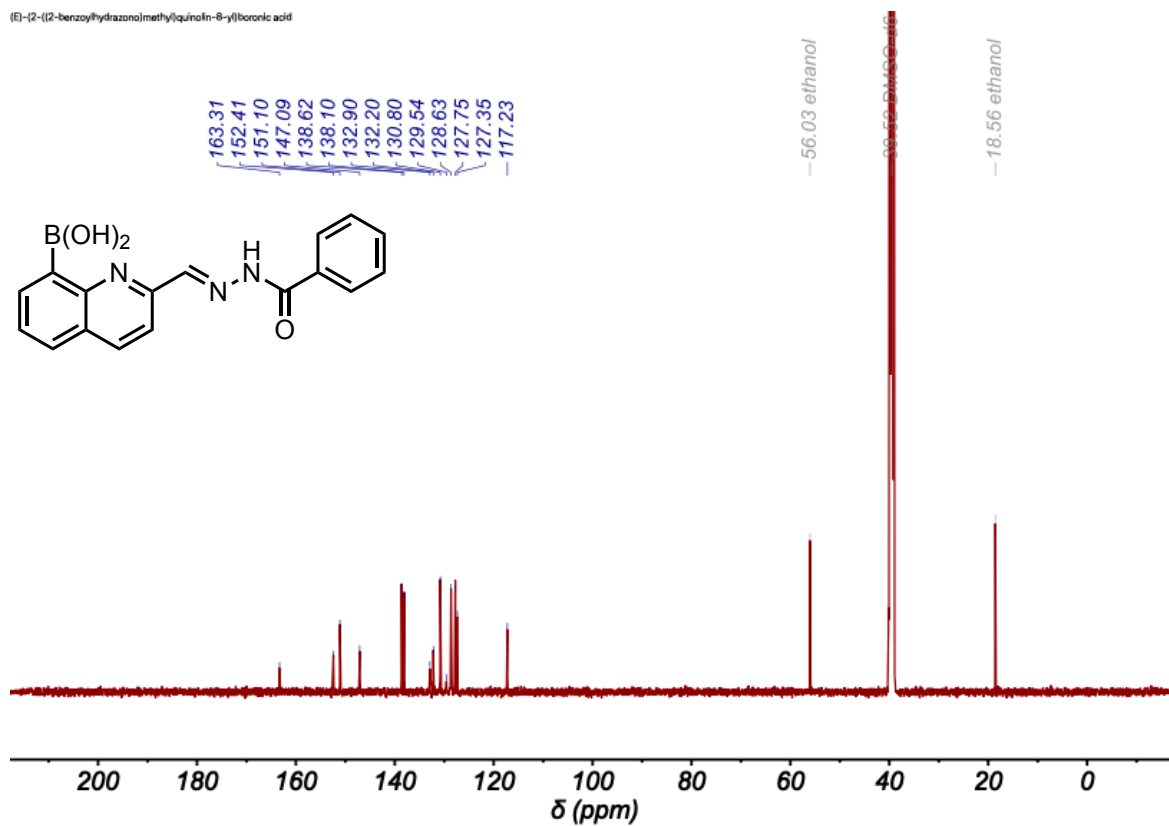
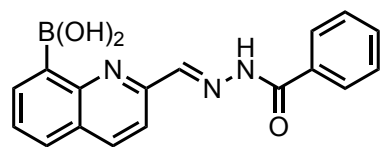
(2-formylquinolin-8-yl)boronic acid



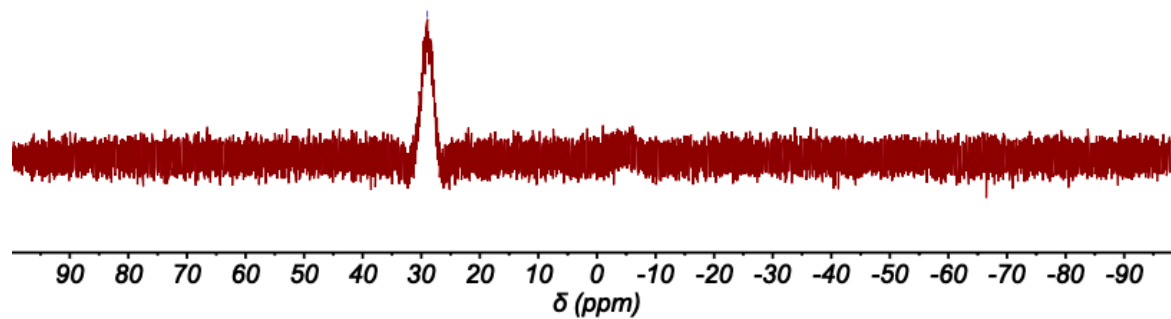
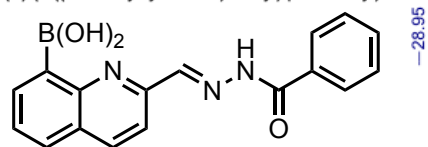
[E]-2-((2-benzoylhydrazono)methyl)quinolin-8-yl)boronic acid



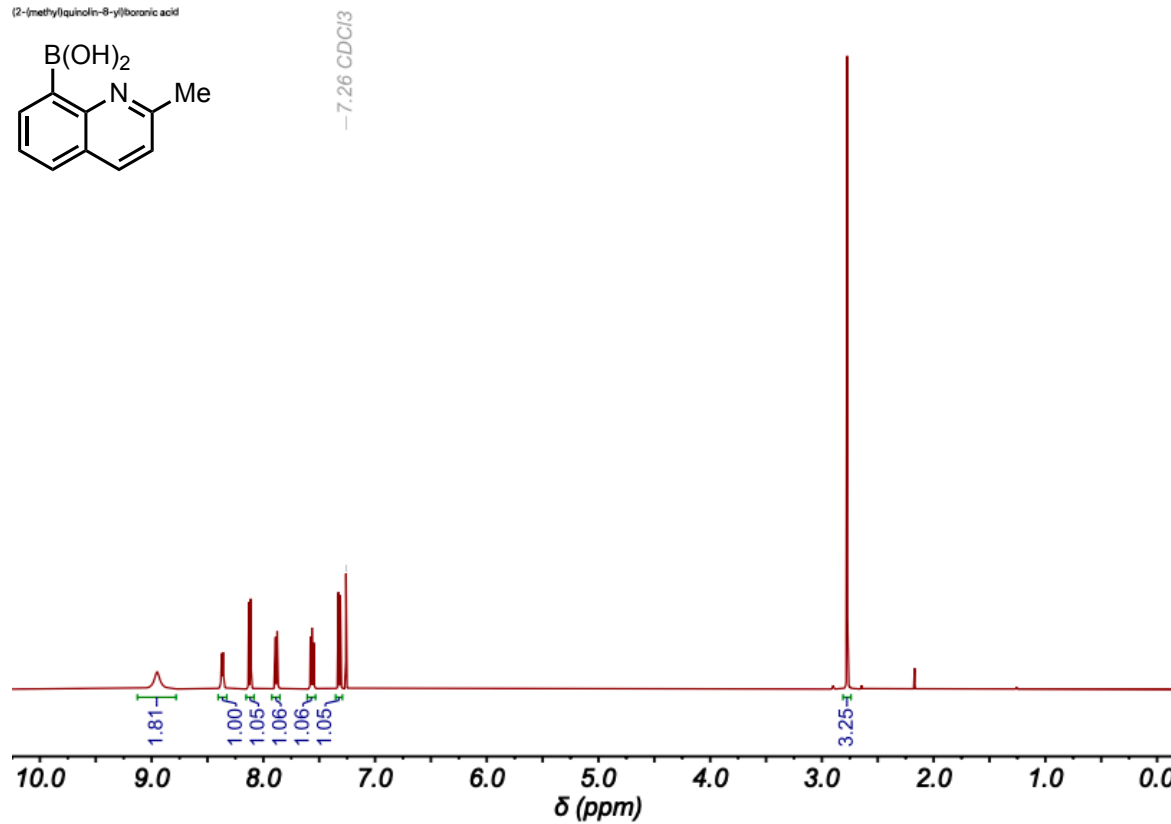
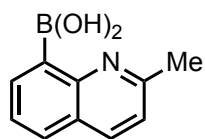
[E]-2-((2-benzoylhydrazono)methyl)quinolin-8-yl)boronic acid



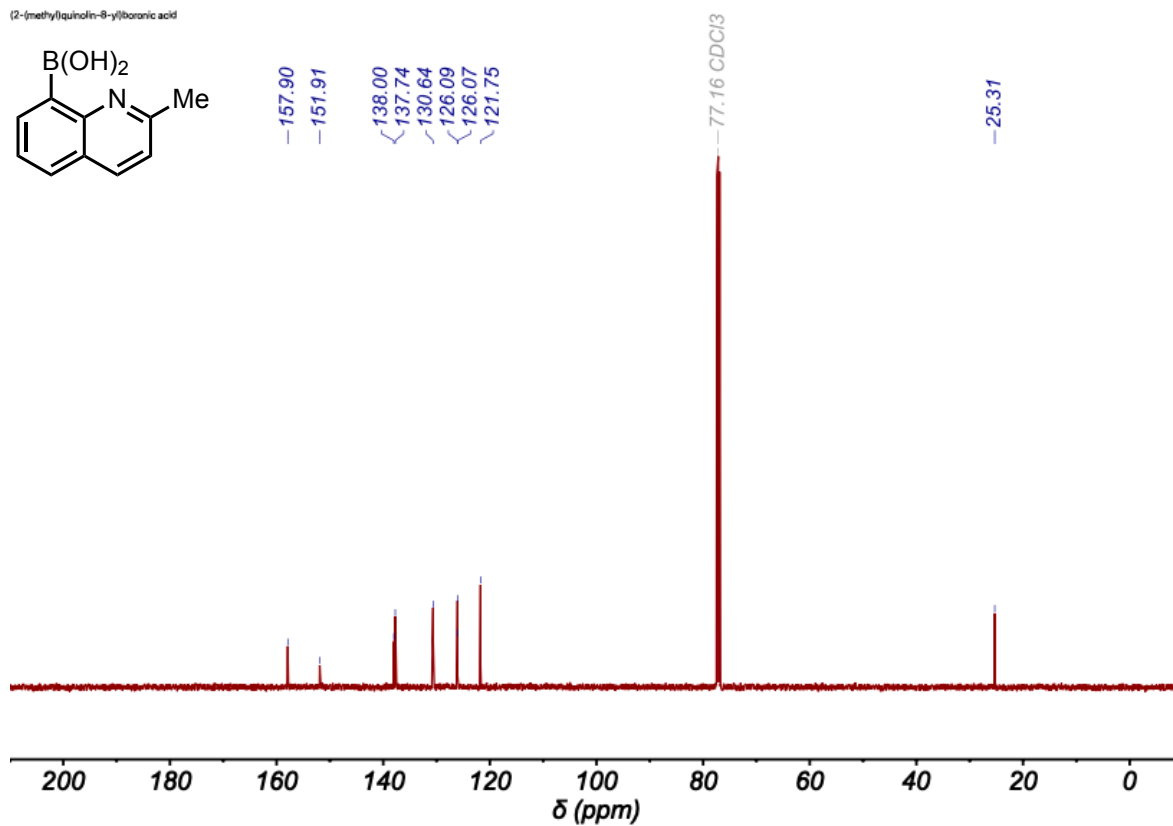
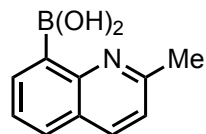
(E)-2-((2-benzoylhydrazono)methyl)quinolin-8-yl)boronic acid



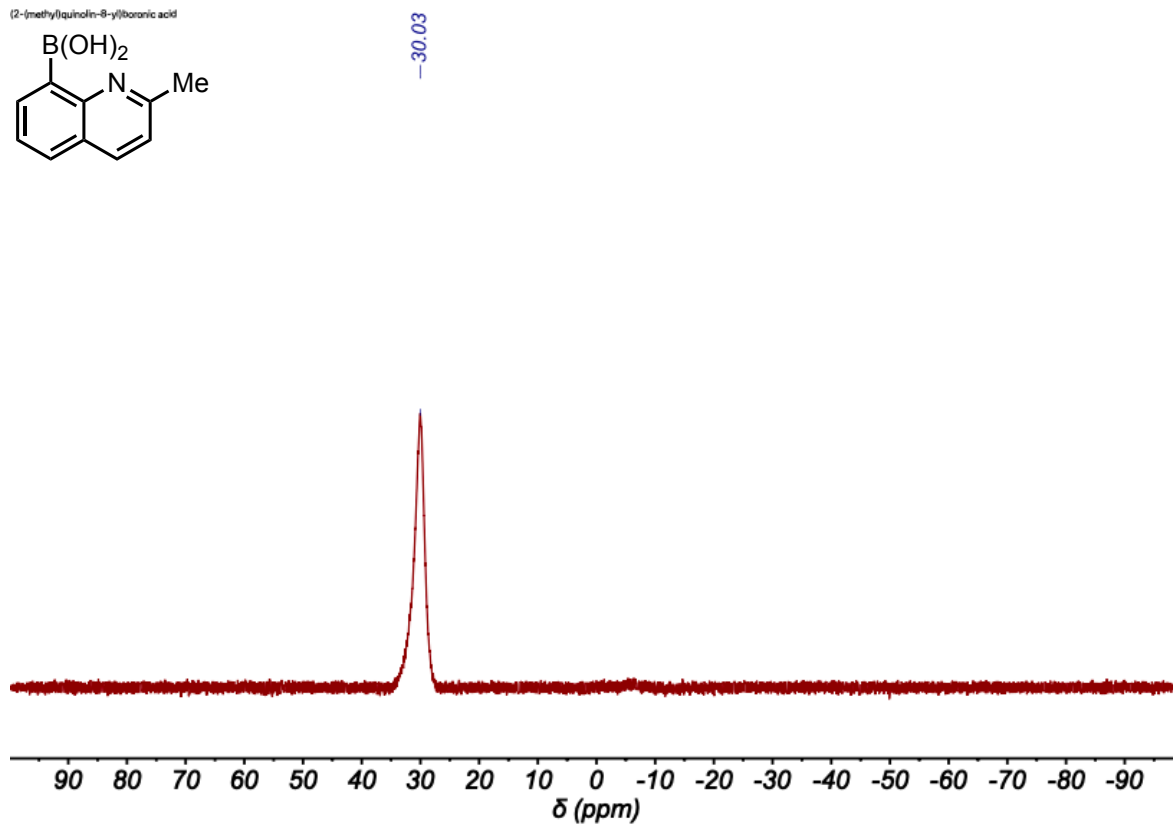
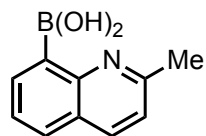
(2-(methyl)quinolin-8-yl)boronic acid



(2-(methyl)quinolin-8-yl)boronic acid



(2-(methyl)quinolin-8-yl)boronic acid



4.1 Photostationary State

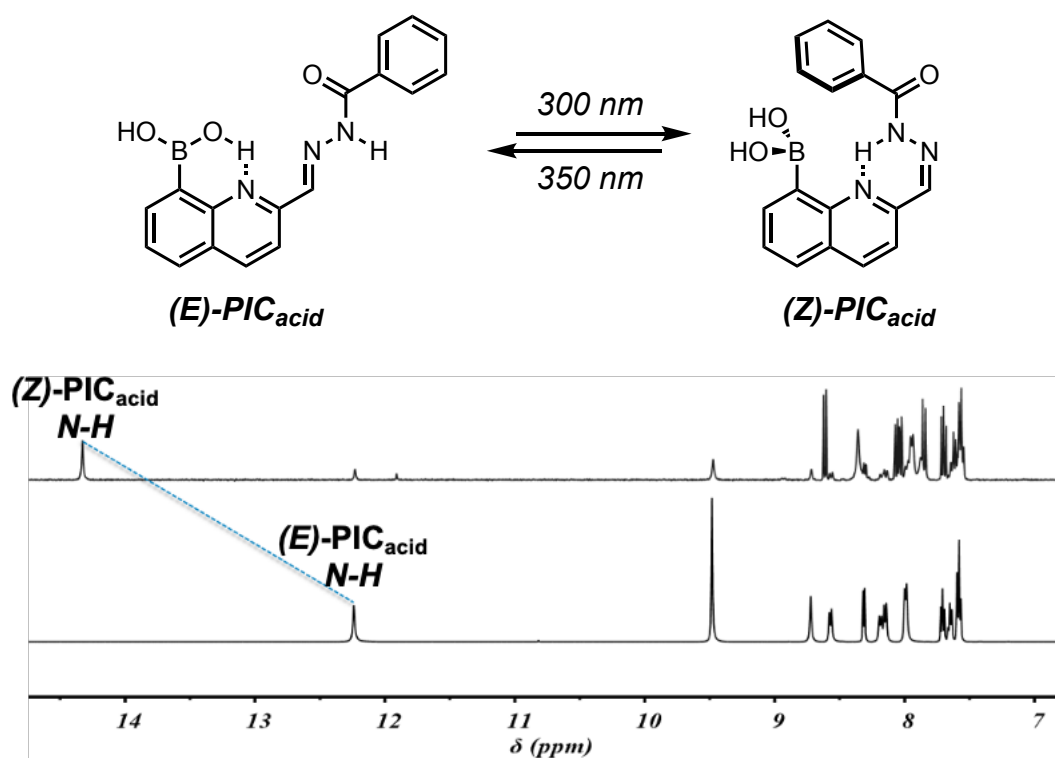


Figure 11. ¹H NMR of the aromatic region of *(E)*- and *(Z)*-PIC_{acid} shows the N–H peak shift downfield after isomerization from *E* to *Z*.

First, we investigated the photoisomerization of the boronic acid *(E)*-PIC_{acid} by monitoring the conversion from *E* to *Z* by ¹H NMR. Initially, a sharp singlet appears at 12.2 ppm in the *E*-isomer, corresponding to the acyl hydrazone N–H bond. After irradiation at 300 nm, the peak shifts downfield to 14.5 ppm, indicating the formation of a strong intramolecular H-bond (Figure 11). The *Z*-isomer is thermally stabilized due to the intramolecular H-bond and can be stored for weeks with no observable back isomerization, even when subjected to elevated temperatures (70 °C). Irradiation at 300 nm promotes efficient conversion from *(E)*-PIC_{acid} → *(Z)*-PIC_{acid}, reaching a

photostationary state (PSS) of 92%. Although the *Z* isomer is thermally stable, when irradiated with 350 nm light, the *Z*→*E* isomerization proceeds with a PSS of 67%.

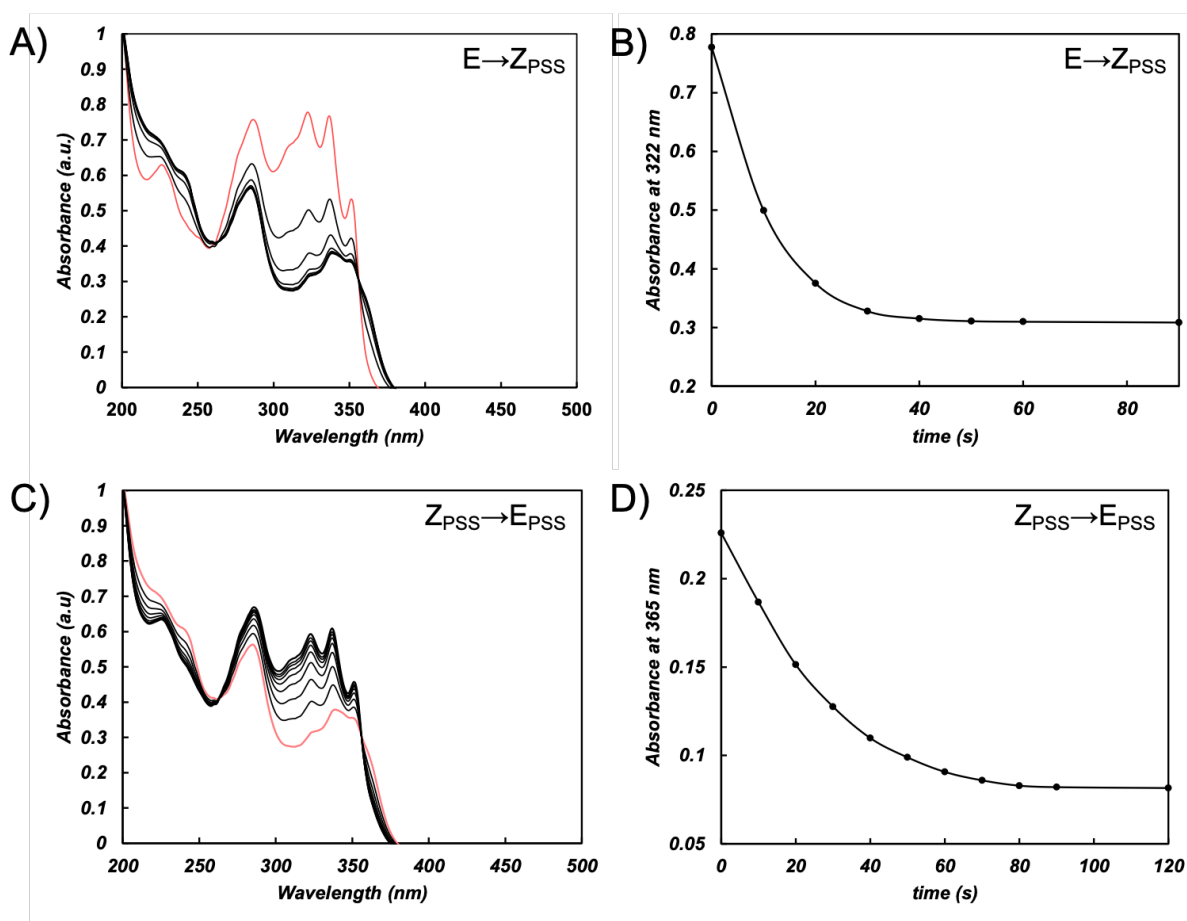


Figure 12. (A) Conversion of (*E*)-PIC_{acid} (red line) in MeCN (1.56×10^{-5} M) to (*Z*)-PIC_{acid,PSS} (black line) followed in time under constant irradiation ($\lambda_{\text{irr}} = 300$ nm, $t_{\text{irr}} = 90$ sec); IP at 336 nm. (B) Absorbance followed at $\lambda_{\text{max}}(E) = 322$ nm over time as in (A). (C) Conversion of (*Z*)-PIC_{acid,PSS} (red line) to (*E*)-PIC_{acid,PSS} in MeCN (black line) followed in time ($\lambda_{\text{irr}} = 350$ nm, $t_{\text{irr}} = 120$ sec). (D) Absorbance followed at $\lambda_{\text{max}}(Z) = 365$ nm over time as in (C).

4.2 Fatigue Resistance

The fatigue resistance of other hydrazone photoswitches is generally quite high (up to 300 cycles).^{30,32} UV-Vis absorption of (*E*)-PIC_{acid} and (*Z*)-PIC_{acid} show significant spectral overlap, but a 10-nm bathochromic shift in the absorption onset of the *Z* isomer provides enough spectral separation to selectively irradiate both isomers (Figure 13A). Using UV-Vis, we monitored *E*→*Z* isomerization over time and found that the PSS is reached in less than 1 minute in acetonitrile at 1.56×10^{-5} M (figure 13A,B). *Z*→*E* isomerization also reaches (*E*)-PIC_{acid} PSS in less than 2 minutes (figure 12C,D, enabling rapid switching between both isomers. Monitoring the UV-Vis absorption of PIC_{acid} at 322 nm during alternating irradiation at 300 and 350 nm, we observe no loss in efficiency after 10 cycles under ambient conditions (Figure 13B). Therefore, the presence of a boronic acid does not affect the robustness of the hydrazone photoswitch.

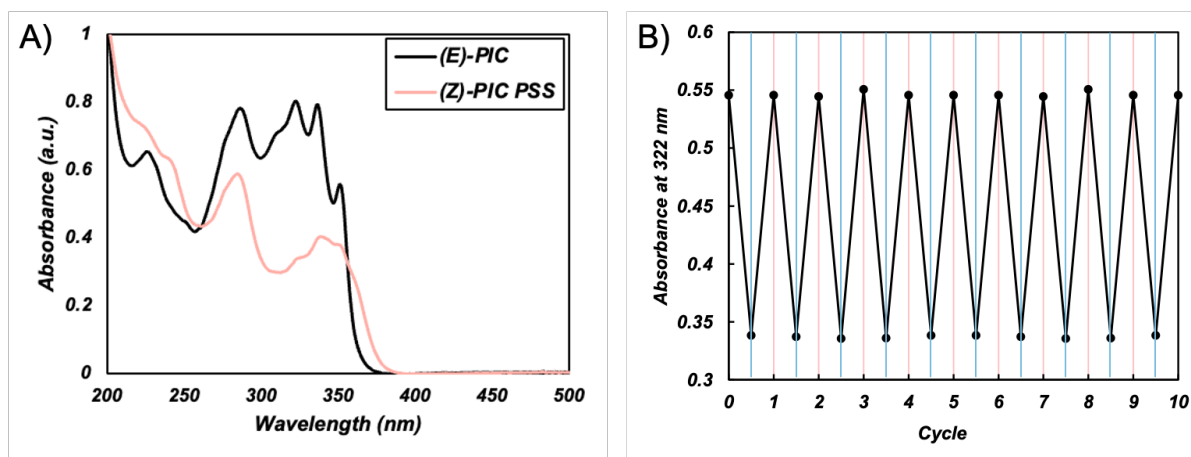


Figure 13. A) UV-Vis absorbance of (*E*)-PIC_{acid} (black line) and the photostationary state of (*Z*)-PIC_{acid} photostationary state (red line) in acetonitrile at 1.56×10^{-5} M. B) Corresponding absorbance of PIC_{acid} after irradiation at 300 nm (blue lines) and 350 nm (red lines).

4.3 Quantitative Conversion of (*E*)-PIC_{ester} and (*Z*)-PIC_{ester}

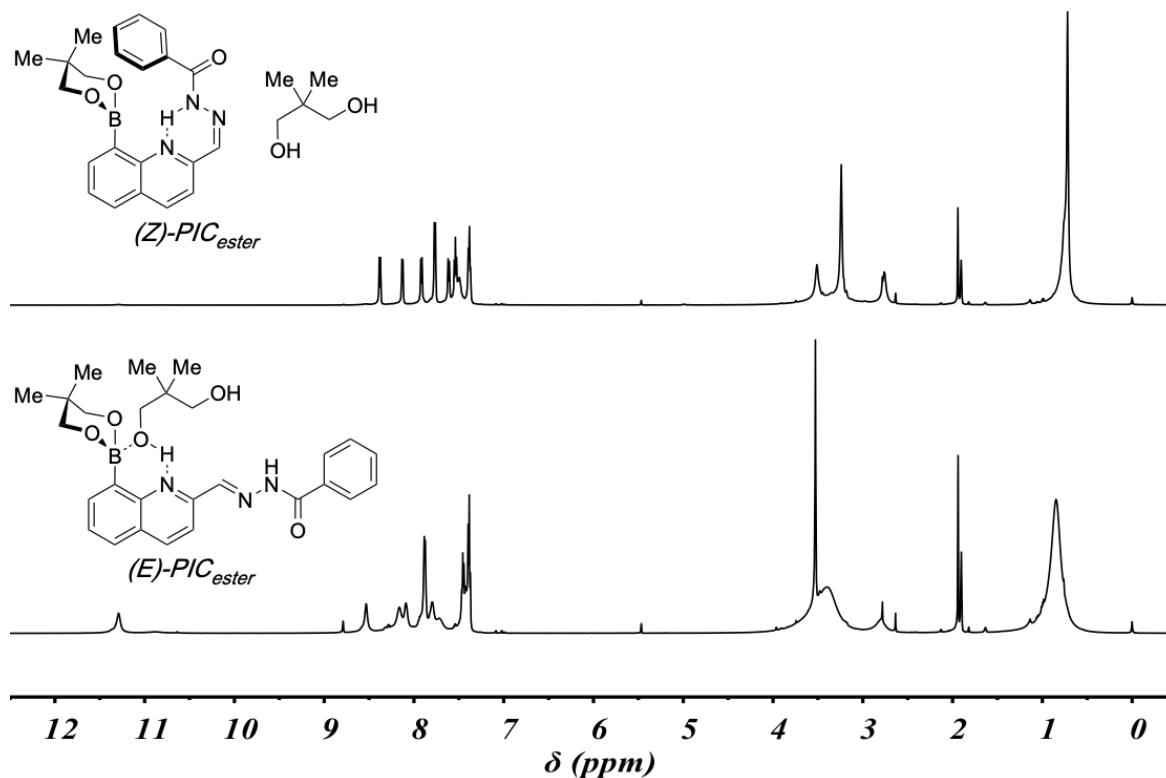


Figure 14. ¹H NMR spectra of (*E*)-PIC_{ester} (bottom) and quantitative conversion to (*Z*)-PIC_{ester} (top) after irradiation with 300 nm light.

Gratifyingly, after condensation with neopentyl glycol in the presence of excess diol (10 equiv), when boronic ester (*E*)-PIC_{ester} is irradiated with 300 nm light, quantitative conversion to (*Z*)-PIC_{ester} is observed (Figure 14). Likewise, in the presence of excess diol, quantitative conversion from (*Z*)-PIC_{ester} to (*E*)-PIC_{ester} is observed. This observation was rationalized by UV-Vis spectroscopy: when (*Z*)-PIC_{acid} is converted to (*Z*)-PIC_{ester}, we observe a 10 nm bathochromic shift in the absorption onset (Figure 15D). In contrast, when comparing (*E*)-PIC_{acid} to (*E*)-PIC_{ester}, no significant spectral changes are observed by UV-Vis (Figure 15C). Consequently, in the

presence of excess diol, the boronic esters possess slightly improved spectral separation between the *E* and *Z* isomers compared to the boronic acids (Figure 15A,B), enabling near-quantitative bidirectional switching.

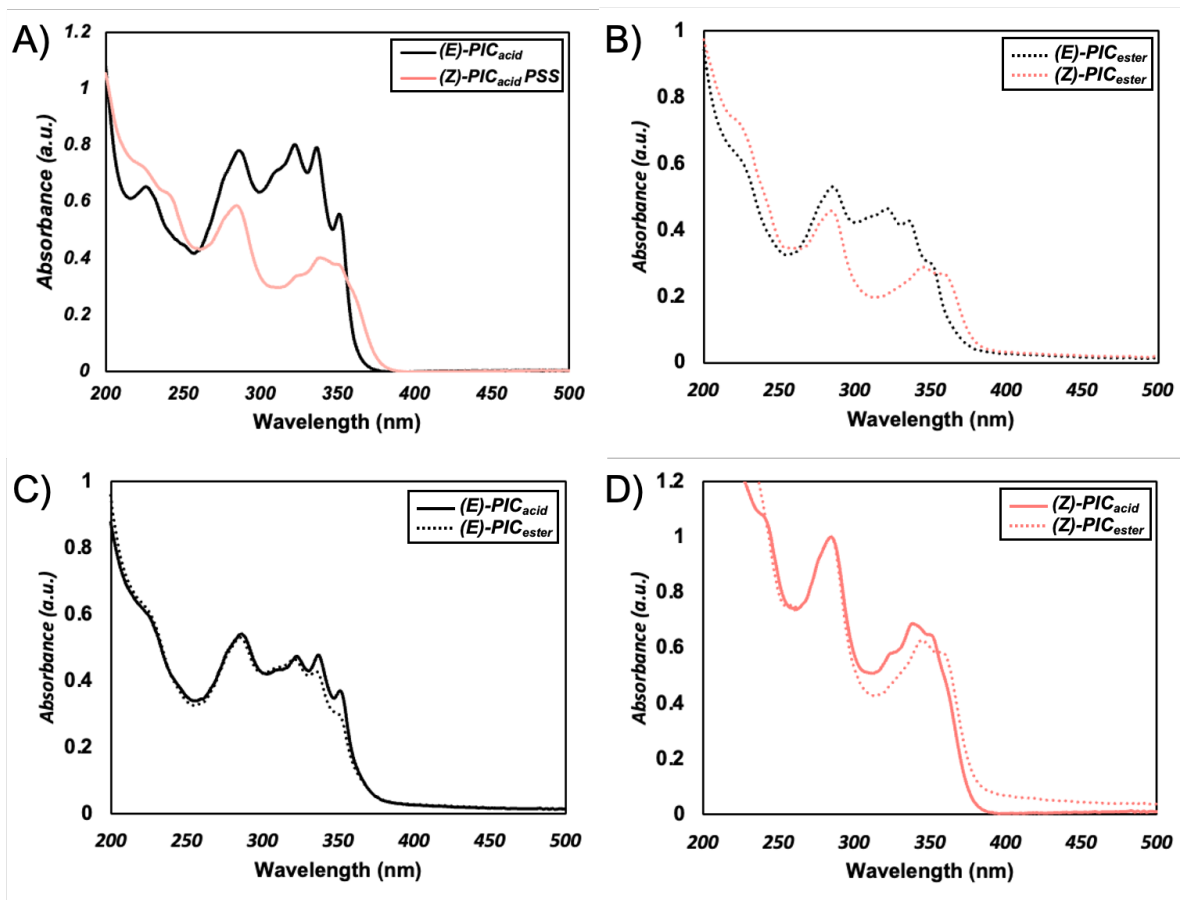


Figure 15. (A) UV-Vis absorption of (*E*)-PIC_{acid} in MeCN (black line, 1.56×10^{-5} M) and (*Z*)-PIC_{acid,PSS} (red line). (B) UV-Vis absorption of (*E*)-PIC_{ester} (black dashed line) and (*Z*)-PIC_{ester} (red dashed line). (C) Comparison of UV-Vis absorption of (*E*)-PIC_{acid} (black line) and addition of 10 equivalents of neopentyl glycol to form (*E*)-PIC_{ester} (black dashed line). (D) Comparison of UV-Vis absorption of (*Z*)-PIC_{acid} (red line) and (*Z*)-PIC_{ester} (red dashed line).

5.1 Photoswitchable Exchange Rates

Facile conversion to boronic esters was achieved in DMF using a 1:2 ratio of boronic acid to diol and removal of DMF *in vacuo*. Because of this simple procedure, we were able to screen a number of boronic esters to find a diol that would exchange at a rate suitable for observing a coalescence temperature by NMR. Ethylene glycol, propylene glycol and neopentyl glycol, and their respective boronic esters from (*E*)-**PIC**_{acid}, were screened. Ethylene glycol exchanged too fast so that no coalescence temperature could be observed. While propylene glycol was slow enough to observe, the NMR was too complex. Neopentyl glycol, on the other hand was found to be the optimal diol for this purpose.

We tested the effect of photoisomerization on the degenerate exchange between neopentyl glycol and the corresponding boronic ester (*E*)-**PIC**_{ester} (1:1, 100 mM). Toluene was used as the solvent, and a small amount of acetone was added to fully dissolve the diol (9:1 toluene-acetone). At 25 °C, ¹H NMR of (*E*)-**PIC**_{ester} shows a broad peak around 1.0 ppm, signifying that the dynamic exchange between diol and ester is occurring faster than the NMR timescale at this temperature (Figure 17). After irradiation with 300 nm light to achieve quantitative conversion to (*Z*)-**PIC**_{ester}, two peaks emerge but are still significantly broadened at room temperature. Upon heating the sample (up to 65 °C), two peaks emerge corresponding to the diol and ester, indicating that

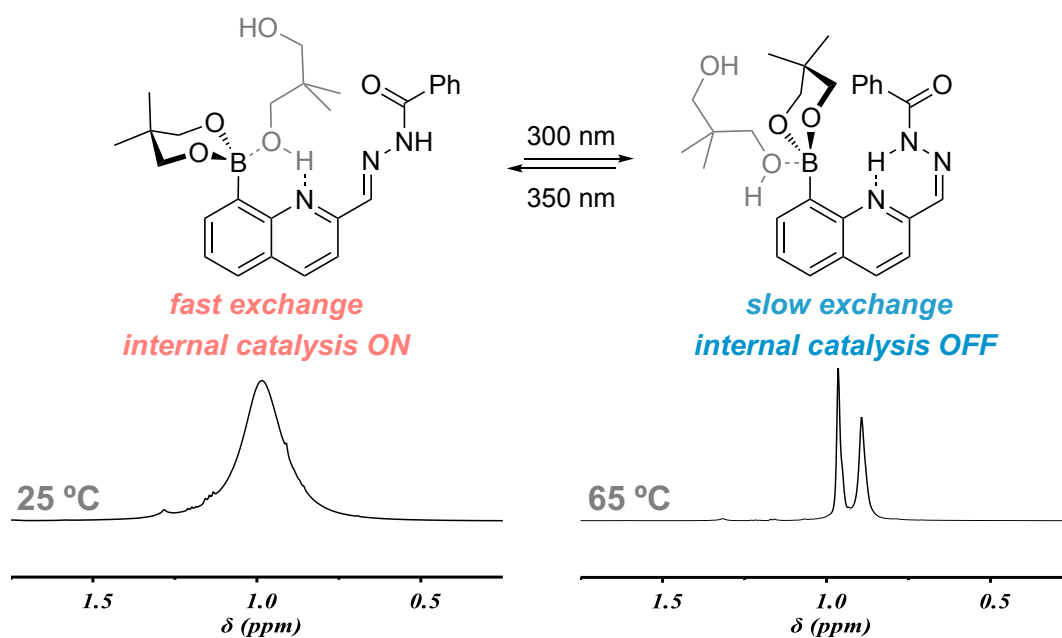


Figure 16. ^1H NMR of the dynamic exchange in (*E*)- $\text{PIC}_{\text{ester}}$ + neo-pentylglycol (25 °C) and static exchange in (*Z*)- $\text{PIC}_{\text{ester}}$ + neo-pentylglycol (65 °C).

exchange does not occur on the NMR timescale in the *Z* isomer, even at elevated temperatures (Figure 16).

The rate of exchange in (*E*)- $\text{PIC}_{\text{ester}}$ could be determined through coalescence between – CH_3 resonances in bound and unbound neopentyl glycol by variable-temperature ^1H NMR (VT-NMR). Upon cooling the mixture, we observe the coalescence temperature of the bimolecular degenerate exchange to be -15 °C (Figure 17). The rate of exchange for (*E*)- $\text{PIC}_{\text{ester}}$ was thus determined to be $4.1 \times 10^3\text{ s}^{-1}$ at 25 °C with an activation energy of 12.4 kcal/mol. A second coalescence temperature is observed at lower temperatures due to a unimolecular fluxional ring flip of the neopentylglycol boronate (Figure 21).⁴²

Fluxionality due to the ring flip is also observed in (*Z*)- $\text{PIC}_{\text{ester}}$, with coalescence occurring around 25 °C (Figure 20). Upon further heating the sample, two peaks emerge as the ring flip

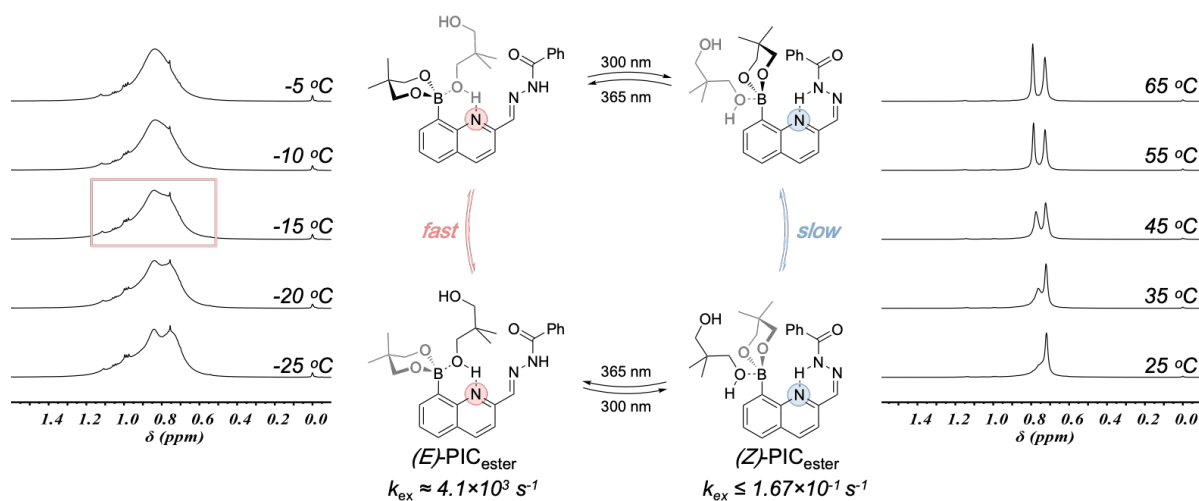


Figure 17. ^1H VT-NMR of the dynamic exchange of (E) -PIC_{ester} (left) and static exchange in (Z) -PIC_{ester} (right).

becomes faster than the NMR timescale. The bimolecular exchange in (Z) -PIC_{ester}, however, was sufficiently slow that a coalescence temperature could not be observed even at elevated temperatures (Figure 17). From this, we can conclude that the exchange is occurring at least as slow as $1.67 \times 10^{-1} \text{ s}^{-1}$ (calculated from $T_c \geq 75^\circ\text{C}$). The exchange was not resolvable by exchange spectroscopy (EXSY) NMR.⁴³

Thus, we have established an upper bound for the exchange rate of (Z) -PIC_{ester} and we can conclude that there are at least 4 orders of magnitude difference between exchange rates in (E) -PIC_{ester} vs. (Z) -PIC_{ester}. The fast bimolecular exchange in (E) -PIC_{ester} suggests that internal catalysis reduces the activation energy for proton transfer. On the other hand, the slower bimolecular exchange in (Z) -PIC_{ester} can be ascribed to the deactivation of internal catalysis through the formation of an intramolecular H-bond, increasing the barrier for proton transfer.

We have demonstrated that photoisomerization of a hydrazone can switch “OFF” internal catalysis of boronic ester exchange. The resulting 10^4 difference in exchange rates is enabled by the formation of an intramolecular H-bond. To show that chemical stimuli cannot regulate internal catalysis to the same extent, we synthesized control (2-methylquinolin-8-yl)boronic acid (**Me-QBA**, **Error! Reference source not found.**). VT-NMR revealed that the corresponding neopentyl glycol boronate, Me-QBE undergoes exchange roughly 10 times faster than to (*E*)-**PIC_{ester}** ($4.9 \times 10^4 \text{ s}^{-1}$ at 25 °C, Figure 15). We hypothesize that exchange in (*E*)-**PIC_{ester}** is slower than that of Me-QBE due to the presence of the electron-withdrawing hydrazone, which reduces the basicity of the quinoline, and contributes some degree of steric hindrance. When **Me-QBE** is exposed to 1.0 equivalent of trifluoroacetic acid (TFA), an acid capable of fully protonating the quinoline, only a moderate decrease in exchange rates was observed ($3.0 \times 10^4 \text{ s}^{-1}$, Figure 18). This observation is consistent with the fact that diol addition to boronic acids can be both acid and base catalyzed,^{44,45} so external proton sources cannot deactivate internal catalysis. These experiments further highlight the importance the intramolecular H-bond in our design to deactivate internal catalysis. Additionally, Letsinger has shown that the presence of exogenous quinoline does not increase the transesterification rate for phenylboronic ester, indicating that internal catalysis is crucial for accelerating exchange.⁴⁶

The quinoline internal catalyst is crucial to our design of PIC. The rigid aromatic structure serves two functions: (1) internal catalysis; (2) formation of an intramolecular H-bond with the acyl hydrazone photoswitch. In addition to showing that an internal proton source is necessary to turn off internal catalysis, we wanted to demonstrate that the quinoline nitrogen is indeed involved in internal catalysis. Single crystals were grown in methanol from the esterification of **Me-QBA-OMe** with catechol (as a non-exchangeable diol). The crystal structure shows that the methanol

proton is dissociated and the quinoline nitrogen is protonated (Scheme 11). By using a non-exchangeable diol such as catechol we are able to isolate an intermediate in the mechanism, thus showing that the quinoline nitrogen is indeed involved in proton transfer.

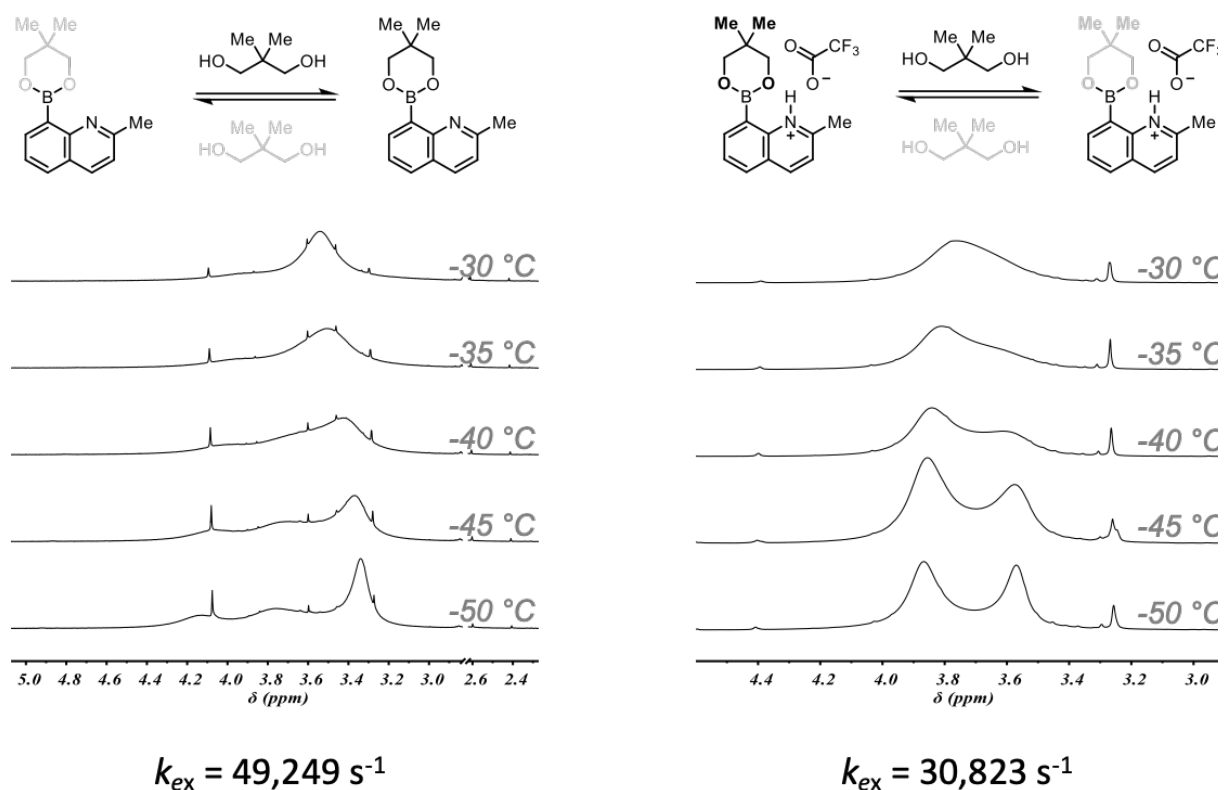
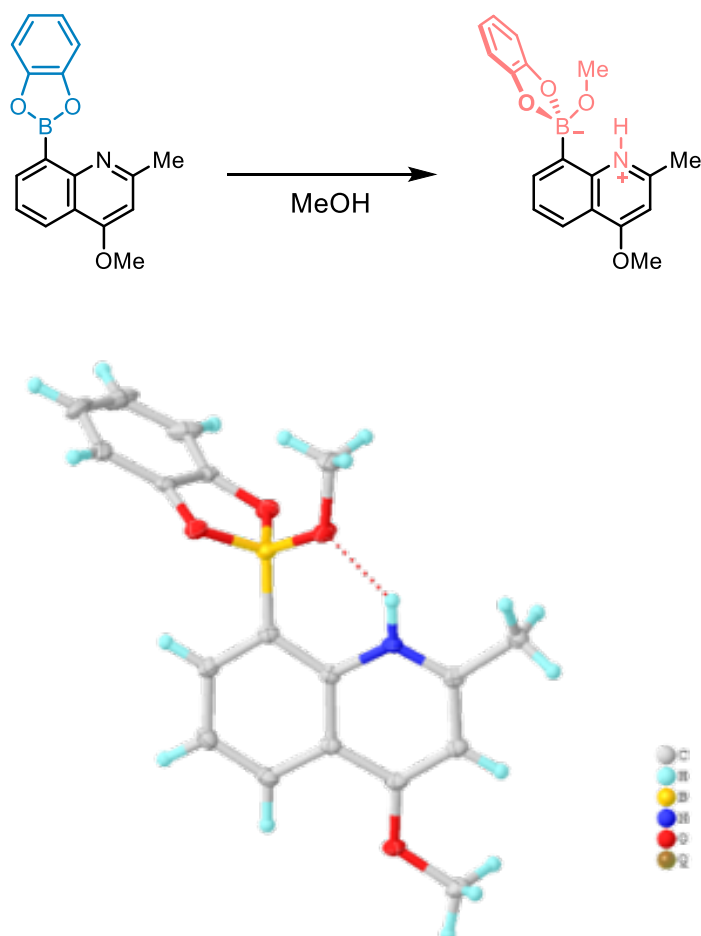


Figure 18. ^1H VT-NMR of the dynamic exchange of Me-QBE (left) and Me-QBE + TFA (right).

We have demonstrated the use of a bidirectional hydrazone photoswitch to control the rate of exchange between a boronate ester and the corresponding diol by at least 4 orders of magnitude. The dramatic change in rates afforded by reversible deactivation of internal catalysis lays the foundation for photocontrolling kinetics in different dynamic covalent reactions. The ability to remotely and reversibly control a dynamic covalent exchange rate can be translated to turn on and

off assembly and reconfiguration in smart materials. The application of these photoswitchable dynamic bonds to tune viscoelasticity in polymer networks is ongoing in our laboratory.



Scheme 14. Crystal structure of Me-QBA-OMe and catechol in methanol

5.2 VT-NMR Kinetic Experiment Procedures

Coalescence experiment for (*E*)-PIC_{ester} with neopentyl glycol: The following experiment was adapted from reference 18 with some modifications: (*E*)-PIC_{acid} (31.9 mg, 0.1 mmol) and 2.0 equivalents of neopentyl glycol (20.8 mg, 0.2 mmol) were dissolved in DMF (1 mL). The mixture was stirred for 1 hour before removing the DMF under reduced pressure on a rotovap at 60 °C.

The resulting mixture was dissolved in toluene-d₈ and acetone-d₆ (0.1 M, 9:1 toluene:acetone). After allowing the reaction to reach equilibrium for 30 min., ¹H NMR spectra of the mixture was taken at temperatures ranging from 25 °C to -50 °C. The spectra were investigated for the coalescence of the methyl peaks of neopentyl glycol in both the esterified and free forms. The peaks in question coalesced at -15 °C.

The activation energy for exchange was calculated using the equation:

$$\Delta G^\ddagger = RT_c [22.96 + \ln\left(\frac{T_c}{\Delta\nu}\right)]$$

where $R = 1.9872 \cdot 10^{-3}$ kcal/mol K is the universal gas constant, T_c is the coalescence temperature, and $\Delta\nu$ is the separation in Hz of the bound and unbound resonances. In this particular calculation, the methyl resonance of bound and unbound neopentyl glycol were monitored for coalescence, which was found to be -15 °C (258.15 K), and $\Delta\nu$ was found to be 72.0 Hz (determined by taking the ¹H NMR spectrum of the mixture far below coalescence (-50 °C) and measuring the separation of the resonances in question). The ΔG^\ddagger value thus calculated was 12.4 kcal/mol.

Furthermore, the rate at coalescence temperature is:

$$k_{ex} = \frac{\pi}{\sqrt{2}}(\Delta\nu)$$

Which calculates to $k_{ex} = 160 \text{ s}^{-1}$ at coalescence temperature (258.15 K). Finally, using the activation energy just calculated along with the Arrhenius equation,

$$k = A \cdot \exp\left(-\frac{\Delta G^\ddagger}{RT}\right)$$

The rate of the reaction at room temperature can be calculated:

$$\frac{k_{T_2}}{k_{T_1}} = \exp\left(-\frac{\Delta G^\ddagger}{R}\left(\frac{1}{T_2} - \frac{1}{T_1}\right)\right)$$

Using $T_1 = 258.15$ K (coalescence temperature), $T_2 = 298.15$ K (room temperature), $\Delta G^\ddagger = 12.4$ kcal/mol, and $k_{T_1} = 160$ s⁻¹, the rate at room temperature (k_{T_2}) was calculated to be $k = 4100$ s⁻¹.

The upper-bound exchange rate for (Z)-PIC_{ester} was determined analogously, assuming that exchange occurs above 75 °C (348.15 K), and Δv was x.

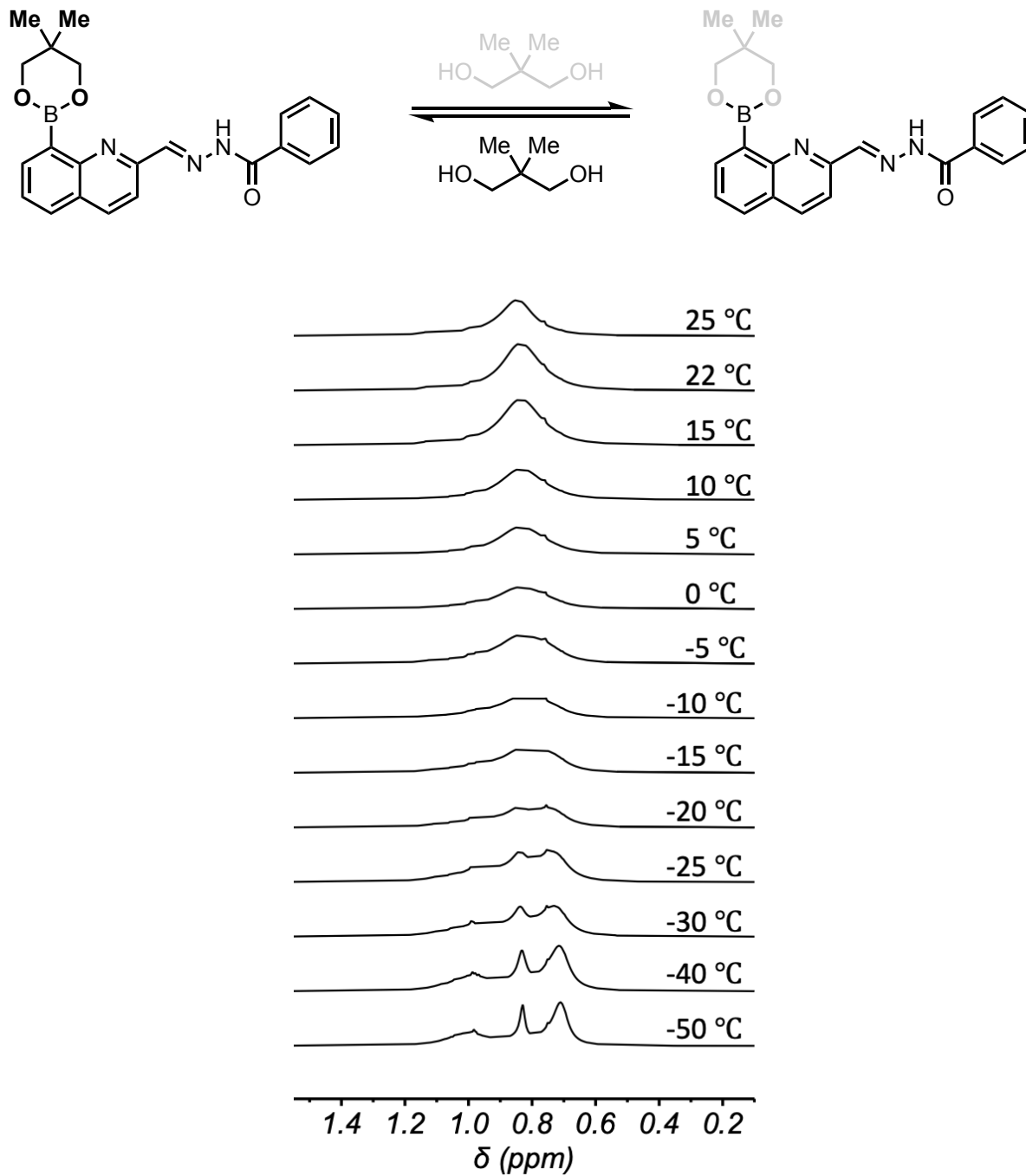


Figure 19. VT-NMR kinetic study boronic ester transesterification of *(E)*-PIC_{ester} and neopentyl glycol. Coalescence for *(E)*-PIC_{ester} at -15 °C ($\Delta\nu = 72.0$ Hz) provides $k \sim 4100$ s⁻¹ at 25 °C.

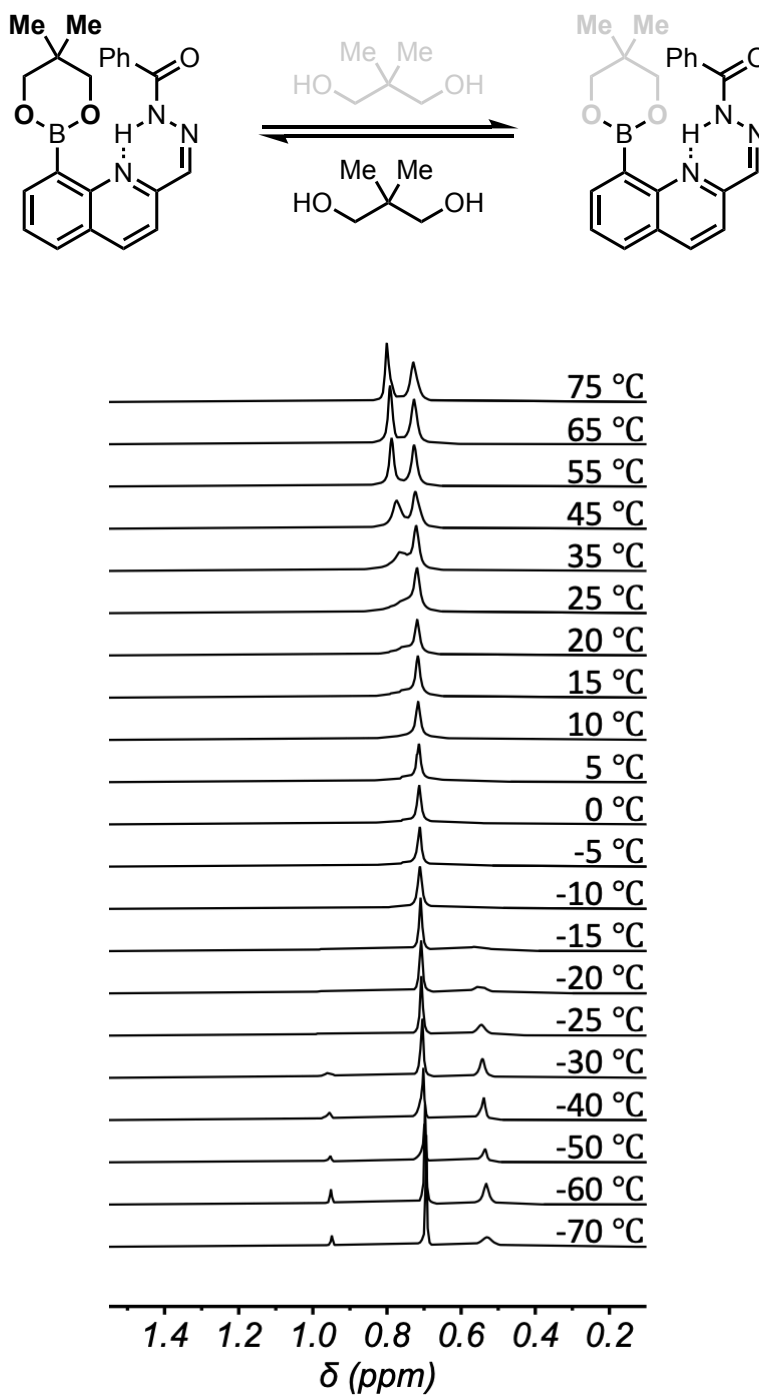


Figure 20. VT-NMR kinetic study boronic ester transesterification of **(Z)-PIC_{ester}** and neopentyl glycol. Coalescence for **(Z)-PIC_{ester}** is not observed up to 75 °C. Coalescence at 25 °C represents the chair flip (activation energy = 13.7 kcal/mol).

5.3 PIC in a polymer network

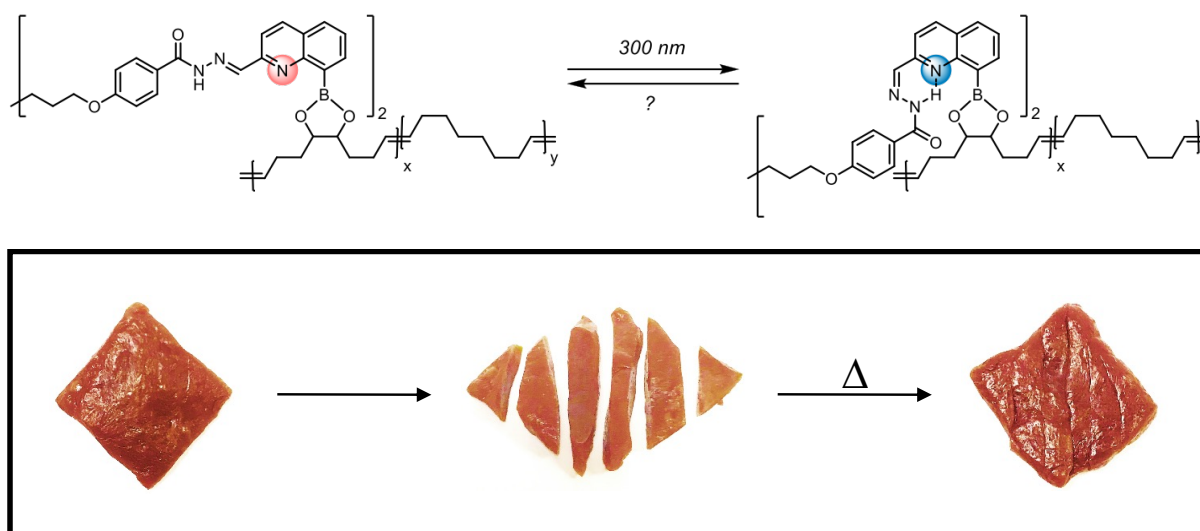


Figure 21. *(E)*-PIC_{crosslinker} in a polymer network.

The application of PIC into a polymer network could be advantageous towards the development of new smart materials controlled by light. To demonstrate this concept, *(E)*-PIC_{ester} was turned into crosslinker *(E)*-PIC_{crosslinker} by condensation of a bis-hydrazide with **5**. A diol polymer was prepared by ring-opening metathesis polymerization of cyclooctadiene monoxide, followed by acidic hydrolysis of the epoxide. This polymer was crosslinked with *(E)*-PIC_{crosslinker} in toluene in a 10:1 ratio (w/w), followed by solvent evaporation. Initial experiments showed that the polymer network with *(E)*-PIC_{crosslinker} was able to undergo self-healing after being cut (Figure 21). Upon irradiation with 300 nm light, after being cut, the material is no longer able to undergo self-healing. Unfortunately, when irradiated with 350 nm light the material does not become self-healing again. From these experiments, it is unclear whether initial irradiation with 300 nm light is causing the photoswitch to isomerize or due to reactivity of the double bonds within the polymer

network. Future experiments to demonstrate photoswitchable self-healing should be designed around a material that is less optically dense and without photosensitive functional groups.

References

1. Winne, J. M.; Leibler, L.; Du Prez, F. E. Dynamic covalent chemistry in polymer networks: a mechanistic perspective. *Polym. Chem.* **2019**, *10*, 6091–6108.
2. Wojtecki, R. J.; Meador, M. A.; Rowan, S. J. Using the dynamic bond to access macroscopically responsive structurally dynamic polymers. *Nat. Mater.* **2011**, *10*, 14–27.
3. Boehnke, N.; Cam, C.; Bat, E.; Segura, T.; Maynard, H. D. Imine Hydrogels with Tunable Degradability for Tissue Engineering. *Biomacromolecules* **2015**, *16*, 2101–2108.
4. Lohse, M. S.; Bein, T. Covalent Organic Frameworks: Structures, Synthesis, and Applications. *Adv. Funct. Mater.* **2018**, *28*, 1705553.
5. Liu, Y.; Lehn, J. M.; Hirsch, A. K. H. Molecular Biodynamers: Dynamic Covalent Analogues of Biopolymers. *Acc. Chem. Res.* **2017**, *50*, 376–386.
6. Rottger, M.; Domenech, T.; van der Weegen, R.; Breuillac, A.; Nicolay, R.; Leibler, L. High-performance vitrimers from commodity thermoplastics through dioxaborolane metathesis. *Science* **2017**, *356*, 62–65.
7. Gu, R. R.; Flidrova, K.; Lehn, J. M. Dynamic Covalent Metathesis in the C = C/C = N Exchange between Knoevenagel Compounds and Imines. *J. Am. Chem. Soc.* **2018**, *140*, 5560–5568.
8. Delahaye, M.; Winne, J. M.; Du Prez, F. E. Internal Catalysis in Covalent Adaptable Networks: Phthalate Monoester Transesterification As a Versatile Dynamic Cross-Linking Chemistry. *J. Am. Chem. Soc.* **2019** *141*, 15277–15287.
9. Rekondo, A.; Martin, R.; Ruiz de Luzuriaga, A.; Cabanero, G.; Grande, H. J.; Odriozola, I. Catalyst-free room-temperature self-healing elastomers based on aromatic disulfide metathesis. *Mater. Horiz.*, **2014**, *1*, 237–240

10. Chen, X.; Dam, M. A.; Ono, K.; Mal, A.; Shen, H.; Nutt, S. R.; Sheran, K.; Wudl, F. A thermally re-mendable cross-linked polymeric material. *Science*, **2002**, 295, 1698–1702
11. Podgoński, M.; Fairbanks, B. D.; Kirkpatrick, B. E.; McBride, M.; Martinez, A.; Dobson, A.; Bongiardina, N. J.; Bowman, C. N. Toward Stimuli-Responsive Dynamic Thermosets through Continuous Development and Improvements in Covalent Adaptable Networks (CANs). *Adv. Mater.*, **2020**, 32, 1906876.
12. Self, J. L.; Dolinski, N. D.; Zayas, M. S.; Read de Alaniz, J.; Bates, C. M. Brønsted-Acid-Catalyzed Exchange in Polyester Dynamic Covalent Networks. *ACS Macro Lett.*, **2018**, 7, 817–821.
13. Colodny, P. C.; Tobolsky, A. V. Chemorheological Study of Polyurethan Elastomers. *J. Am. Chem. Soc.*, **1957**, 79, 4320–4323.
14. Lu, Y.-X.; Tournilhac, F.; Leibler, L.; Guan, Z. Making Insoluble Polymer Networks Malleable via Olefin Metathesis *J. Am. Chem. Soc.*, **2012**, 134, 8424–8427.
15. Altuna, F. I.; Pettarin, V.; Williams, R. J. J. Self-healable polymer networks based on the cross-linking of epoxidised soybean oil by an aqueous citric acid solution *Green Chem.*, **2013**, 15, 3360–3366.
16. Capon, B. Neighbouring group participation *Q. Rev., Chem. Soc.*, **1964**, 18, 45–111.
17. Wulff, G.; Lauer, M.; and Bohnke, H. Rapid Proton Transfer as Cause of an Unusually Large Neighboring Group Effect. *Angew. Chem. Int. Ed.* **1984**, 23, 741-742.
18. Cromwell, O. R.; Chung, J.; Guan, Z. Malleable and Self-Healing Covalent Polymer Networks through Tunable Dynamic Boronic Ester Bonds. *J. Am. Chem. Soc.* **2015**, 137, 6492–6495.

19. Nishimura, Y.; Chung, J.; Muradyan, H.; Guan, Z. Silyl Ether as a Robust and Thermally Stable Dynamic Covalent Motif for Malleable Polymer Design. *J. Am. Chem. Soc.* **2017**, 139, 14881–14884.
20. Neilson, B. M.; Bielawski, C. W. Illuminating photoswitchable catalysis. *ACS Cat.* **2013**, 3, 1874–1885.
21. Boelke, J.; Hecht, S. Designing Molecular Photoswitches for Soft Materials Applications. *Adv. Optical Mater.* **2019**, 7, 1-14.
22. Fischer, E.; Hirschberg, Y. Photochromism and reversible multiple internal transitions in some spiropyrans at low temperatures. Part I. *J. Chem. Soc.* **1954**, 11, 4522.
23. Irie, M.; Fukaminato, T.; Matsuda, K.; Kobatake, S. Photochromism of Diarylethene Molecules and Crystals: Memories, Switches, and Actuators. *Chem. Rev.* **2014**, 114, 12174-12277.
24. Bandara, H. M. D.; Burdette, S. C. Photoisomerization in different classes of azobenzene. *Chem. Soc. Rev.* **2012**, 41, 1809-1825.
25. a) Lehn, J.-M. Chem. - Conjecture: Imines as Unidirectional Photodriven Molecular Motors—Motional and Constitutional Dynamic Devices. *Chem. Eur. J.* **2006**, 12, 5910-5915; b) Chaur, M. N.; Collado, D.; Lehn, J.-M. Configurational and Constitutional Information Storage: Multiple Dynamics in Systems Based on Pyridyl and Acyl Hydrazones *Chem. Eur. J.* **2011**, 17, 248-258; c) Vantomme, G.; Hafezi, N.; Lehn, J.-M. A light-induced reversible phase separation and its coupling to a dynamic library of imines. *Chem. Sci.* **2014**, 5, 1475-1483; d) Vantomme, G.; Jiang, S.; Lehn, J.-M. Adaptation in Constitutional Dynamic Libraries and Networks, Switching between Orthogonal Metalloselection and Photoselection Processes. *J. Am. Chem. Soc.* **2014**, 136, 9509-9518.

26. a) Ray, D.; Foy, J. T.; Hughes, R. P.; Aprahamian, I. A switching cascade of hydrazone-based rotary switches through coordination-coupled proton relays. *Nat. Chem.* **2012**, *4*, 757-762; b) Qian, H.; Aprahamian, I. An emissive and pH switchable hydrazone-based hydrogel *Chem. Commun.* **2015**, *51*, 11158-11161; c) Qian, H.; Pramanik, S.; Aprahamian, I. Photochromic Hydrazone Switches with Extremely Long Thermal Half-Lives *J. Am. Chem. Soc.* **2017**, *139*, 9140-9143; d) I. Aprahamian, Hydrazone switches and things in between. *Chem. Commun.* **2017**, *53*, 6674-6684.
27. Van Dijken, D. J.; Kovaříček, P.; Ihrig, S. P.; Hecht, S. Acylhydrazones as Widely Tunable Photoswitches. *J. Am. Chem. Soc.* **2015**, *137*, 14982–14991.
28. Kathan, M.; Hecht, S. Photoswitchable molecules as key ingredients to drive systems away from the global thermodynamic minimum. *Chem. Soc. Rev.*, **2017**, *46*, 5536-5550.
29. Goulet-Hanssens, A.; Eisenreich, F.; Hecht, S. Enlightening Materials with Photoswitches. *Adv. Mater.* **2020**, *32*, 1-23.
30. Kathan, M.; Kovaříček, P.; Jurissek, C.; Senf, A.; Dallmann, A.; Thünemann, A. F.; Hecht, S. Control of Imine Exchange Kinetics with Photoswitches to Modulate Self-Healing in Polysiloxane Networks by Light Illumination. *Angew. Chemie Int. Ed.* **2016**, *55*, 13882–13886.
31. Lemieux, V.; Gauthier, S.; Branda, N. R. Selective and Sequential Photorelease Using Molecular Switches. *Angew. Chemie*, **2006**, *118*, 6974–6978.
32. Wilson, D.; Branda, N. R. Turning “on” and “off” a pyridoxal 5'-phosphate mimic using light. *Angew. Chem. Inter. Ed.* **2012**, *51*, 5431–5434.
33. Kathan, M.; Kovaříček, P.; Jurissek, C.; Senf, A.; Dallmann, A.; Thünemann, A. F.; Hecht, S. Control of Imine Exchange Kinetics with Photoswitches to Modulate Self-Healing in Polysiloxane Networks by Light Illumination. *Angew. Chem. Int. Ed.*, **2016**, *55*, 13882–13886.

34. Gillis, E. P.; Burke, M.D. Multistep Synthesis of Complex Boronic Acids from Simple MIDA Boronates. *J. Am. Chem. Soc.* **2008**, 130, 14084–14085.
35. Doebner, O.; Miller, W. V. Ueber eine dem Chinolin homologe Base. *Ber.*, **1883**, 14, 2464-2472
36. Matsugi, M.; Tabusa, F.; Minamikawa, J. I. Doebner-miller synthesis in a two-phase system: Practical preparation of quinolines. *Tet. Lett.*, **2000**, 41, 8523–8525.
37. Leir, C. M. An improvement in the Doebner-Miller synthesis of quinaldines. *J. Org. Chem.* **1977**, 42, 911–913.
38. Kaplan, H. The Use of Selenium Dioxide in the Preparation of Quinoline Aldehydes. *J. Am. Chem. Soc.* **1941**, 63, 2654–2655.
39. Zhang, Y.; Gao, J.; Li, W.; Lee, H.; Lu, B. Z.; Senanayake, C. H. Synthesis of 8-arylquinolines via one-pot Pd-catalyzed borylation of quinoline-8-yl halides and subsequent Suzuki-Miyaura coupling. *J. Org. Chem.* **2011**, 76, 6394–6400.
40. Hobson, S. T.; Boecker, J. D.; Gifford, J. H.; Nohe, T. L.; Wierks, C. H. . Synthesis and unusual stability of pyridine and N-methyl pyridinium 1,3-dioxolanes. *J. Het. Chem.*, **2003**, 40, 277–282.
41. Son, J. H.; Tamang, S. R.; Yarbrough, J. C.; Hoefelmeyer, J. D. Hydrolysis of 8-(pinacolboranyl)quinoline: Where is the 8-quinolyboronic acid? *Zeitschrift Fur Naturforschung - Section B Journal of Chemical Sciences* **2015**, 70, 775–781.
42. Eichhorn, A. Copper(I) catalyzed borylation and cross-coupling reactions; (Figure 45, page 99) PhD Thesis, Julius Maximilian University of Würzburg: Würzburg, Germany, **2018**.
43. Kleckner, I. R.; & Foster, M. P. (2011). An introduction to NMR-based approaches for measuring protein dynamics. *Biochimica et Biophysica Acta* **2011**, 1814, 942–968.

44. Collins, B. E.; Metola, P.; Anslyn, E. V. On the rate of boronate ester formation in ortho-aminomethyl-functionalised phenyl boronic acids. *Supramol. Chem.* **2013**, *25*, 79–86.
45. Sun, X.; Chapin, B. M.; Metola, P.; Collins, B.; Wang, B.; James, T. D.; Anslyn, E. V. The mechanisms of boronate ester formation and fluorescent turn-on in ortho-aminomethylphenylboronic acids. *Nat. Chem.* **2019**, *11*, 768–778.
46. Letsinger, R. L.; Dandegaonke, S. H. Organoboron Compounds. IX. 8-Quinolineboronic Acid, its Preparation and Influence on Reactions of Chlorohydrins, *J. Am. Chem. Soc.* **1958**, *81*, 498–501.
47. Morrison J. D.; Letsinger, R. Organoboron Compounds. XVIII. Bifunctional Binding of Water by the cis-1,2-Cyclopentanediol Ester of 8-Quinolineboronic Acid L. *J. Org. Chem.* **1964**, *29*, 11, 3405–3407
48. Goldman, M.; Wehry, E. L. Environmental effects upon the photoluminescence of 8-quinolineboronic acid *Anal. Chem.* **1970**, *42*, 11, 1186–1188.

Appendix A. Original Research Proposal

A.1 Abstract

The development of super-resolution microscopy has led to numerous biological discoveries on the nanometer scale, surpassing the diffraction limit of light. The expansion of single molecule localization microscopy (SLM) has led to more accurate methods to image individual molecules. This technology has yet to be applied to image individual ions. Here, we propose a new tool to image single ions through the combination of spontaneous blinking fluorophores, metal ion sensors, and FRET. This simple strategy can be applied to image biological Zn(II) ions to better understand their function and role in pathological diseases such as diabetes and Alzheimer's.

A.2 Background and Significance

A.2.1 Super-resolution Microscopy

Surpassing the diffraction limit of light is a significant accomplishment which has enabled the discovery of worlds previously unexplored under the microscope. This effort was recognized with the 2014 Nobel Prize in Chemistry, awarded jointly to Eric Betzig, Stefan W. Hell, and William E. Moerner for their groundbreaking contributions in super-resolution microscopy. Moerner's work in Single-molecule Localization Microscopy (SLM) has led to several progeny techniques, including photoactivated localization microscopy (PALM)³, fluorescence photoactivation localization microscopy (FPALM)⁴, stochastic optical reconstruction microscopy (STORM)⁵, ground-state depletion microscopy followed by individual molecular return (GSDIM)⁶, and direct STORM (dSTORM).⁷

A key attribute of all SLM methods is that, during data acquisition, only a small subset of fluorophores are switched on, detected and localized at any given time. These fluorophores are then switched off or bleached, and another subset is switched on. Repetition of this process allows a super-resolution image to be constructed from a large number of individual molecular localizations. Fluorescence Resonance Energy Transfer (FRET) microscopy is another imaging technique which utilizes a donor/acceptor pair of fluorophores for proximity dependent imaging. Both techniques have been applied extensively in cellular imaging and have provided important insight to biological systems.

Up until this point, there have been no reports in literature that successfully merge these two imaging techniques. It has been proposed by Verveer and Grecco that coupling super-resolution and FRET microscopy is possible, however has not been demonstrated because of the challenge to switch donor and acceptor fluorophores in a single pair simultaneously to allow FRET to occur.⁸ Tinnefeld separately adds to this dialogue, predicting that merging super-resolution and FRET would be fruitful for the design and investigation of artificial machines, nanomaterials, and bioanalytical tools.⁹

Developing a technique for super-resolution FRET microscopy will need to be addressed by organic chemists to produce the appropriate donor/acceptor pair. In doing so we must first ask: What are the challenges associated with switching donor and acceptor fluorophores in a single pair simultaneously to allow FRET to occur? The challenge lies in the blinking mechanism. Current STORM dyes require external additives (usually a reducing reagent) to induce blinking cycles. In addition to interfering with the local environment, the complications involved with donor acceptor pairs makes FRET a daunting task.

A.2.2 Imaging Biological Zinc

Zn(II), the second most abundant d-block metal ion in the human brain and is involved in virtually every biological process. Zinc plays important roles in many biological processes, including regulation of apoptosis, signal transmission, enzyme function, and gene expression and is associated in a number of pathological processes, such as diabetes and Alzheimer's disease. Zn(II) pools have been implicated in both neurophysiology and disease, but details of its functional significance remain unclear. Is Zn(II) a neurotransmitter? What factors govern Zn(II) release into the synapse in physiological and pathological contexts? How and why does Zn(II) influence signaling cascades and synaptic plasticity? These questions remain unanswered despite chemist's and biologist's best efforts to study Zinc's precise role. Because Zn(II) spectroscopically invisible, chemists have developed fluorescent zinc sensors to visualize/quantify free zinc in cells. Despite this, there has yet to be a way to image Zinc (or any other biological ion) through super-resolution microscopy. The ability to resolve individual Zinc ions on the nm scale could provide a clearer picture for understanding Zinc's biological function.

A.3 Specific Aims

General: to develop a technique for FRET based super-resolution imaging of metal ions in live cells.

Specific Aim: synthesize and study the photophysical properties between proposed donor fluorophore and a spontaneous blinking reporter fluorophore.

A.4 Previous Work

A.4.1 Spontaneous Blinking Fluorophores

Current *d*STORM (direct STORM) dyes rely on light or external additives (usually a reducing reagent) to induce blinking cycles. In addition to interfering with the local environment, this complicates imaging live cells. The Urano group circumvented this problem by designing a dye that would be in equilibrium between a nonfluorescent and fluorescent form and therefore blink spontaneously (Figure 21).¹⁰ They found that hydroxymethyl rhodamines were an excellent scaffold and devised methods to tune the equilibrium constant of intramolecular spirocyclization. The transient lifetime of the “open” fluorescent form (50–150 ms) allows for high-quality SMLM with excellent photon yields (~2600) even under substantially reduced illumination intensities.

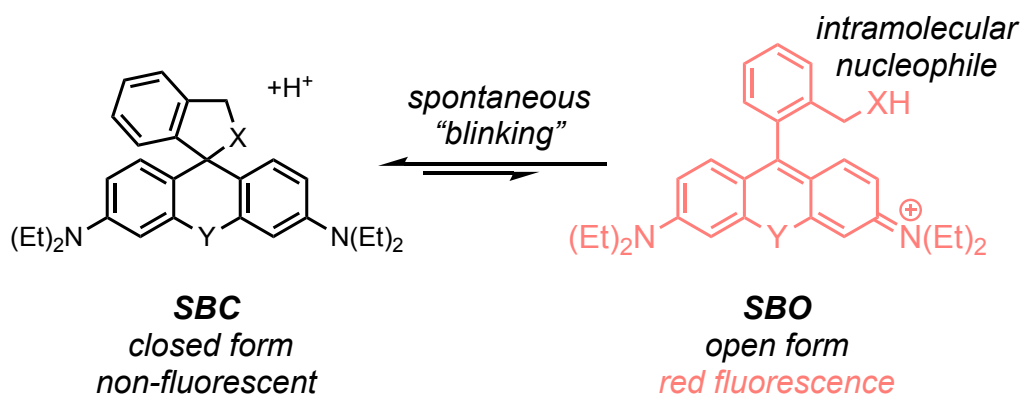


Figure 22. Mechanism of spontaneous blinking rhodamine dyes.

A.4.2 Zinc Sensors

As stated earlier, chemists have developed a large library of fluorescent Zinc sensors to visualize and quantify free Zn(II) ions in cells because it is spectroscopically invisible. BIPY binds to Zinc through a unique mechanism and has a nanomolar binding affinity. In its unbound state,

BIPY displays blue fluorescence, however, upon binding to zinc, **BIPY-Zn** becomes rigid, and conjugation is extended and thus a large bathochromic shift in the emission is observed (Figure 22).¹¹ The green emission of bound BIPY overlaps well with the absorption of the open ring rhodamine and have been demonstrated to be a compatible FRET pair.

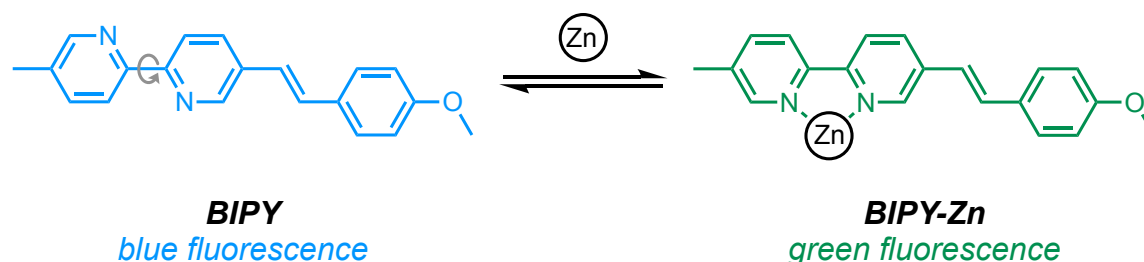


Figure 23. Mechanism of Zinc binding induced bathochromic shift in BIPY fluorophores.

A.5 Proposed Research

Dyes that undergo spontaneous blinking offer a unique opportunity to address the appropriate donor/acceptor pair for super-resolution FRET. Using a non-switchable acceptor with spontaneous blinking properties and a switchable donor with a metal coordination site, super-resolution FRET imaging of metal ions can be achieved. The excited **BIPY-SPC** (blue) undergoes a large Stokes shift upon metal coordination to form **BIPY-Zn-SPC** (green) (Figure 23). The shifted emission then overlaps with the absorption of open ring form of rhodamine (red) in **BIPY-Zn-SPO** and FRET results in another large Stokes shift (Figure 23). Since only a small population of the rhodamine is in the open form under physiological conditions, single molecules can be efficiently imaged through FRET to provide super-resolved images of metal ions in a cell. The background fluorescence from BIPY can be eliminated with a short wavelength filter and/or a long wavelength filter to isolate the emission signal from the reporter.

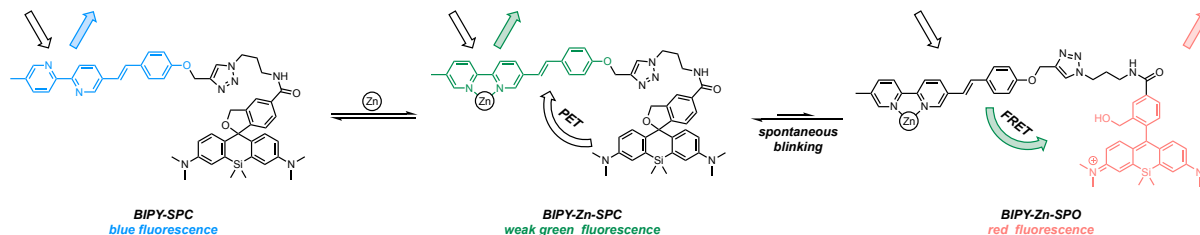


Figure 24. Proposed mechanism for super-resolution imaging of Zinc ions by the combination of a FRET pair consisting of a spontaneous blinking (acceptor) and a Zinc sensor (donor).

Figure 25. Proposed mechanism for super-resolution imaging of Zinc ions by the combination of a FRET pair consisting of a spontaneous blinking (acceptor) and a Zinc sensor

A.5.1 Experimental Plan

The synthesis of the BIPY-alkyne and Rhodamine-azide have both been reported in good yields and would make up a total of 6 steps.¹¹ Using “click” chemistry the pair can be linked in the final synthetic step to afford **BIPY-SPC** (Figure 24). Following the synthesis of the proposed ligand, fluorescence titrations with zinc can be used to assess the blinking properties and determine the optimal excitation wavelengths. After which, confocal imaging of the free ligand should show the BIPY emission and no signal using STORM. Upon addition of zinc to the cells, confocal imaging should show a shifted emission of the **BIPY-Zn-SPC** whereas STORM imaging should detect the FRET signal from the blinking **BIPY-Zn-SPO** (Figure 23).

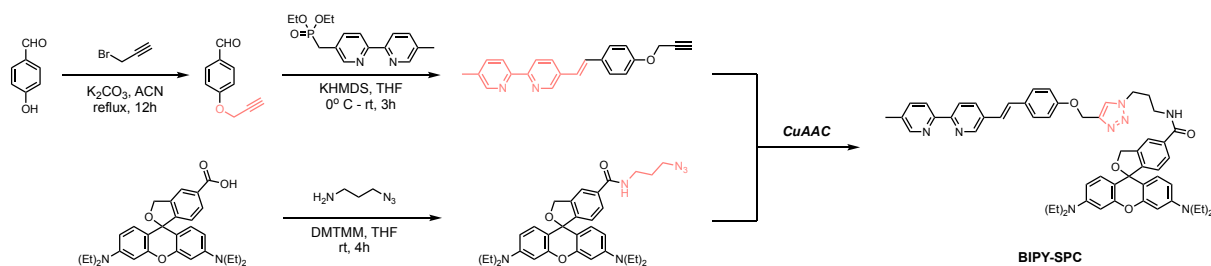


Figure 25. Synthesis of BIPY-SPC.

A.5.2 Experimental Challenges and Contingency Plans

If the proposed structure does not behave as intended, we need to look at other potential donors. Using non-switchable acceptor with spontaneous blinking properties and a non-switchable donor, we will determine the efficiency of FRET through the absorption and emission spectra. By employing “click” chemistry, a variety of donor fluorophores can be used so the optimal photophysical properties can be explored.

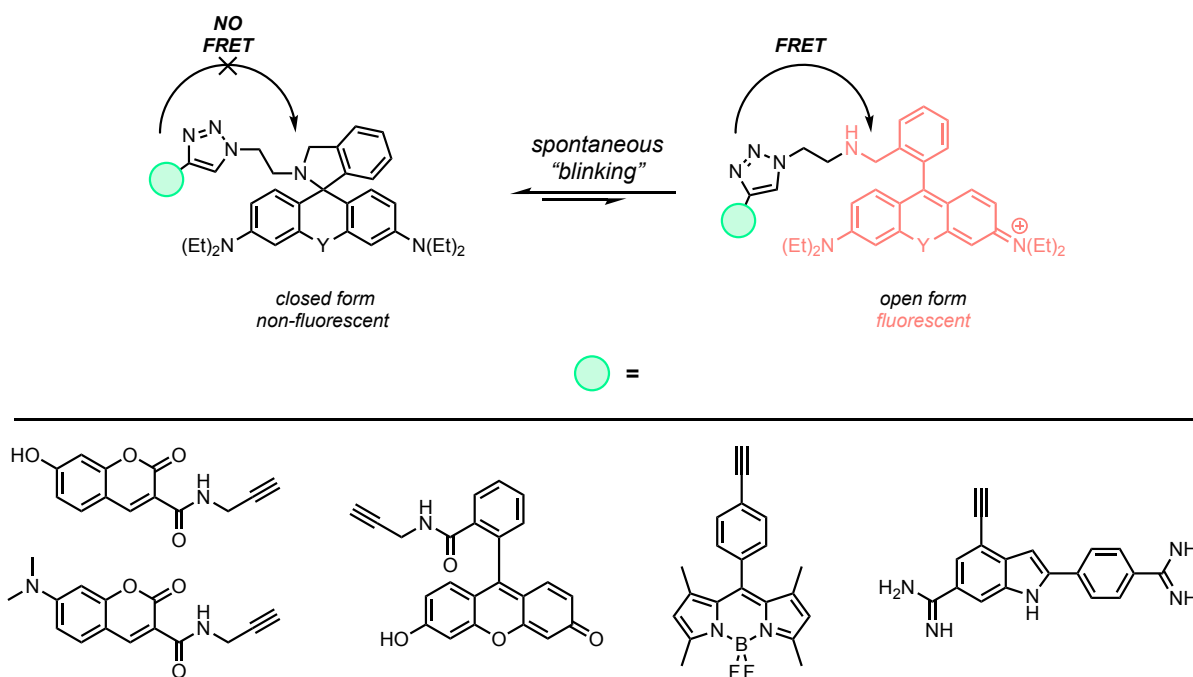


Figure 26. Utilizing CuAAC to screen donor fluorophores to be compatible with SPC.

In the case that the proposed molecule is not water soluble, there are several options to introduce of water solubilizing groups. The simplest way is by the inclusion of a hydrophilic crosslinker. Either the azide or the alkyne can be functionalized with poly-ethylene glycol chains, with careful attention to not extend the crosslinker too much as to dismiss the proximity induced FRET mechanism.

A.6 Conclusion

Here, we have proposed a new imaging tool to get super-resolution imaging of free Zinc ions. Using the principals of FRET by combination of a spontaneous blinking fluorophore

acceptor, and a Zinc sensor as the donor we hope to achieve single ion imaging of free Zinc in cells. Using this technology, we hope to see Zinc in a new light under the microscope to unravel the mysterious role in pathological processes.

A.7 References

49. Hell, S. W. Far-field optical nanoscopy. *Science*, **2007**, 316, 1153–1158.
50. Huang, B., Babcock, H. & Zhuang, X. Breaking the diffraction barrier: super-resolution imaging of cells. *Cell*, **2010**, 143, 1047–1058.
51. Betzig, E. et al. Imaging intracellular fluorescent proteins at nanometer resolution. *Science*, **2006**, 313, 1642–1645.
52. Hess, S. T., Girirajan, T. P. K. & Mason, M. D. Ultra-high resolution imaging by fluorescence photoactivation localization microscopy. *Biophys. J.*, **2006**, 91, 4258–4272.
53. Rust, M. J., Bates, M. & Zhuang, X. Sub-diffraction-limit imaging by stochastic optical reconstruction microscopy (STORM). *Nature Methods*, **2006**, 3, 793–796.
54. Folling, J. et al. Fluorescence nanoscopy by ground-state depletion and single-molecule return. *Nature Methods*, **2008**, 5, 943–945.
55. Heilemann, M. et al. Subdiffraction-resolution fluorescence imaging with conventional fluorescent probes. *Angew. Chem. Int. Ed.*, **2008**, 47, 6172–6176.
56. Grecco, H. E.; Verveer, P. J. FRET in Cell Biology: Still Shining in the Age of Super-Resolution? *Chem. Phys. Chem.*, **2010**, 12, 484-490.
57. Vogelsang, J.; Steinhauer, C.; Forthmann, C.; Stein, I.; Person-Skergo, B.; Cordes, T.; Tinnefeld, P. Make them blink: probes for super-resolution microscopy. *Chem. Phys. Chem.*, **2010**, 11, 2475-2490.
58. Urano, Y. et al. A Spontaneously blinking fluorophore based on intramolecular spirocyclization for live cell super-resolution imaging. *Nature Chem.*, **2014**, 6, 681-689.

59. Sreenath, K., Clark, R. J., Zhu, L. Tricolor Emission of a fluorescent Heteroditopic Ligand over a Concentration Gradient of Zinc(II) ions. *J. Org. Chem.*, **2012**, *77*, 8628-8279.
60. Jradi, F. M.; Lavis, L. D., Chemistry of Photosensitive fluorophores for single-molecule localization microscopy *ACS Chem. Biol.*, **2019**, *14*, 1077-1090.

Curriculum Vitae**David Nabil Barsoum**

1320 N. Milwaukee Ave. Apt 2 Chicago, IL 60622

Phone: (561) 414-8705

Email: davidbarsoum2015@u.northwestern.edu

EDUCATION2015-Present **Northwestern University, Department of Chemistry**

Degree Awarded: PhD in Organic Chemistry

Research Adviser: Assistant Professor Julia Kalow (2017-present), Professor Karl Scheidt (2015-2017)

Thesis Title: *Remote Controlled Exchange Rates by Photoswitchable Internal Catalysis of Boronic Ester-Diol Exchange*

2014

Florida State University, Department of Chemistry and Biochemistry

Degree Awarded: B.S. in Biochemistry with Honors in the Major and Minor in Mathematics

Research Adviser: Associate Professor Lei Zhu (2012-2015)

Thesis Title: *Rhodamine B Thiohydrazide Tautomerization Chemistry & a New Class of Rhodamine Spirolactam Indicators***PUBLICATIONS**

1. **Barsoum, D. N.**; Kalow, J. A. Remote Controlled Exchange Rates by Photoswitchable Internal Catalysis of Dynamic Covalent Bonds (submitted).
2. Fitzpatrick, K. P.; Schwamb, C. B.; Check, C. T.; Jang, K.-P.; **Barsoum, D. N.**; Scheidt, K. A. Development of Ferrocene-Based Planar Chiral Imidazopyridinium Salts for Catalysis *Organometallics* **2020**, 39, 14, 2705– 2712.
3. Wang, M. H.; **Barsoum, D. N.**; Scwamb, C. B.; Cohen, D. T.; Goess, B. C.; Riedrich, M.; Chan, A.; Maki, B. E.; Mishra, R.K.; Scheidt, K. A. Catalytic, Enantioselective β -Protonation through a Cooperative Activation Strategy. *J. Org. Chem.*, **2017**, 82, 4689-4702.
4. **Barsoum, D. N.**; Kyeremeh-Mensah, L.; Clark, R. J.; Masson, E.; Zhu, L. Zn²⁺ Complexes of N,N-di-(2- picolyl)hydrazones. *Eur. J. Inorg. Chem.* **2016**, 35, 5477-5484.
5. **Barsoum, D. N.**; Okashah, N.; Zhang, X.; Zhu, L. Mechanism of Copper(I)-Catalyzed 5-iodo-1,2,3- triazole from azide and terminal alkyne. *J. Org. Chem.* **2015**, 80, 9542-9551.
6. **Barsoum, D. N.**; Brassard, C. J.; Deeb, J. H. A.; Okashah, N.; Sreenath, K.; Simmons, J. T.; Zhu, L. Synthesis of 5-iodo-1,2,3-triazole from organic azide and terminal alkyne – ligand acceleration effect, substrate scope, and mechanistic insight (Feature Article). *Synthesis* **2013**, 45, 2372-2386.

RESEARCH EXPERIENCE

Graduate Research Assistant, Northwestern University (July 2017 to present, Kalow Laboratory) Project Summaries:

- **Remote Controlled Exchange Rates by Photoswitchable Internal Catalysis of Boronic Ester-Diol Exchange (2018-Present)**
Proposed and designed a photoswitchable internal catalyst capable of remotely tuning the rates of exchange between boronic ester/diol over 4 orders of magnitude. Currently exploring the ability to control the rate of exchange of boronic esters with diols through reversible photoinduced-isomerization of acylhydrazones and relating small molecule kinetics to macroscopic properties in polymer networks.

Graduate Research Assistant, Northwestern University (November 2015 to July 2017, Scheidt Laboratory) Project Summaries:

- **Selenourea Complexes for determining the Relative Nucleophilicity of Planar Chiral NHCs (2016-2017)**
Successfully synthesized several selenourea complexes of planar chiral NHCs and determined their relative nucleophilicities via ^{77}Se NMR and X-ray crystallography.
- **Mechanistic Insight to Enantioselective β -Protonation (2016-2017)**
Constructed a Hammett Plot using a ^1H -NMR assay based real-time monitoring method to elucidate the rate determining step of a reaction which provided key insights into the role of the cooperative catalysis system.
- **Developing a FRET Based High Throughput Experiment Platform (2016)**
Proposed and designed project for a high throughput screening platform utilizing FRET as a rapid quantitative method to determine product yields.

Undergraduate Research Assistant, Florida State University (January 2012 to June 2015, Zhu Laboratory) Project Summaries:

- **Synthesis of 5-iodo-1,2,3-triazoles from Organic Azide and Terminal Alkyne (2012-2013)**
Successfully led five group members in developing a synthetic method for 5-iodo-1,2,3-triazoles, which was especially effective in activating previously unreactive aromatic azides and provided mechanistic insight.
- **Rhodamine B Thiohydrazide Tautomerization Chemistry (2013-2014)**
Successfully proposed, wrote, and defended an Honors Thesis project on the synthesis and structural investigation of rhodamine B thiohydrazide derivatives and proposed a new class of rhodamine B hydrazides for future investigation.
- **Characterizing the Zinc(II) Complexes of N,N-di-(2-picolyl)hydrazone (DPH) Ligands (2014)**
Proposed and designed project for a new type of coordinating group that has two potential binding modes. Successfully characterized the two binding modes with several ligands in solution and the solid state.

- **Structural and Photophysical Investigation of 1,4,5-aromatically-substituted-1,2,3-triazoles** (2014) Directed project and mentored an undergraduate student on the synthesis of tri-aromatically substituted triazoles to investigate the potential fluorescent properties.
- **Spontaneous Blinking of Rhodamine Spiroindoline Dyes for Super-Resolution Imaging** (2014) Successfully synthesized rhodamine B spiroindoline ligands to elucidate the structural role in ground state switching efficiency for STORM imaging, which was a major contribution to the work led by graduate student Kirsten Daykin.
- **Mechanism of Cu(I) Catalyzed 5-iodo-1,2,3-triazoles from Azide and Alkyne** (2015) Concisely distinguished the mechanistic pathway of iodotriazole formation from prototriazoles using a ¹H-NMR assay based real-time monitoring method and isolation of a carbene-stabilized Cu-triazolide intermediate.

AWARDS, HONORS, & SCHOLARSHIPS

- National Science Foundation Graduate Research Fellowship (NSFGRFP, 2015)
- ACS Organic Division Undergraduate Award (2013)
 - *Awarded for top undergraduate organic chemistry research assistant at Florida State University*
- Honors in the Major (2013)
- Bess H. Ward Honors Thesis Scholarship (2013)
- Delos F. and Frances L. DeTar Chemistry Research Fellowship (2013)
- 3rd Place Undergraduate Poster at FAME (2013)
- Russell H. and Dorothy P. Johnsen Chemistry Research Fellowship (2012)
- 1st Place Undergraduate Poster at FIMS (2012)

SKILLS AND TECHNIQUES

- Organic synthesis
- ¹H-NMR based real-time kinetics
- Photoredox/Photochemistry
- Methodology Development
- UV/Vis & Fluorescence Spectroscopy

PRESENTATIONS

Talks:

- 91st Florida (ACS) Annual Meeting and Exposition (FAME) in Tampa, FL (2015)
- 66th Southeastern Regional Meeting of the ACS (SERMACS) in Nashville, TN (2014)
- Honors in the Major Thesis Defense (2013)

Posters:

- Artificial Molecular Switches and Motors Gordon Research Conference (GRC) (2018)
- 246th ACS National Meeting & Exposition in Indianapolis, IN (2013)
- FSU Fall Undergraduate Research Symposium in Tallahassee, FL (2013)
- 89th Florida (ACS) Annual Meeting and Exposition (FAME) in Tampa, FL (2013)
 - *Awarded 3rd place for undergraduate poster presentation*

- Florida Inorganic and Materials Symposium (FIMS) in Gainesville, FL (2012)
 - *Awarded 1st place for undergraduate poster presentation*